AD-A105 707 SYRACUSE UNIV NY DEPT OF ELECTRICAL AND COMPUTER EN--ETC F/G 11/9
POLYMERIC MICROELECTRONICS.(U)
JUN 81 S T KOWEL, E BALIZER, T T SU, I H LOH DAAK70-80-C-0053
UNCLASSIFIED TR-81-6 NL

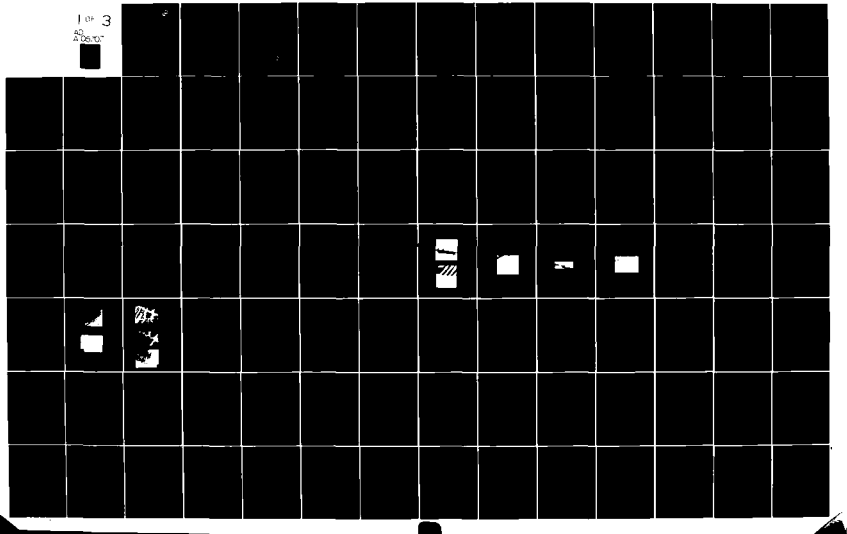

Report #DAAK70-80-C-0053-1 / TR81-6

POLYMERIC MICROELECTRONICS

June 1981

Prepared for the

US Army Night Vision and Electro-Optics Laboratory

Fort Belvoir, VA 22060

by

Stephen T. Kowel
Edward Balizer
T. T. Su
I. H. Loh
Dennis Cleverly
George C. Martin
Philipp G. Kornreich

DEPARTMENT OF ELECTRICAL AND COMPUTER ENGINEERING

SYRACUSE UNIVERSITY

Syracuse, NY 13210

(14) TR-81-6

Unclassified

SECURITY CLASSIFICATION OF THIS PAGE (When Data Entered)

REPORT DOCUMENTATION PAGE

READ INSTRUCTIONS BEFORE COMPLETING FORM

1. REPORT NUMBER: DAAK70-80-C-0053-1

2. GOVT ACCESSION NO.: AD-A102 707

3. RECIPIENT'S CATALOG NUMBER:

4. TITLE (and Subtitle): (6) Polymeric Microelectronics,

5. TYPE OF REPORT & PERIOD COVERED: Annual Technical 5/80 - 5/81

6. PERFORMING ORG. REPORT NUMBER: TR81-6

7. AUTHOR(s): (10) Stephen T. Kowel, Edward Balizer, T.T. Su, I.H. Loh, Dennis Cleverly, ~~George Martin, and Philipp G.~~ Kornreich.

8. CONTRACT OR GRANT NUMBER(s): (15) DAAK70-80-C-0053

9. PERFORMING ORGANIZATION NAME AND ADDRESS: Department of Electrical and Computer Engineering, 111 Link Hall, Syracuse University, Syracuse, NY 13210

10. PROGRAM ELEMENT, PROJECT, TASK AREA & WORK UNIT NUMBERS: 62709A, 11162709DH95, 00 001C5 (16) (17) 00

11. CONTROLLING OFFICE NAME AND ADDRESS: U.S. Army Night Vision and Electro-Optics Laboratory, Fort Belvoir, VA 22060 (12) 235

12. REPORT DATE: 6/1/81 (11) 1 Jun 82

13. NUMBER OF PAGES: 226

14. MONITORING AGENCY NAME & ADDRESS(if different from Controlling Office): (9) Annual technical rept. May 80-May 81,

15. SECURITY CLASS. (of this report): Unclassified

15a. DECLASSIFICATION/DOWNGRADING SCHEDULE:

16. DISTRIBUTION STATEMENT (of this Report)

Distribution list;

distribution unlimited

17. DISTRIBUTION STATEMENT (of the abstract entered in Block 20, if different from Report)

18. SUPPLEMENTARY NOTES

The support for this work was provided by the Advanced Concept Team, Office of the Director of Army Research, Department of the Army, DAMA-ZE, Washington, D.C. 20310

19. KEY WORDS (Continue on reverse side if necessary and identify by block number)

Polymers, microstructures, adaptive optics, liquid crystals, adaptive lenses, adaptive mirrors.

20. ABSTRACT (Continue on reverse side if necessary and identify by block number)

Our basic goal has been to evaluate the suitability of polymer systems for use in adaptive optics. Structures such as the electrostatically controlled mirrors and lenses described in this report require the mating of materials relatively new to electronics applications with microfabrication technology. Microprocessor technology will be essential in electronically "calibrating" structures with little inherent optical quality. → next page

DD FORM 1 JAN 73 1473 EDITION OF 1 NOV 65 IS OBSOLETE

Unclassified 406 739

SECURITY CLASSIFICATION OF THIS PAGE (When Data Entered)

The resultant devices should be small, inexpensive, and should require low power and voltages since no mechanical motion is employed. In the case of deformable mirrors, analysis indicates that elastomer microstructures should be capable of larger deformations than conventional adaptive optical components. Microfabrication creates structures with large area-to-volume ratios. Thus electrostatic forces can overcome inertial forces.

We have verified that such materials can be spread in thin sheets and formed into islands smaller than 20μm on a side. The techniques developed depend on using elastomers which can serve as "resist". Exposed to ultraviolet light through a mask, they are chemically altered and the unwanted portions can then be washed away.

We have also demonstrated that conductive and reflective metal electrodes can be deposited using low temperature conditions. The thin films created should not stiffen the polymer appreciably. Indium is the best material for use in these structures.

In addition to mirror structures, we have studied the concept of a liquid crystal matrix lens. Appropriate voltages will produce a two-dimensional variation of index of refraction, creating a spherical phase front for a plane wave input. Focal lenghts of several meters appear possible. A system of four tandem nematic lenses has been shown to provide focussing action for a beam of light with arbitrary transverse polarization.

High resolution display applications cannot tolerate fringing effects. For the lens application, however, the fringing effect in a high density array should create a graduation in index of refraction, greatly improving phase performance. With a dense set of small electrodes, performance approaching diffraction-limited is expected.

TABLE OF CONTENTS

LIST OF FIGURES

LIST OF FIGURE (Cont'd)

LIST OF FIGURES (Cont'd)

LIST OF FIGURES (Cont'd)

LIST OF TABLES

Chapter 1: Introduction

1.0 General

Much interest in recent years has centered on the field of adaptive optics. (1) Aberrations in optical systems such as telescopes can be minimized in real time by the insertion of a phase correcting mirror on a piezoelectric substrate. The mirror surface is deformed by a set of actuators. Typically a small number of actuators (less than twenty) is used, each requiring adjustable voltages on the order of several thousand volts. Such high voltages are required to move the surface by 0.1μm since the ceramic piezoelectric is practically incompressible.

The research described here has as its goal the creation of adaptive optical components requiring lower voltages, lower weight, and lower cost. Also, the structures under study, if successful, would be capable of significantly greater phase control. Thus controllable lenses and beam formers could be created.

A new area of polymer technology is the use of polymeric materials in electronic devices such as transducers, switching systems, or electronically tunable lenses (2). Among the various polymeric materials, low modulus silicone polymers are used for the majority of optical devices. The large deformations of crosslinked polydimethylsiloxane (PDMS) induced by uniaxial

compression lead to applications of deformable microcomponents. A variety of optical components such as the Ruticon (2) has been developed in which image storage is obtained by optically inducing a charge distribution which deforms the elastomer. The metallized elastomer then reflects the wavefront as shown in Figure 1.0-1. These new concepts are of potential importance in the field of imaging and image display.

1.1 Objectives

One primary objective of this study was the creation of a microcomponent consisting of metal film overlaid with a deformable polymer network and a reflecting metal film as shown in Figure 1.1-1. Typical dimensions of the microcomponent are 20 μm in width and 40 μm in height. The surface of the structure should be capable of reflecting incident light and conducting electricity . By applying a voltage across such a structure, shown in Figure 1.1-1, the electrical force induces a mechanical compression of the structure due to the deformation in the soft elastomer. The structure could be used as a focusing mirror or an electronically controlled beam scanner.

It is recognized that the tensile modulus for this compression deformation is approximately a factor of three greater than that for a shear deformation. In order to take advantage of this difference of moduli, and inverted L-shaped structure shown in Fig. 1.1-2 which deforms according to a shear mode was

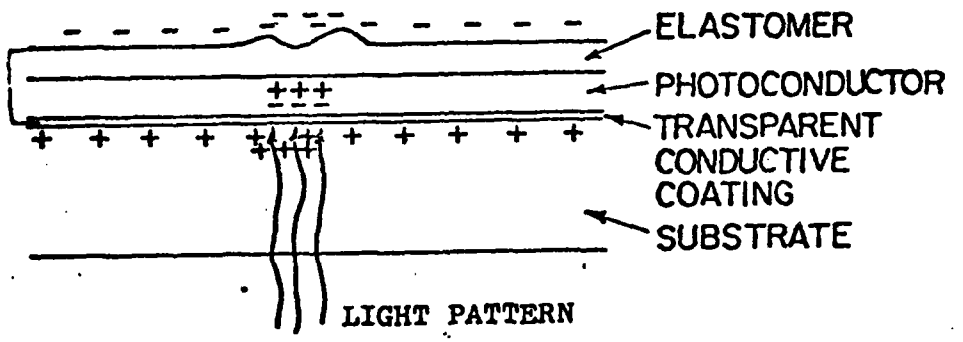

Fig. 1.0-1 Mechanism of Ruticon Image Formation

When the photoconductor is illuminated, charges move toward the photoconductor-elastomer boundary. These charges modulate the electrical field and the top surface of the elastomer deforms.

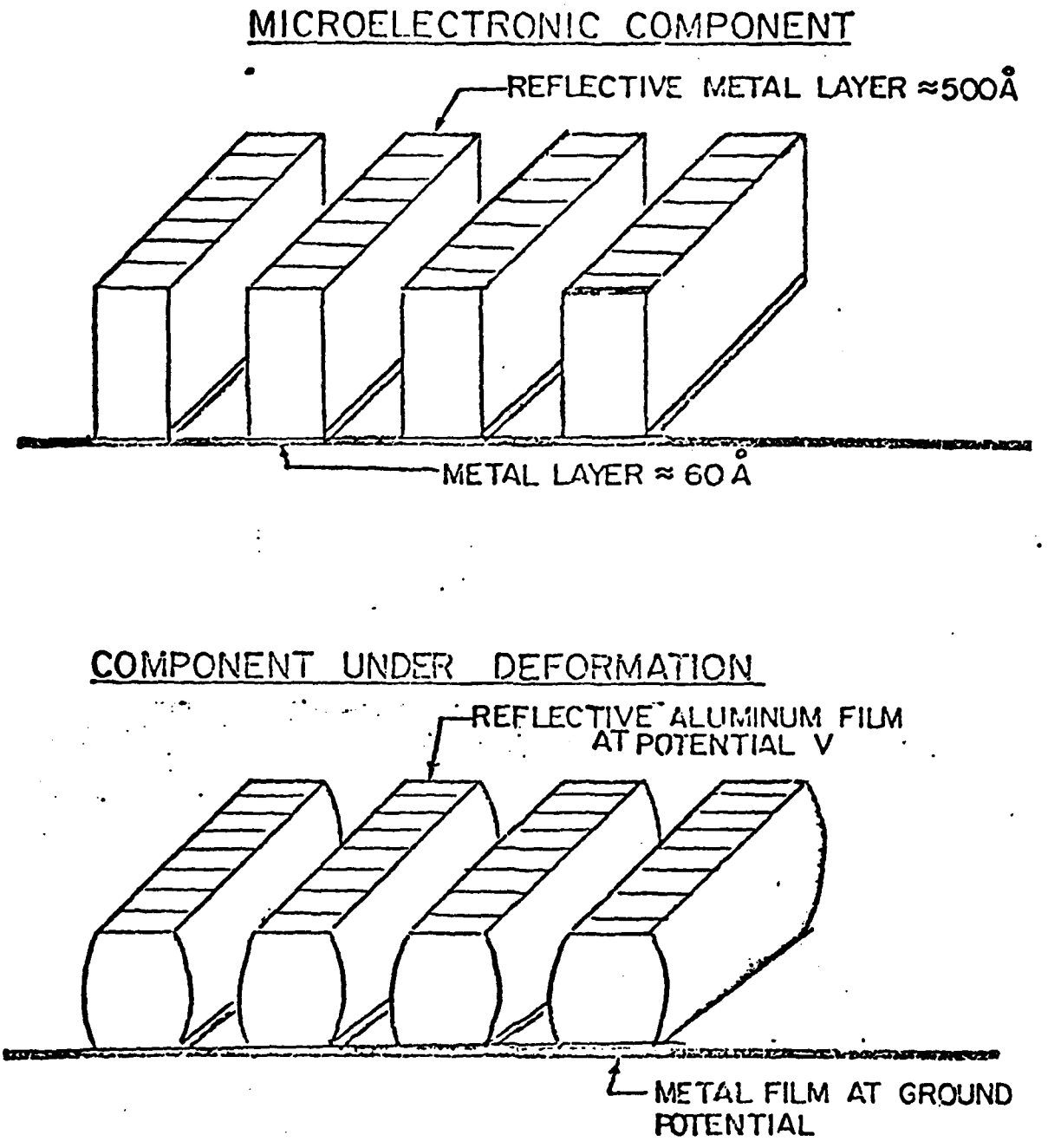

Fig. 1.1-1 Typical Polymeric Microstructures

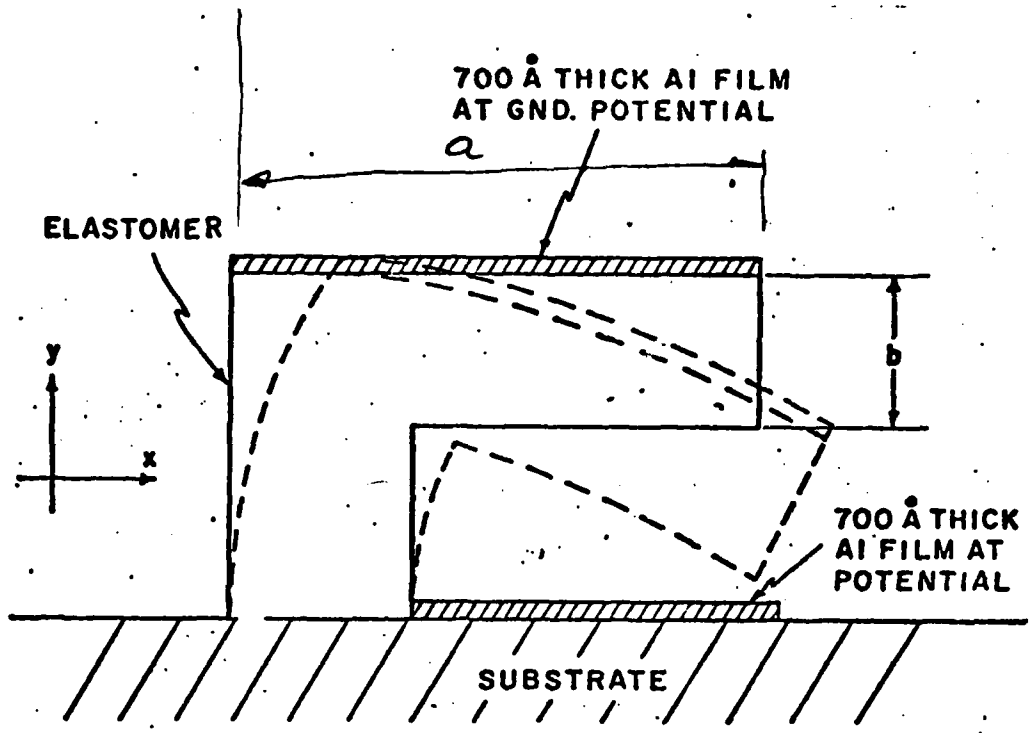

Figure 1.1-2 Side View of a Microplate Element Undergoing Deflection

proposed to maximize the deformation. The equation of motion for the shear deformation as a function of voltage is presented in detail in Appendix 1A. A future objective is to fabricate such a structure.

Another area of research is concerned with adaptive optical components based on transmission rather than reflection. A liquid crystal is capable of large index of refraction changes under electronic control. We have studied the concept of a liquid crystal lens for image formation as well as aberration control.

1.2 Photochemical lithography of silicone elastomers

(a) Materials characterization

In this study, the structure and properties of crosslinked silicone polymers and their applications as microelectronic components were explored. Equilibrium swelling techniques have been used to characterize the elastic moduli of crosslinked silicone polymer gels and the uncrosslinked fractions in the curing process. Both large samples and thin films were investigated. The consistency in uncrosslinked fractions between the two samples indicated that both crosslinking reactions followed the same mechanism and the elastic moduli obtained from large samples could be used to estimate those of the microcomponents.

(b) Photochemical lithography

A photochemical lithographic technique was devised for the fabrication of a microcomponent on a glass substrate. This technique consisted of the exposure of the polymer gels to ultraviolet radiation through an aluminum mask and the development of the elastomer pattern. The physical shape of the developed pattern was explained in terms of the uncrosslinked fraction data obtained from the equilibrium swelling experiments.

(c) Infrared characterization

Since the microstructures are thin and have one surface fixed to a plate, there is some difficulty in obtaining equilibrium swelling measurements. An alternative method of characterization of the crosslink density is by infrared spectroscopy. The absorbance spectra were identified according to the bond structure of the silicones. The bonds reactive in crosslinking were measured with respect to time of curing to determine crosslinking kinetics. In addition the absorbance in the infrared was found as a function of sample thickness. The results yielded information as to polymer - polymer interactions and the effect of UV radiation on the silicones.

1.3 Metallization of silicone elastomers

For high quality reproduction of images these devices require large reversible deformations of the elastomer and a highly reflective metallic coating. Ruticons used cross-

linked silicone elastomers for their mechanical properties and various metals for the reflecting surface. The amount of metal required for good reflectivity was sufficiently thick to alter the mechanical behavior of the elastomer and, therefore, its imaging capabilities were limited.

We developed a cryogenic metallization technique to coat the device with a very thin reflecting metallic film that may not perturb the elastic properties of the silicone substrate. The classical nucleation theory was used to interpret this phenomenon.

1.4 Theoretical Models of static deformation

Theoretical models have been formulated to analyze the static deflection of the polymer microstructure. The equilibrium equations were derived from an energy function composed of two parts. One contribution was the strain energy as found from the theory of rubber elasticity, the other that of the electrostatic energy due to a potential across a capacitor. This model yielded expressions for the static deformation in terms of the applied potential and the modulus of the gel.

1.5 Experimental measurements of the deformation

The deformation of the gel was measured by an interferometric technique using the red band from a He Ne laser. The structures had both thin film and finger electrode geometries for exciting the deformation. The thin film electrodes yielded interference patterns from which a deformation could

be measured as a function of voltage. Both gold and aluminum were used for the thin film electrodes and measurements for the deformation as a function of voltage were obtained. However, the interference pattern for the finger electrodes was not well defined; this led to an investigation of optimization of parameters in the metallization technique so that an improved surface could sustain a pattern.

1.6 The dynamic characterization of polymer films

In order to model the dynamics of the structure and estimate response times, the viscous and elastic tensor components have to be determined. Since the gel is isotropic, there are only four constants to be determined; two elastic and two viscous. A non-destructive experimental technique to determine these constants is the propagation of plate modes in a delay line apparatus. The dispersion relations for lossy plate modes were derived for an anisotropic film of which the gel is a special case. An example of the evaluation of elastic and loss constants was made for PVF_2.

1.7 Liquid crystal lens - Analysis

We have analysed the concept of an electronically controlled lens based on the concept of index of refraction modulation by an electric field. The materials required and the possible geometries of the structure have been studied. The optical performance has been evaluated assuming simple models for the

crosstalk between electrodes. For lens applications, this crosstalk (coupling) greatly improves the optical performance by extending the spatial frequency response.

1.8 Liquid crystal lens - Experimental effort

We have begun the experimental phase by procuring a commercial liquid crystal cell and modifying it for our purposes. No conclusive results have been obtained so far.

1.9 Pattern generator

We have nearly finished the construction of our pattern generator. A 5-watt Spectra Physics argon ion laser is the optical source for the system which is composed of three (x, y, θ) stepper motor-driven platforms under microcomputer control. This system is capable of 1 μm precision with the potential of a 1 μm spot size. The laser can be operated in the visible (green, blue) region, or in the near ultraviolet. The system is operational and is being calibrated and adjusted to maximize accuracy and minimize vibration. The computer has been programmed for simple patterns such as straight lines.

This system will permit selective crosslinking and pyrolysis of the elastomer materials.

1.10 Statement of Goals

The specific goals of the research were:

(1) to investigate the preparation and characterization of polymer gels for electronic applications (Sections 2.1, 2.2, and 2.4);

(2) to develop techniques for the lithography and metallization of these materials (Section 2.3);

(3) to determine the effects of an electric field on the viscoelastic behavior of the components (Sections 2.5 and 2.6);

(4) to develop a technique to find the viscoelastic constants to be used for modelling a general structure (Section 3.0);

(5) to analyze and fabricate an adaptive electro-optic lens based on liquid crystal technology (Section 4).

1.11 Publications:

1. "Low Frequency Acoustic Propagation in Anisotropic Thin Polymer Films", by E. Balizer, P. Kornreich, S. Kowel, and A. Mahapatra, 1980 Ultrasonics Symposium, p. 713.

2. "The Metallization of Silicone Polymers in the Rubbery and Glassy State", by E. Balizer, T. T. Su, G. C. Martin, I. H. Loh, S. T. Kowel, P. Kornreich, (accepted, Journal of Applied Physics).

1.12 Presentations:

1. "Low Frequency Acoustic Propagation in Anisotropic Thin Polymer Films", by E. Balizer, P. Kornreich, S. Kowel, and A. Mahapatra, 1980 Ultrasonics Symposium, Boston, Mass.

2. "The Metallization and Lithography of Silicone Polymers", by T. T. Su, G. C. Martin, E. Balizer, I. H. Loh, S. Kowel, P. Kornreich, 1981 A.P.S. Meeting, Phoenix, Arizona.

3. "The Photolithography of Silicone Microstructures", by T. T. Su, G. C. Martin, and S. Kowel, 1980 ACS Meeting, Las Vegas, Nevada.

4. "The Metallization and Lithography of Silicone Polymers", S. Kowel, Dec. 1980, Xerox Webster Research Center.

References

1. J. W. Hardy, "Adaptive Optics - Problems and Prospects", SPIE International Technical Symposium, San Diego, CA, August 1981, Proceedings Volume 293.

2. N. K. Sheridon, IEEE Trans. on Electron Devices, Ed-19, 1003 (1972).

Chapter 2 Elastomer Structures

2.1 Materials

The materials selected for this study were low modulus silicone gels. These materials were chosen because of their low modulus and their dimensional and thermal stability. Organic elastomers such as poly(isoprene) do not have the required thermal stability and very low modulus necessary for these applications.

The silicone is to be used as a gel, that is, the individual molecules are chemically bonded to each other until the gel point is attained,i.e., a single molecule is formed. The mechanisms and techniques of crosslinking and characterization of the networks are presented in this section.

A silicone polymer is composed of the repeating unit:

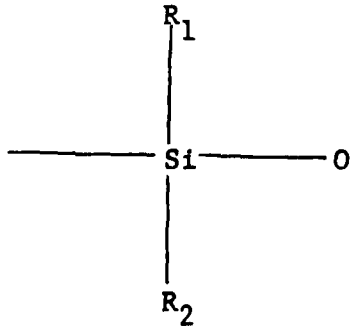

R_1 and R_2 are commonly chosen to be one of the following groups, $CH_2 = CH$, CH_3, $CF_3CH_2CH_2$, $CNCH_2CH_2$. For $R_1 = R_2 = CH_3$, polydimethylsiloxane results. The crosslinking begins by initiating a radical (unbonded electron) on the methyl group. This occurs when, upon heating, a peroxide initiator (mixed into the polymer) breaks into a diradical by the reaction:

$$R - R + Q \xrightarrow{140^{\circ}C} \dot{R} + \dot{R}$$

The radical peroxide transfers the electron to a methyl site:

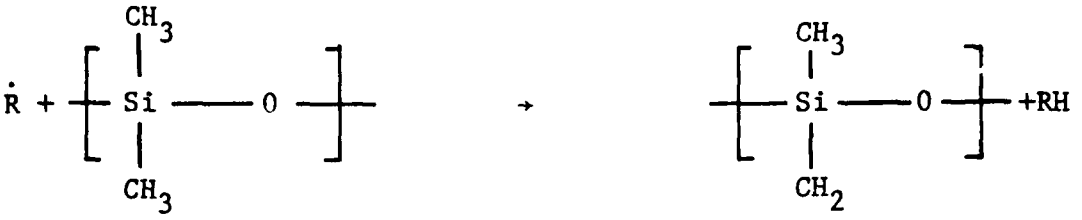

The unpaired electron of the side group carbon atom is now reactive and capable of bonding to a similar species as follows:

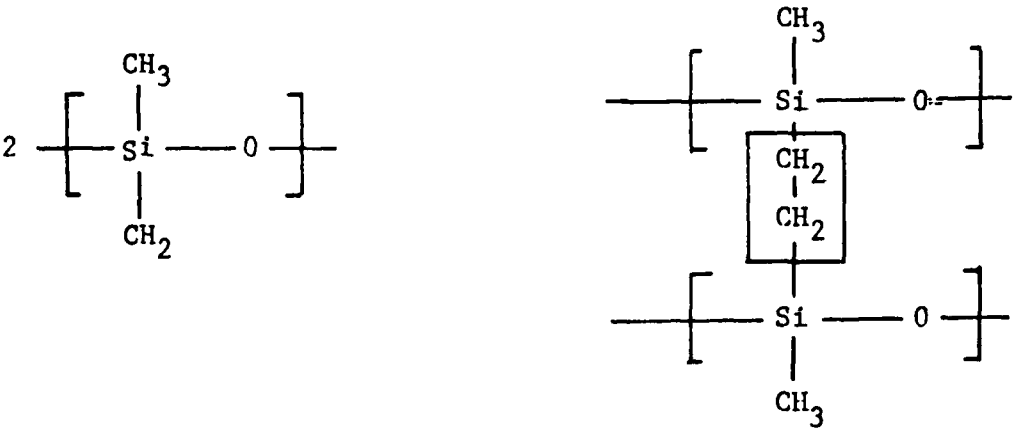

The resulting crosslink is bracketed above.

The crosslinking occurs randomly in the network; however, fluctuations may occur due to aggregation of the peroxide so that a nonuniform crosslinking density occurs. This problem may be circumvented by periodically substituting a diene CH_2 = CH group for a methyl group in the polymer chain. Sine the diene group is more susceptibel to radical formation, uniformly distributed diene groups result in a network with a uniform crosslink density. For the vinyl crosslinking an initiator

which is unreactive with saturated bonds and reactive only with the double-bonded vinyl group, such as dicumyl peroxide, is used.

2.2 Characterization of the Network or Modulus Determination

The density of crosslinks or, equivalently, the number of monomer units per network chain may be found by equilibrium swelling and by stress-strain measurements. For small strains, the tensile modulus, E, of the network is

$$E = 3RT\nu_e \qquad (2.2\text{-}1)$$

where R is the gas constant, T is the absolute temperature, and ν_e is the number of chains per unit volume. The density of crosslinks may be determined using this linear relation. Equation 2,2-1 for the modulus was derived from a kinetic theory which assumes no interaction between chains. It is known that the retractive stress possesses an additional term which has been physically assigned to entanglements and transients of polymer chains.

This entanglement term has been shown to go to zero when the network is swollen. We, therefore, outline the characterization of silicone by swelling. A detailed description of the experimental procedure in the swelling experiment is given in Appendix 2A.

The numerics of the crosslinking density are given in this section. We wish to calculate the number of chains in a network. Consider a swollen silicone gel in equilibrium with a solvent (hexane). The volume fraction of the polymer, V_2, is

$$V_2 = \frac{1}{\rho_r} / [(w/\rho_h) + (1/\rho_r) \qquad (2.2\text{-}2)$$

where ρ_r is the density of the polymer, ρ_h is the density of the solvent (hexane), and w is the grams of hexane absorbed per gram of polymer. The number of modes of effective network chains per cubic centimeter, ν_e, for tetrafunctional sites is given by the relation [1]

$$\nu_e = \frac{[1_n(1-V_2) + V_2 + X_1 V_2^2]}{V_1 (V_2^{1/3} - V_{2/2})} \qquad (2.2\text{-}3)$$

where X_1 is the solvent/polymer interaction parameter (0.48 for hexane)[2] and V_1 is the molar volume of haxane (130.6 cc/mole). The value of ν_e can be compared to the modulus since, from Eq. 2.2-1,

$$\nu_e = \frac{E}{3RT}$$

This determination of the modulus depends only upon the number of true network chains and is not affected by entanglements.

2.3 Fabrication of Structures

The preparation and the lithography of elastomers based on polydimethylsiloxane were investigated. The silicone materials, crosslinked either by thermal or ultraviolet radiation, were characterized by equilibrium swelling measurements.

A process was devised for the fabrication of an elastomer microstructure on a glass substrate through the use of semiconductor photolithographic techniques. This technique consisted of the exposure of the polymer to ultraviolet radiation through an opaque mask, the development of an elastomer pattern, and the metallization of the polymer surface.

A microcomponent was constructed consisting of a metal film overlaid with a deformable polymer network and a reflecting metal film as shown in Figure 1.1-1. Typical dimensions of the microcomponent are 20 μm in width and 40 μm in height. The surface of the structure should be capable of reflecting incident light and conducting electricity.

To this end, a novel cryogenic metallization technique was introduced to coat the surface of the device with a thin reflective metal layer. The conductance of the metal film was used to characterize the metallized surface.

2.3.1 Materials for Microstructures

The three materials selected for this study were two experimental materials from Dow Corning Corporation, Midland, Michigan, designated by the supplier as System A and System B, and the

third a Dow Corning Dielectric Gel. System A and System B are ultraviolet curable while the Dielectric Gel is thermally curable. All three systems are essentially polydimethylsiloxane (PDMS) with different functional groups for crosslinking. System A consists of a mercapto-functional siloxane (X_2 - 7077) and a vinyl-functional fluid (X_2 - 7078) with the crosslinking reaction between these two sites. System B is a vinyl-functional siloxane (X_2 - 7079) and a silane-functional polymer (X_2 - 7080). The Dielectric Gel (Q_3 - 6537) is a two-part system consisting of a vinyl fluid and a silane fluid. The mixing specifications for the components are presented in Appendix 2B.

2.3.2 Characterization by Swelling of Bulk and Microstructures

(a) Large Samples (bulk swelling)

The ultraviolet curable samples (Systems A and B) were prepared according to the supplier's instructions (3) and exposed to a 200 watt Hg arc light. The exposure energy of the ultraviolet light was measured with a Laser Precision Corp. KT-4000 radiation detector. For the Dielectric Gel, the samples were prepared in aluminum cups and cured in an oven at 413 K. After preparation, the samples were swollen to equilibrium for two days, removed from hexane, and weighed. Vaporization of hexane during the weighing operation was minimized by saturating the balance atmosphere with hexane vapor before weighing. The samples were then dried in a vacuum oven for 24 hours at ambient temperature and reweighed in order to determine the soluble fraction of fluid.

(b) Thin Films (microswelling)

The ultraviolet curable Systems A and B were spin-coated on a glass substrate and exposed to ultraviolet radiation for specified periods of time. The samples were then swollen in an isooctane bath for one minute, removed, dried, and weighed. The same procedure was repeated three times for all samples. The soluble fraction or the percentage extractable was obtained by measuring the weight difference before and after swelling.

The swelling data were converted into crosslink densities and elastic moduli using the theory of rubber elasticity (Sec. 2.2). The soluble fractions, the crosslink densities, and the elastic moduli of the three systems are listed in Tables 2.3-I, II, and III. The results are plotted as a function of exposure energy (or curing time) in Figures 2.3-1, 2.3-2, 2.3-3, and 2.3-4.

(c) Soluble Fraction in Large Samples (bulk swelling)

For System A, the soluble fractions or the percentage extractables of all samples were 15% ± 2% for curing times greater than 2 minutes. This indicates that a completely crosslinked network is already formed after exposure to ultraviolet radiation for only 2 minutes. For System B and the Dielectric Gel, the crosslink reaction was not complete since the soluble fraction decreased with increasing curing time. Similar results were obtained by Schwartz et al. (4) on other silicone polymers. The scatter which occurred in the data for System B may be due to

Table 2.3-I

Bulk Swelling Data for System A

Curing Time(Min)	% Extractable	ν_e (10^2 k_g mole/m^3)	E(MPa)
2	15.1	1.49	1.1
3	12.2	1.42	1.1
4	10.6	1.78	1.3
6	13.8	1.71	1.3
7	11.5	1.83	1.4
8	12.8	1.59	1.9

Table 2.3-II

Bulk Swelling Data for System B

Curing Time(Min)	% Extractable	ν_e($k_g$mole/m^3)	E(Pa)
8	39.4	12.5	8.3×10^4
10	43.3	18.0	1.3×10^5
12	26.3	18.2	1.4×10^5
14	28.4	19.0	1.4×10^5
16	23.1	32.5	2.4×10^5
18	17.1	47.6	3.5×10^5
20	20.4	11.4	8.5×10^5
25	22.5	62.4	4.8×10^5
30	21.4	38.6	2.7×10^5
35	18.9	52.9	4.0×10^5
40	17.8	10.5	7.8×10^5
60	14.0	87.6	6.6×10^5

Table 2.3-III

Bulk Swelling Data for Dielectric Gel

Curing Time(min)	%Extractable	μ_e(mole/m^3)	E(10^4Pa)
10	48.5	4.0	2.9
15	43.3	6.7	5.0
20	39.2	8.1	6.1
25	36.7	6.5	4.9
30	32	11.7	8.8
35	22.9	24.8	19.0

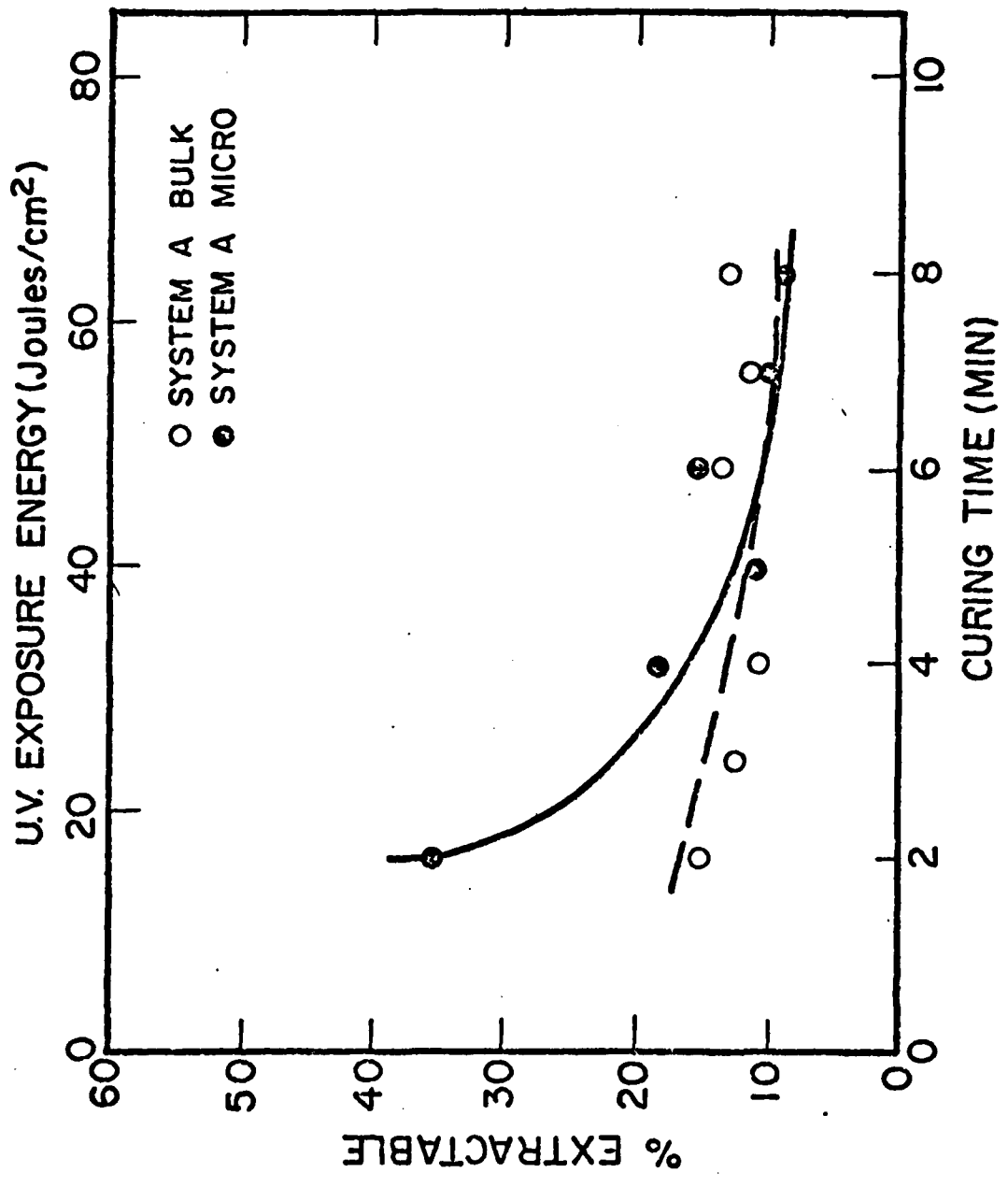

Figure 2.3-1 % Extractable versus curing time (or exposure energy) for System A

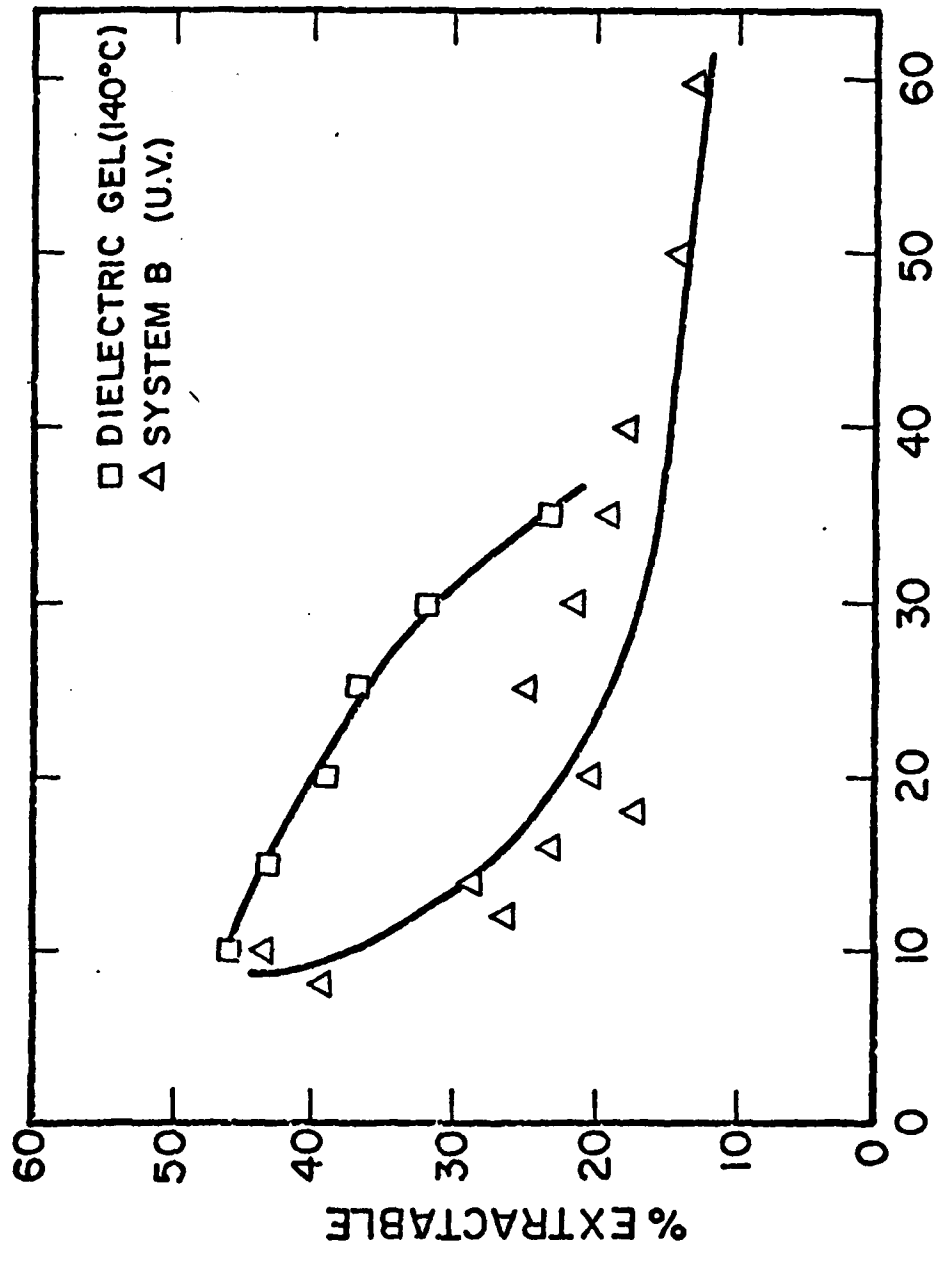

Figure 2.3-2 Extractable versus curing time (or exposure energy) for System B and Dielectric Gel

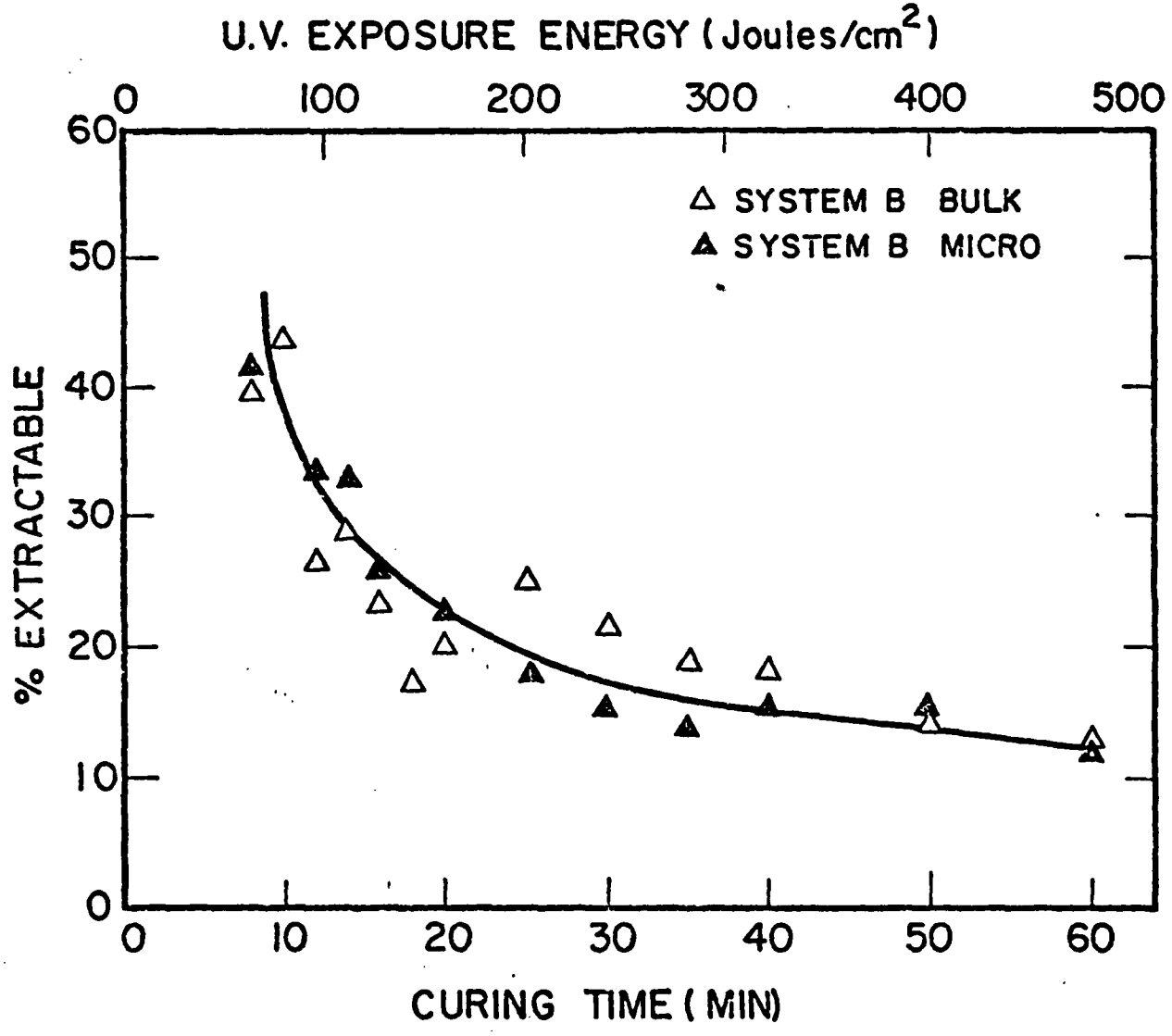

Figure 2.3-3 % Extractable versus curing time (or exposure energy) for System B ·

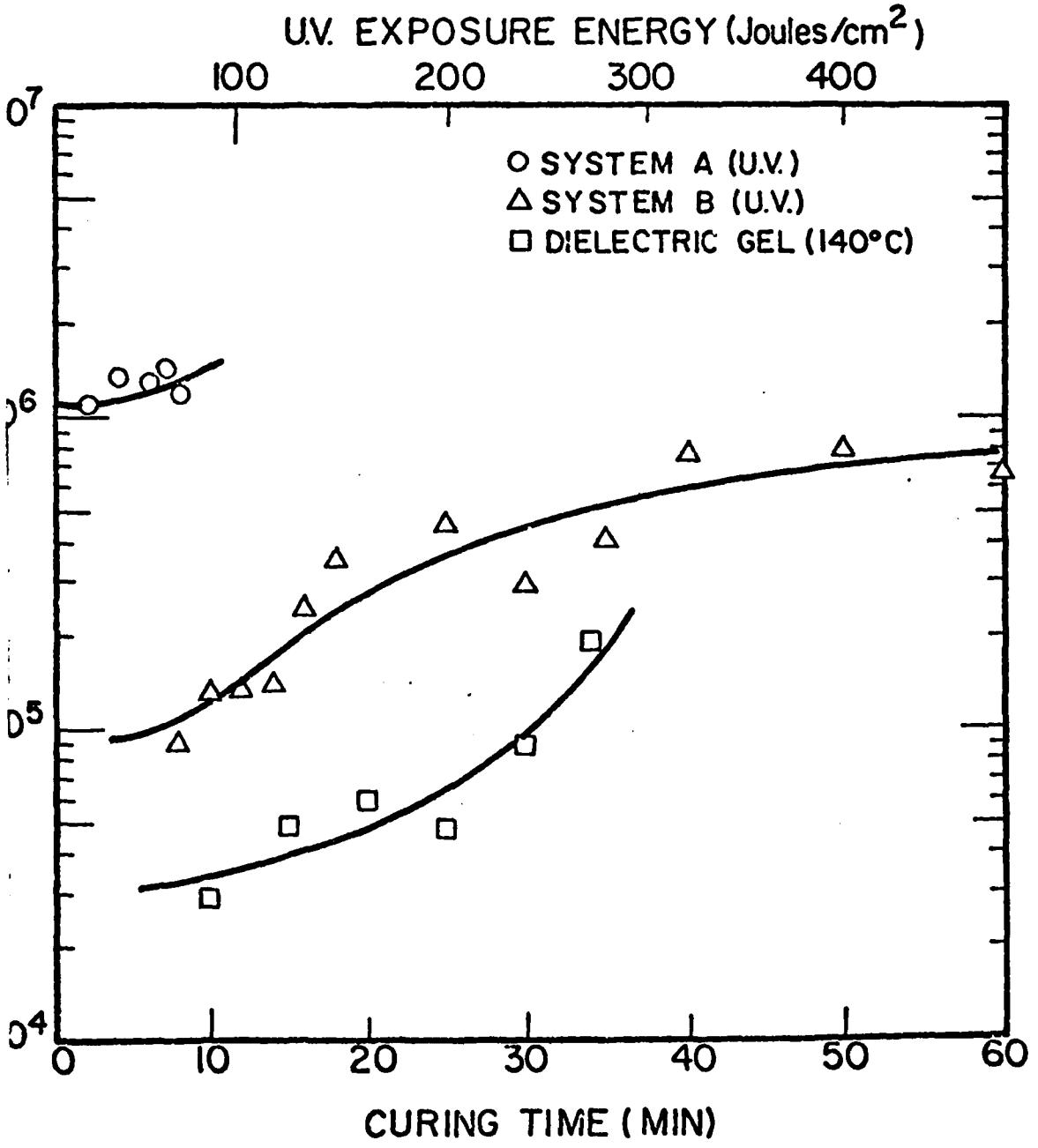

Figure 2.3-4 Variation of elastic modulus with curing time (or exposure energy)

(i) the variations in the sample geometry, which could be as high as 5%;

(ii) uncertainties in the swelling measurements;

(iii) the uncertainties in the elastic analysis, which have been attributed to the neglect of two terms. One is a factor relating the modulus to an ilolated unperturbed polymer chain. The second effect is that of chains which are ineffectively crosslinked (i.e., crosslinked at only one end) and reduce the modulus.

(d) Crosslink Densities and Elastic Moduli of Large Samples

As shown in Figure 2.3-4, the elastic modulus of System A was almost constant with curing time. This consistent with the soluble fraction data since System A formed a completely cross-linked network after an exposure of only 2 minutes whereas, for System B and the Dielectric Gel, the crosslinking reaction was not complete since the elastic modulus increased with increasing curing times which afrees with the results of Schwartz et al. (4).

(e) Thin Films (microswelling)

The objective of microswelling was to determine the uncross-linked soluble fraction in the microstructure. The results were then used to estimate the modulus of the microelectronic components from the microstructure thickness after developing. For the ultraviolet-curable Systems A and B, the soluble fractions

are listed in Tables 2.3-IV and 2.3-V, and the results are plotted in Figures 2.3-1 and 2.3-3. For both systems, the samples reached a constant weight after immersion for three minutes in isooctane indicating that this time was sufficient for completely developing the microstructures. As shown in Figure 2.3-3, the percent extractables for System B obtained from microswelling were consistent with those from bulk swelling. Hence, the elastic moduli obtained from large samples could be used to estimate the moduli of the microstructures.

2.3.3 Photolithography and Sample Preparation

As stated in Section 2.3 the specific objective of the study was the creation of a microcomponent consisting of a metal film overlaid with a polymer network and a reflecting metal film as shown in Figure 1.1-1. When an external voltage is applied across the structure in the deformation testing, the external voltage will be shorted if metal is deposited on the vertical edges. Only a vertical or an undercut structure can be metallized without depositing metal vapor on the vertical edges. For this purpose, a photochemical lithography process was devised for the fabrication of microcomponents on a glass substrate (5,6). The process included spin-coating, exposure, and developing. The physical shape of the structure was explained in terms of the uncrosslinked fraction data obtained from the equilibrium swelling experiments.

The photolithographic process first involves pretreatment of the glass substrate. Next, a photosensitive polymer film (photoresist) is applied to the substrate by spin-coating techniques.

Table 2.3-IV

Microswelling Data for System A

Curing Time	Weight of Film(g)				%Extractable
Min.	0 min.	1 min.	2 min.	3 min.	
2	.0339	.0243	.0243	.0218	35.6
4	.0335	.0280	.0274	.0274	18.2
5	.0345	.00317	.0305	.0305	11.6
6	.0361	.0331	.0331	.0306	15
7	.0350	.0313	.0316	.0313	10.6
8	.0370	.0348	.0336	.0336	9.1

Table 2.3-V

Microswelling Data for System B

Curing time(Min)	Weight of Film(g)				% Extractable
min	0 min	1 min	2 min	3 min	
8	.0281	.0176	.0165	.0165	41.3
10	.0269	.0179	.0179	.0179	33.5
12	.0266	.0196	.0178	.0178	33
16	.0271	.0211	.0201	.0201	26
20	.0289	.0231	.0223	.0223	22.8
25	.0281	.0235	.0230	.0230	18.2
30	.0282	.0239	.0239	.0239	15.3
35	.0252	.0218	.0218	.0218	13.7
40	.0269	.0236	.0236	.0227	15.5
60	.0270	.0245	.0240	.0236	12.5

The film is then selectively irradiated with an ultraviolet lamp through a mask which contains clear and opaque features outlining the desired pattern. The areas in the photoresist that are exposed to light are made either soluble or insoluble to a solvent (developer) (6). For a positive photoresist, the irradiated regions dissolve leaving a positive image of the mask on the substrate while, for a negative resist, the unexposed regions dissolve leaving a negative image of the mask on the substrate.

The photochemical lithography process used in this study is diagrammed in Table 2.1.

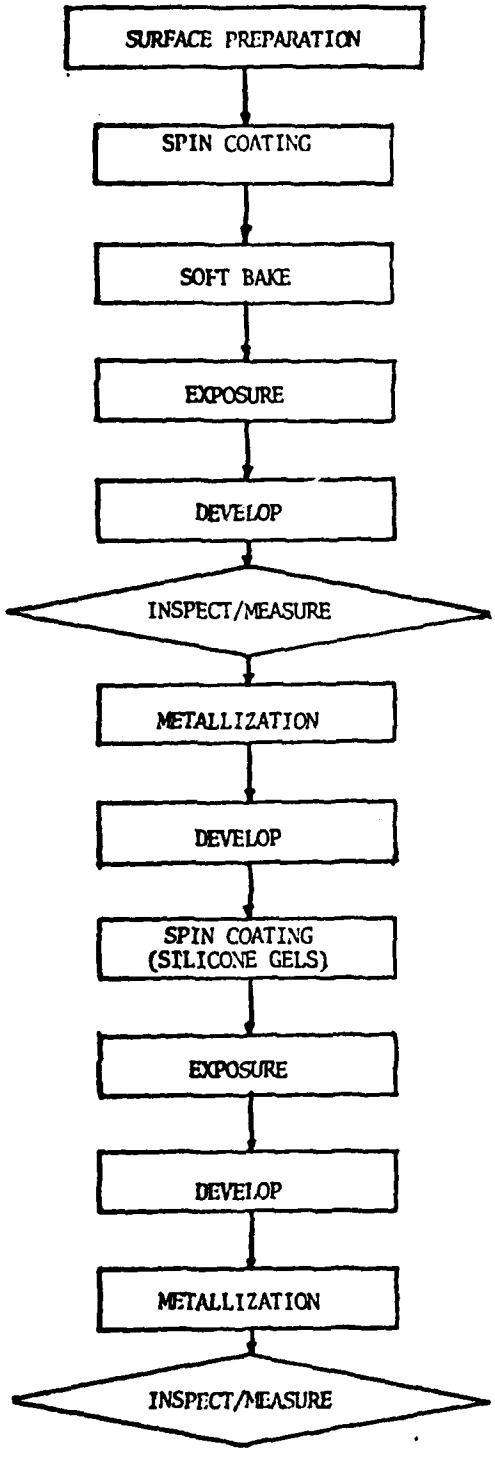

Table 2.1 Diagram of Photolithography Steps

2.3.4 Characterization

A conventional polymer resist pattern was prepared and metallized as shown in Figure 2.3-5. The resist pattern was then removed by acetone and the resulting aluminum pattern was used as a mask for the polymer gel pattern. For the deformable microstructure fabrication, a very thin transparent aluminum film (6 nm) was evaporated over the opaque pattern as shown in Figure 2.3-6. The polymer gels were then spun over the aluminum pattern as shown in Figure 2.3-7. The exposed area crosslinked while the unexposed area remained uncrosslinked. Since the crosslinked gel is insoluble, the soluble fraction was washed away by a solvent.

The relation between the microcomponent thickness and spinning speed was investigated by spin-coating the polymer gels on glass substrates at various speeds. The spin-coating results are given in Appendix 2C. The polymer films were thin cured in a 200 watt mask aligner. The thickness was obtained by measuring the cross section with an optical microscope.

The microelectronic patterns were investigated by electron and optical microscopy. To facilitate the electron microscope investigation, a thin layer of aluminum was evaporated upon the sample under high vacuum conditions to prevent charge build-up on the polymer surfaces.

Scanning electron micrographs of the electronic components prepared with System B are shown for the 20 μm wide pattern in

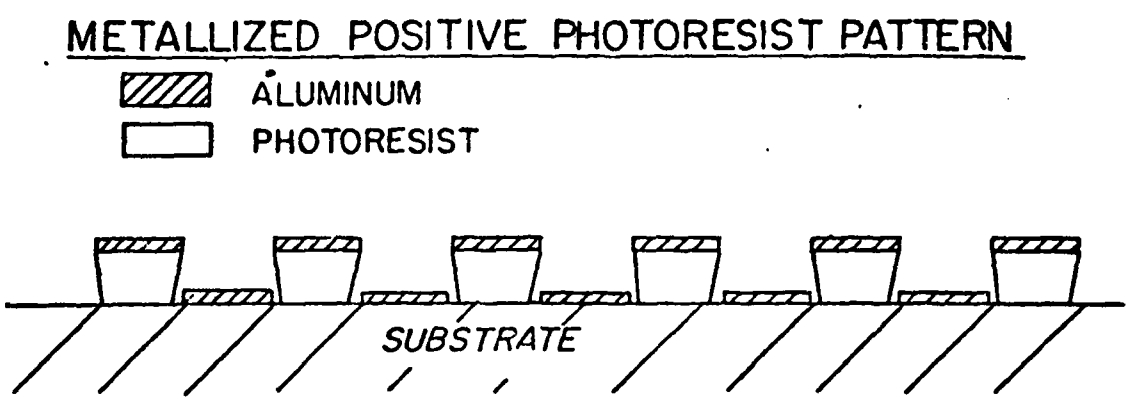

Fig. 2.3-5 Photoresist Pattern for Lift Off Technique

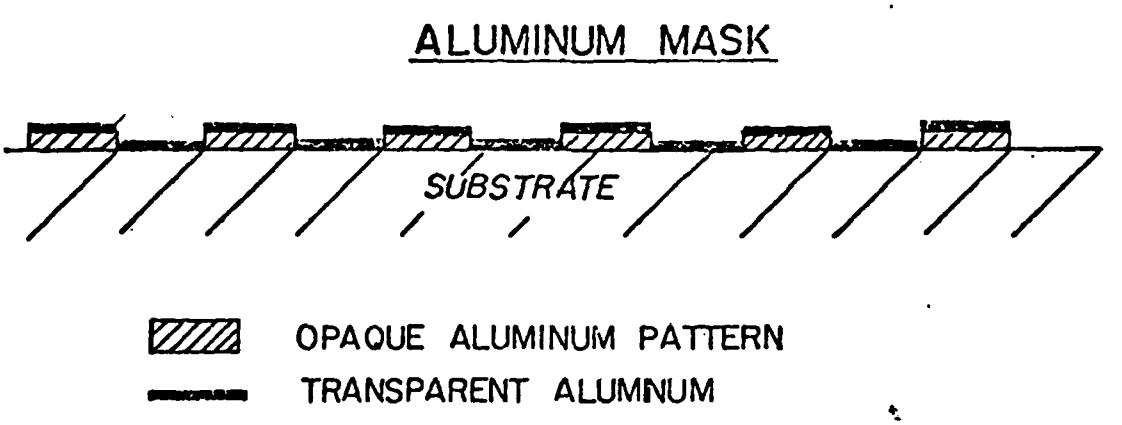

Fig. 2.3-6 Aluminum Contact and Mask Layer For Microstructure Fabrication

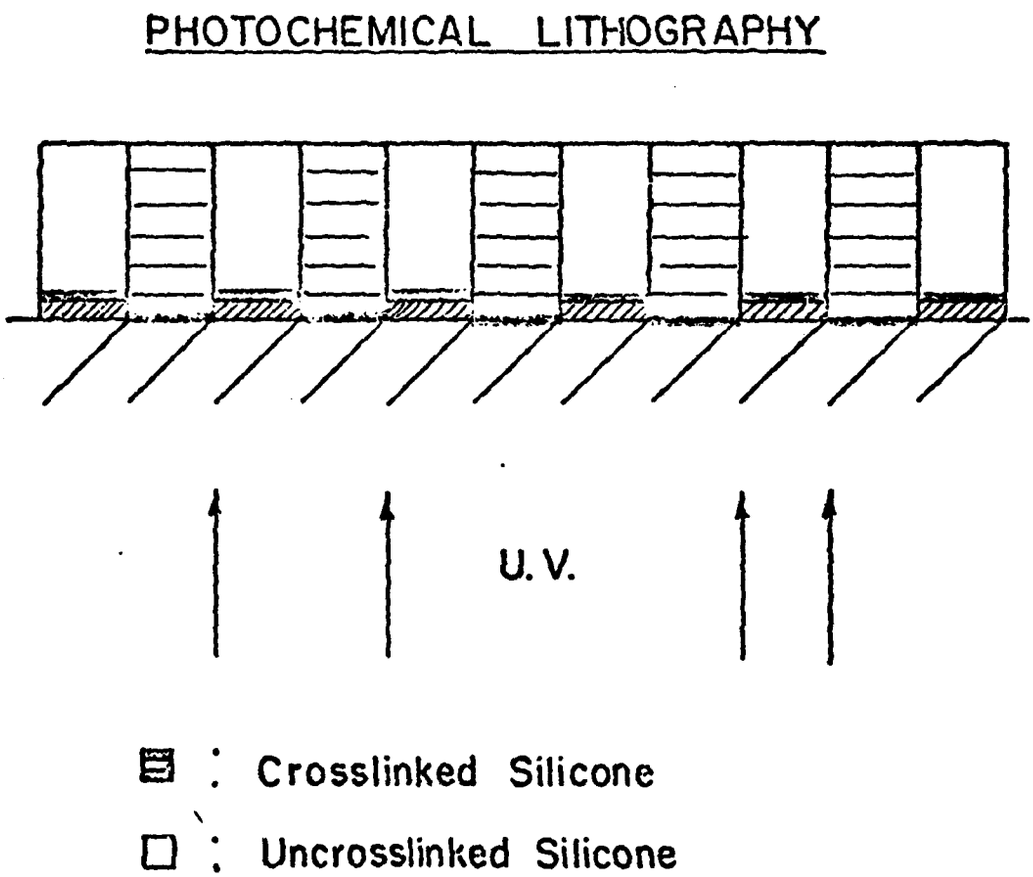

Fig. 2.3-7 Microstructure Photocythography Process

Figure 2.3-8 and for the 60 μm wide spacing in Figure 2.3-9. The polymer thickness in both samples is 13 μm. Due to the lithography process, the narrow pattern is more rectangular than the wide pattern. In developing the pattern, the solvent extracts the unexposed area and the extractable fraction of the exposed area. The exposed area contracts after drying but this contraction can occur on only three of the four sides of the pattern since the adhesion between the polymer and the substrate is strong enough to hold the sample onto the substrate. Hence, by determining the cross sectional areas of the pattern and a non-extracted pattern, the extractable fraction of the microstructure can be estimated and compared to the equilibrium swelling results. This is shown in Figure 2.3-10 in which an undeveloped and a developed pattern are shown. For this sample, an extractable fraction of 23% was obtained which is consistent with the equilibrium swelling measurements on bulk samples at similar curing times.

An optical micrograph of the electronic component prepared with System B is shown in Figure 2.3-11. The polymer was cured for 60 minutes and has a thickness of 35 μm. This pattern is much more rectangular than the 13 μm thick pattern. The structure can be used to construct a microelectronic component as shown in Figure 1.1-1.

2.3.5 Metallization of Polymer Gels in the Rubbery State and the Glassy State

It was pointed out in the previous chapter that the microstructure will be used as a focusing mirror or an electronically

Figure 2.3-8 Elastomer pattern with 20 μm spacing.

Figure 2.3-9 Elastomer pattern with 60 μm spacing.

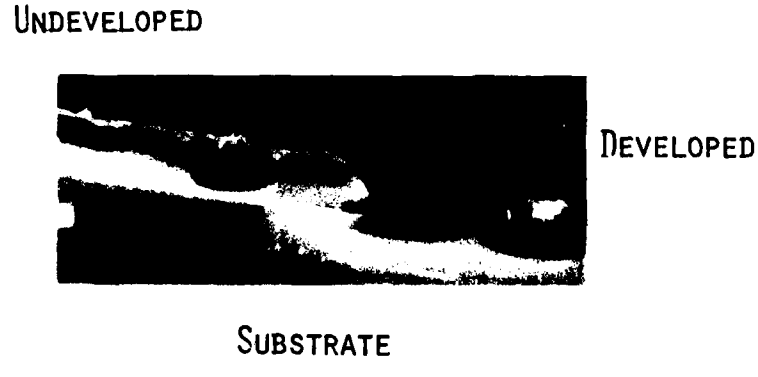

Fig. 2.3-10 SEM Picture Showing a Crossection of Undeveloped (left) and Developed Photoresist Pattern.

Figure 2.3-11 Elastomer pattern for deformation testing.

controlled beam scanner (7). The surface of the structure should be capable of reflecting incident light and conducting electricity. For these purposes, a reflective and conductive thin metal film was coated on the top surface of the components. The metal films deposited at ambient conditions with high reflectivity were thick enough to alter the mechanical behavior of the elastomer and, therefore, its imaging capabilities were very limited. A cryogenic metallization technique was developed to coat the component surfaces with a thin reflective metal layer (8). The metallization process was interpreted in terms of the physical properties of polymer gels and the classical thin film nucleation theory.

2.3.6 Experimental Procedures for Metallization

The materials were mixed according to specification and spin-cast on glass microscope slides. Samples of four different crosslink densities were prepared for each system. For System A, the samples were exposed to a 200 watt mask aligner for 0, 1, 2, and 4 minutes while, for System B, the samples were exposed for 0, 5, 10, and 15 minutes. Shorter exposure times for System A were chosen since the kinetics of crosslinking was faster than for System B. For the Dielectric Gel, one sample was cured at room temperature for 25 hours and the others were cured in an oven at 413 K for 10, 20, and 30 minutes.

For the purpose of cooling the polymer gels below their glass transition temperatures, a low temperature metallization vacuum chamber was fabricated as shown in Figure 2.3-12. The apparatus was constructed of a glass bell jar with a two-piece metal cover. The top consisted of an aluminum plate fitted with

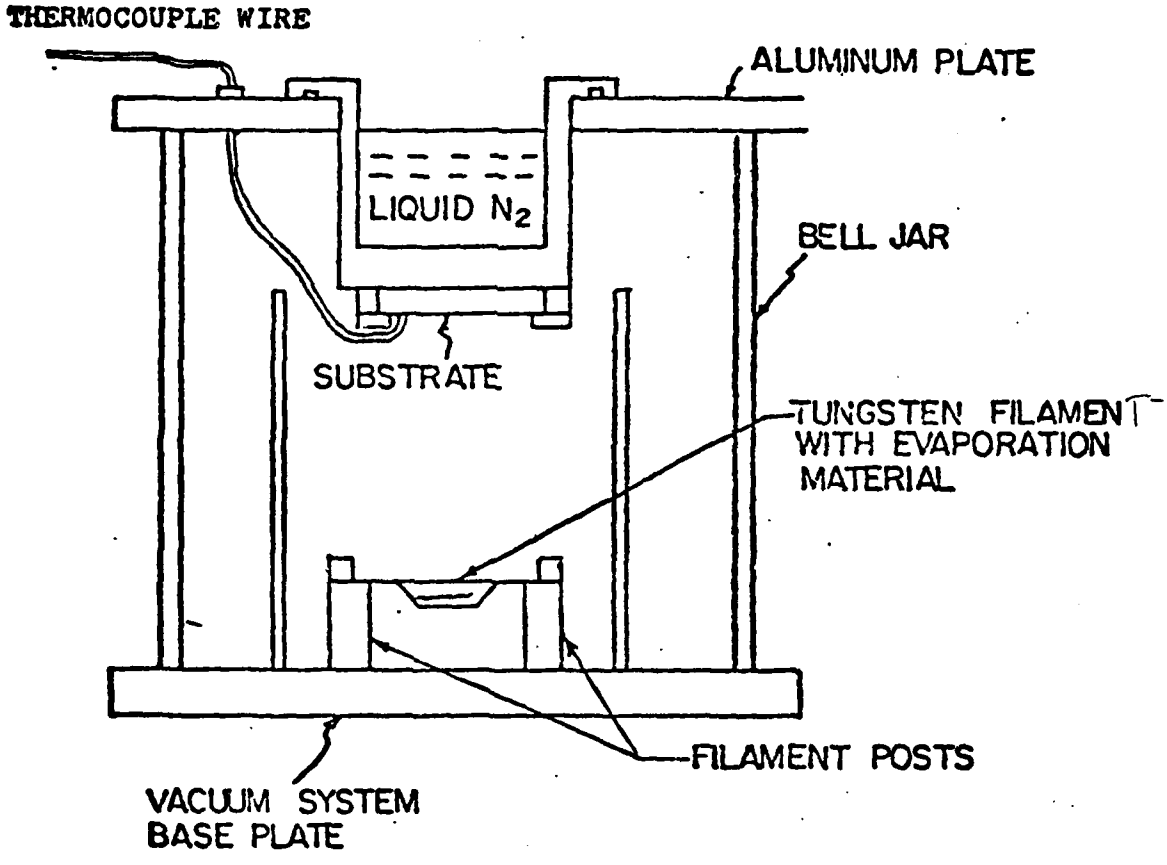

Fig. 2.3-12 Vacuum Chamber for Low Temperature Metal Evaporation

a hollow cylindrical stainless steel tube with a brass cover. When liquid nitrogen is placed in it, the tank acts as a low temperature reservior for the polymer samples clamped in thermal contact to it.

For every evaporation, four samples, each of a different crosslink density, were simultaneously metallized to maintain a uniform thickness from sample to sample. It was found for both indium and aluminum that a 0.635 cm length of 0.127 cm diameter wire evaporated at 2×10^{-6} torr was sufficient for the formation of a metal film. The films were about 50 μm in thickness. For the low temperature evaporation, the silicone was allowed to equilibrate for 30 minutes at low temperature. After ten minutes of equilibration time, the temperature of the silicone was measured to be 100 K using a thermocouple inserted into the vacuum chamber, thus assuring that the polymer was well below its glass transition temperature of approximately 150 K. (9).

The resulting metal coatings were investigated by optical microscopy and measurements of reflectance and conductance. The conductance was measured by a two-point microprobe with a separation distance of 0.6 cm. For the reflectance measurement, a He Ne laser beam was used to scan a portion of the metal film that had the highest reflectance. The selected area was scanned in a horizontal motion for three vertical heights and the largest value of the reflectance as measured by a CdS cell, was recorded. The sample averages were normalized to the reflectance measured from an aluminum metallized glass slide.

2.3.7 The Characterization of the Aluminum Metallization

In this and the following section, the results of the metal surface morphology for aluminum for indium are presented. We compare the surfaces for both low temperature and ambient temperature thermal processing.

The reflectivities and the conductances are listed in Tables 2.3-VI and 2.3-VII. All of the aluminum surfaces formed by evaporation onto the substrate at ambient temperature appeared opaque with an oxidized surface. Optical reflective microscopy showed the surface texture to consist of a fine structure of folds with no long-range correlation. This metallic texture is shown in micrograph (A) of Figure 2.3-13.

As a result of the low temperature evaporation, the gels of all three systems had a mirror-like surface. Optical microscopy for these samples, for a lower magnification than those of ambient, shown in Figure 2.3-13-B, revealed an aluminum film that contained wrinkles with a longer range of order as compared to samples produced at ambient temperature. Both the aluminum and the indium surfaces exhibited some features in common for the low temperature processing. First, large wrinkles which may be caused by flow could be seen for uncured samples (unexposed to ultraviolet radiation). Second, microscopy of the mirror-like surfaces of the low temperature gels showed that a less coarse wrinkled texture occurred for the cured materials. The size of the wrinkles decreased with increasing crosslink density of the gel as shown in Figure 2.3-14. Unlike the ambient samples, the surfaces for these samples had cracks which are probably due

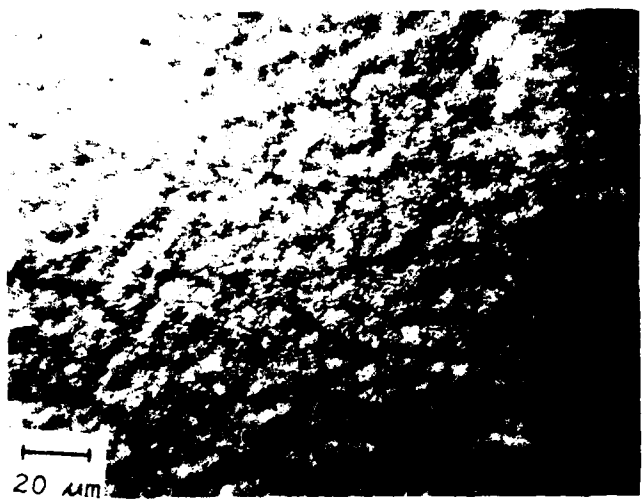

A. Aluminum evaporated onto an ambient temperature substrate. The gel is system A cured for 2 min.; the magnification is 50 x 10.

B. Aluminum evaporated onto a liquid nitrogen cooled substrate. The gel is the same system and cure as above; the magnification is 10 x 10.

Figure 2.3-13 A comparison of Al surfaces for low and ambient temperature of the substrate during evaporation.

A. System A cured for 1 minute and magnified at 10 x 10.

B. System A cured for 2 minutes and magnified at 10 x 10.

C. System A cured for 4 minutes and magnified for 10 x 10.

Figure 2.3-14 The metallized aluminum surface of the liquid nitrogen cooled gels for different cures.

Table 2.3-VI

Surface Characterization of Silicone Gels with Aluminum Metallization

Polymer System	Cure Time (min.)	Normalized Reflectance*(a) Metallization Temp. 300 K	below T_g	Conductance (10^{-2} S) (b) Metallization Temp. 300 K	below T_g
A	1	0	99	3	12
	2	61	98	3	18
	4	107	104	6	20
B	5	93	99	3	10
	10	32	101	5	10
	15	50	103	10	15
Dielectric Gel	10	—	—	0	32
	20	17	21	0	30
	30	87	75	0	37

* These reflectances were normalized to that of a metallized glass slide.

a) For those normalized reflectance values within 25% of that of glass, specular reflection occurred.

b) No conductance occurred (less than 10^{-8}S) for ambient aluminum metallization onto the dielectric gel. Although there was spread in the values, the order of magnitude of the values presented are reliable.

Table 2.3-VII

Surface Characterization of Silicone Gels with Indium Metallization

Polymer System	Cure Time (min.)	Reflectances* (a) Metallization Temp. 300 K	Reflectances* (a) Metallization Temp. below T_g	Conductance (10^{-2} S) (b) Metallization Temp. 300 K	Conductance (10^{-2} S) (b) Metallization Temp. below T_g
A	1	—	—	0	26
	2	112	86	0	38
	4	99	95	0	43
B	5	33	87	0	12
	10	70	100	0	15
	15	97	104	0	20
Dielectric Gel	10	94	90	0	32
	20	94	76	0	30
	30	91	24	0	37

* These reflectances were normalized to that of a metallized glass slide.

a) For those normalized reflectance values within 25% of that of glass, specular reflection occurred.

b) No conductance occurred (less than 10^{-8}S) for ambient indium metallization on any of the polymer substrates. Akthough there was spread in the values the order of magnitude values presented are reliable.

to the difference in expansivity between the polymer and the aluminum as the sample is taken from liquid nitrogen to room temperature.

The reflectances listed in Tables 2.3-VI and 2.3-VII show some variation. The higher values were obtained when the reflected laser beam could be focused onto the detector. The lower reflectance values occurred when the reflected beam was diffused, thus indicating the smoothness of the texture of the metallic surface. A comparison of the reflectance for System A illustrates that a higher quality reflecting surface corresponds to the long-range correllated texture for the low temperature process.

Conductances for all three systems of the gels (Tables 2.3-VI and 2.3-VII) were greater for the liquid nitrogen cooled gels than those of the ambient. For both of the ultraviolet-cured systems, the ambient conductances are a small fraction of those prepared at the lower temperature. The Dielectric Gel processed at low temperature conducted for both metals, as contrasted with that prepared by the ambient evaporation where no conduction was measured. This is a striking result when compared to the ultraviolet cured materials.

2.3.8 The Characterization of the Indium Metallization

The indium deposition for ambient conditions yielded a brown-colored film which was transparent. For System A, with curing times of 1 and 2 minutes, a variety of colors, which ranged from white to pink to purple were observed on the surface. For low temperature evaporation, the indium had a mirror-like surface and, unlike aluminum, did not appear to have any cracks.

The reflectances of the indium surface (Table 2.3-VII) were high for both processing temperatures for System A, while for System B, the low temperature process yielded a greater average reflectance.

The results for the conductance for indium were similar to those of aluminum in that none of the gels conducted under the condition of ambient evaporation, whereas, for the low temperature evaporations, the metal films were conducting.

Little variation was noted in the conductivity for different crosslink densities. It appears that there may be a greater surface migration for indium than for aluminum and that its interaction with silicone allows a similar film to be formed on all of the silicone gels (10).

To further investigate the temperature dependence of the substrate on the metallization, the reservoir was cooled by an acetone-dry ice bath to 180 K. This temperature is above that of the glass transition of the polymers. Samples for System B were metallized at this temperature and the resulting conductances for both aluminum and indium are listed in Table 2.3-VIII.

The values of the conductances were intermediate between those at 300 K and those below the glass transition temperature (T_g) for both metals. The results for indium were more sensitive to the substrate temperature. At a substrate temperature of 300 K the indium films did not conduct, whereas, for both low temperatures, the films were conducting. There appear to be several competing mechanisms responsible for the values

Table 2.3-VIII

Conductances of Al and In Films Prepared at 180 K

System	Cure Time(min.)	Conductances (10^{-2} S) (a) Al	In
B	5	5	4
	10	7	14
	15	7	17

a) The values of the order of magnitude are reliable, although there was spread in data values.

of the conductances which include the primary and secondary nucleation kinetics (11) and metal diffusion in the crosslinked networks (12). The substrate temperature sensitivity of the conductance indicates that a nucleation mechanism is predominant rather than the glassy state of the substrate. However, further analysis of the substrate temperature dependence on the metallic penetration into the polymer is needed as this may also be an important factor in the conductance.

2.3.9 Conclusions

The inference that metallization onto a glassy rather than a rubbery polymer would yield a metal surface with improved electrical and optical properties is supported by the experimental results. A substrate cooled above the glass transistion temperature also yields better conducting films than those of an ambient substrate. This indicates a nucleation mechanism may be responsible for the substrate temperature dependence of the film. The average reflectance and conductance values for all the gels prepared by the low temperature processing were higher than those of ambient processing conditions. An improved reflectance is also found for metal films with low temperature processing. This is in agreement with larger and smoother sections occuring on the metal surface of these gels.

The reflectance and conductance values for the metal film processed at low temperature also varied with the metal used, aluminum or indium, the silicone system and the curing time. Among the gels, the aluminum films on the ultraviolet cures of System B yielded the largest values for both reflectance and conductance.

References:

1. L.R.G. Treloar, The Physics of Rubber Elasticity, 3rd Edition, Oxford University Press, (1975).

2. A.M. Bueches, J. polm. Sci., 15, 97 (1955).

3. Dow Corning Corporation, Midland Michigan.

4. A. Schwartz, J. B. Weisbrook, and D. T. Turner, ACS Polymer Preprints, 20 (2), 443 (1979).

5. G. C. Martin, T. T. Su, P. Kornreich, and S. T. Kowel, "The Photochemical Lithography of Silicone Elastomers" presented at the Symposium of Polymeric Materials for Electronic Applications, ACS 180th National Meeting, Las Vegas, Nevada (1980); ACS Organic Coatings and Plastics Chemistry Preprints, 43, 390 (1980).

6. L. T. Thompson, and R. E. Kerwin, Ann. Rev. Mat. Sci., 6, 267 (1967).

7. S. T. Kowel, and P. G. Kornreich, Polymer Microelectronics, Proposal submitted to the National Science Foundation, Syracuse University (1978).

8. E. Balizer, T. T. Su, G. C. Martin, P. G. Kornreich, and S. T. Kowel, to be published.

9. K. E. Polmanter, and M. J. Hunter, J. Appl. Polym. Sci., 1, 3 (1959).

10. J. M. Burkstrand, Polym. Prop., ACS Div. of Polym. Chem., 21, (1), 132 (1980).

11. C. A. Neugebauer, in Handbook of Thin Film Technology, edited by L. I. Maissel and R. Glang, (McGraw Hill, New York, 1970), p. 6 -8.

12. J. P. Crine, J. F. Currie, S. Sapilha, and A. Yelon, Annual Report CEIPD, 69 (1979).

2.4 FTIR Studies of PDMS

In this section, the IR spectra of the silicone gel Systems A, B, and the Dielectric Gel taken by FTIR are presented. The windows of the first set of spectra were MgF_2 (supplied by NVEOL) and had a cut-off at 1000 cm^{-1}. A second set of spectra were taken with KBr windows to allow for lower wave numbers. The absorption bands were correllated to the silicone polymer bond structure. This enabled the kinetics of crosslinking to be followed by the change in absorbance of reactive bands. In addition, absorbance measurements were taken for System A which yield information on polymer interactions.

2.4.1 The Spectra of System A, System B, and Dielectric Gel

Samples of System A, System B, and the Dielectric Gel were coated on the MgF_2 windows supplied by NVEOL. The systems were crosslinked for the following exposure times: System A - 5 mins., System B - 10 mins., by UV; and Dielectric Gel - 30 mins. at 413 K. The windows were found to transmit between 5000 to 1000 cm^{-1} wave numbers. FTIR spectra were taken for the polymer coated windows over this region. The measured transmission spectra are shown in Figs. 2.4-1, 2.4-2, 2.4-3, for Systems A, B, and the Dielectric Gel respectively. Although structure in the transmission spectra occurs throughout the interval, a sharp absorption is noted at about 3000 wave numbers. This is a sharp absorption for the Dielectric Gel and broadens for Systems A and B. The Dielectric Gel had the greatest transmission range as compared to Systems A and B.

The structure of the spectra and relatively low transmission for Systems A and B indicate that the ultraviolet active side groups

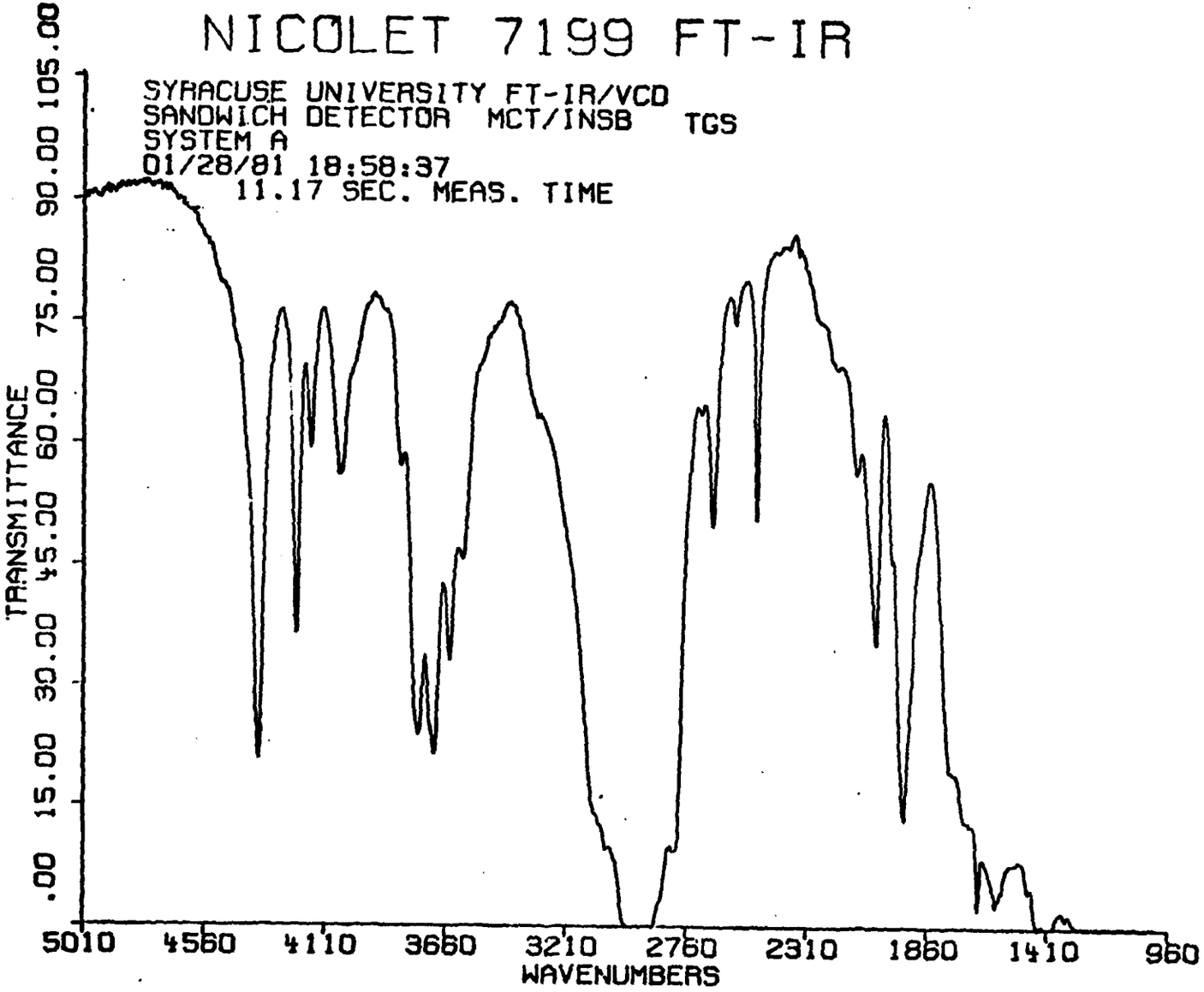

Figure 2.4-1 Infrared Transmission Spectra for Crosslinked System A.

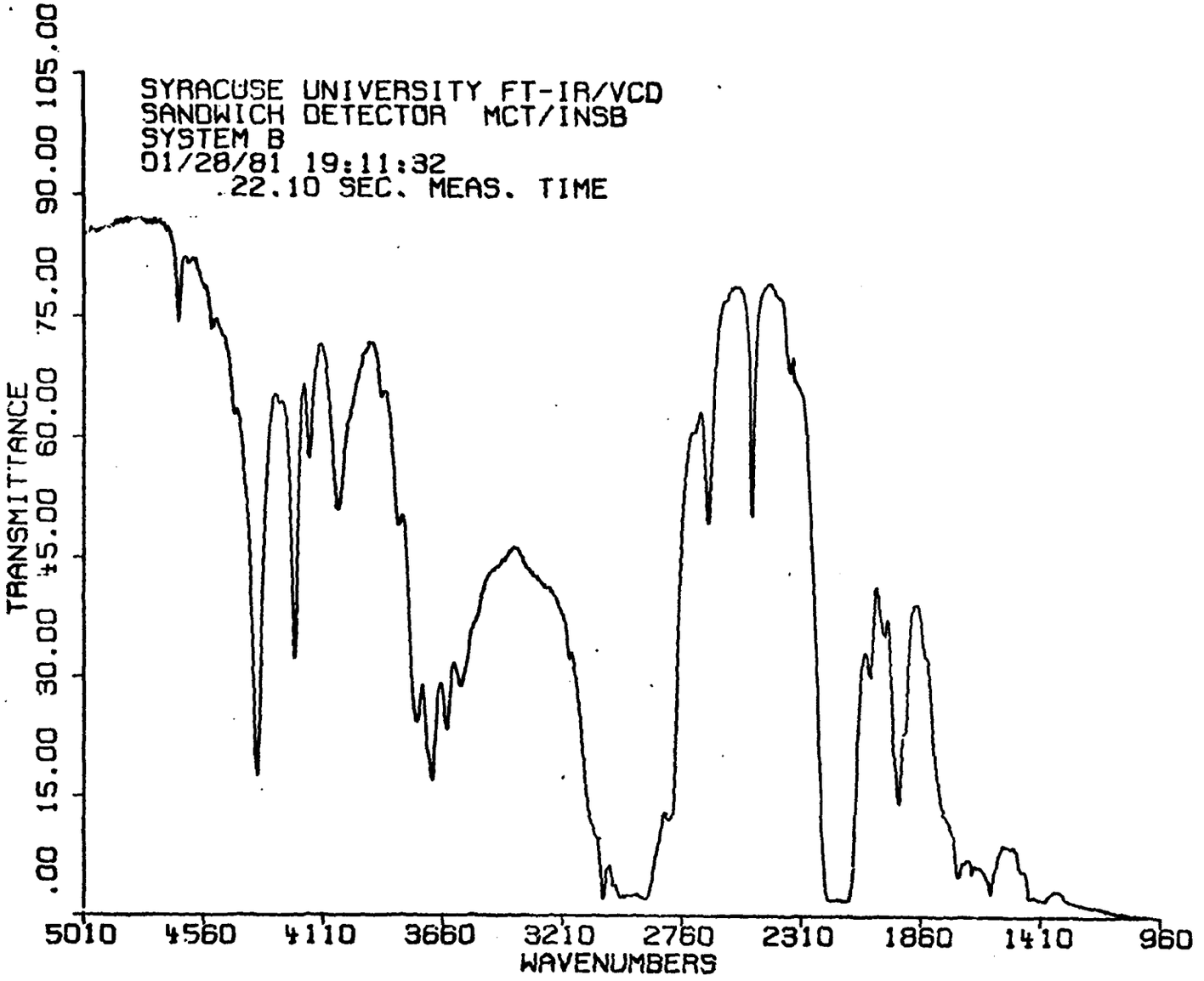

Figure 2.4-2 Infrared Transmission Spectra for Crosslinked System B.

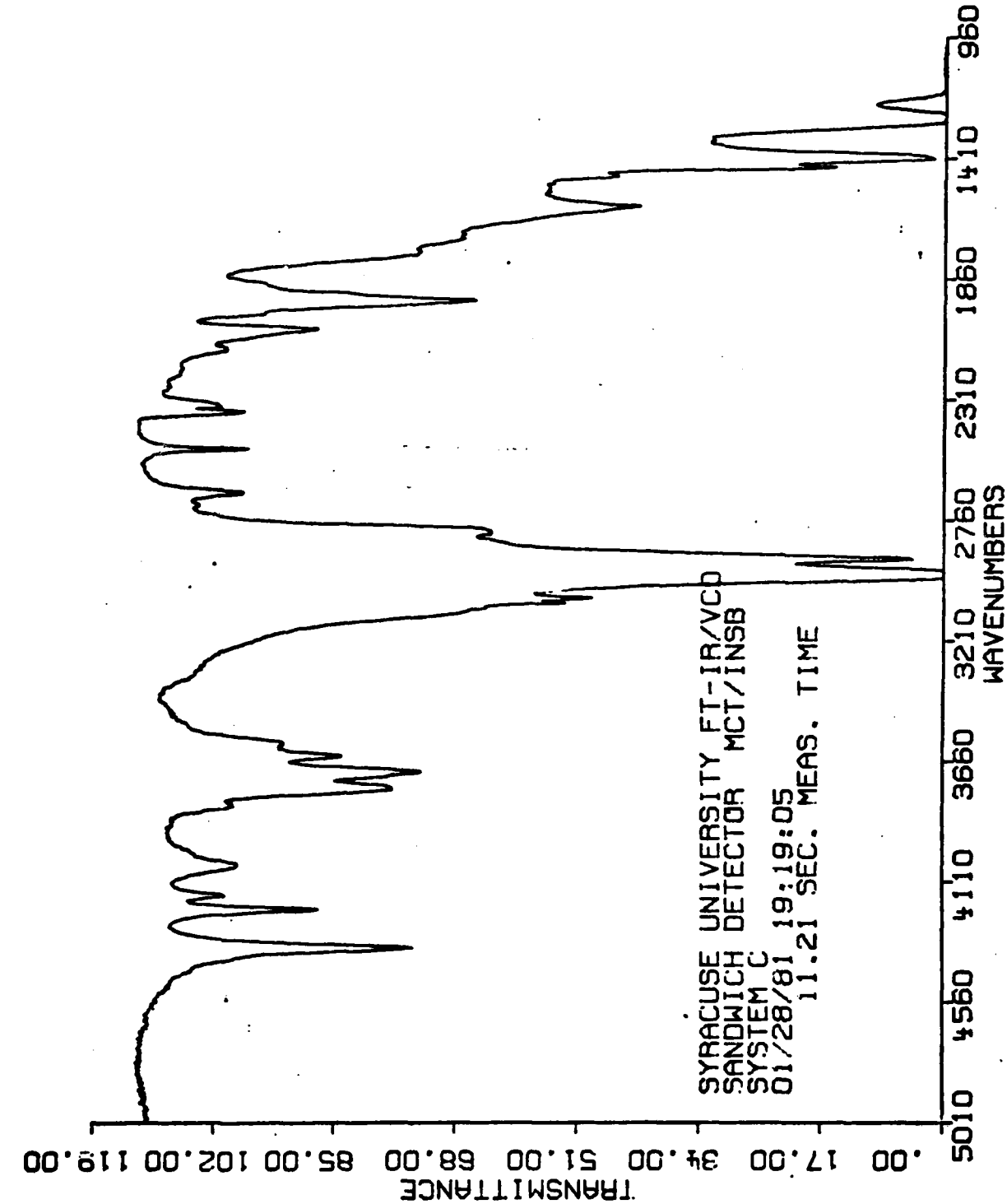

Figure 2.4-3 Infrared Transmission Spectra for Crosslinked Dielectric Gel.

are absorbing in the IR. If this is so, the transmission spectrum may be used to characterize the crosslink density and, hence, the modulus of the microstructure. In order to separate out the silicone bands, we have identified each band occurring in PDMS and listed them in Table 2.4-1.

Table 2.4-I

Bands for Determination of Crosslink Density [1]

Bond	Wave Number (cm^{-1})	Description of Band or Mode
Carbon		
C = C	1680 - 1620	Stretching; Variable intensity
	1750 - 1760	Stretching; medium intensity
Methyl Group		
C - H	2959	C - H stretch in $SiCH_3$
Si - C	800	Si - C bending in $Si(CH_3)_2$
CH_3	1377	CH_3 bending
C - H_2	1263	C - H_2 rocking
C - H	1421	C - H bending
Silicone		
Si - O	1080 - 1020	Intense band in Polymers of Silicone and Oxygen due to vibrations.

The strong absorption for the silicones at 3000 cm^{-1} can be correllated to the C-H stretch as listed above. The remaining modes are near the low wave number cut-off region of the windows. In Fig. 2.4-4, the transmission spectra for dimethyl and phenyl substituted silicones are shown.[1] There is very little structure in the region of 5000 to 1400 wave numbers as compared to our IR spectra. The structure is believed to be caused by crosslinkable active groups.

2.4.2 Crosslinking Kinetics of System A

By extending the IR measurements into the low wave number region with KBr windows, identification of the crosslink active side group bands and quantitative measurements of crosslinks may be made. We have therefore retaken the IR spectrum of System A with KBr windows, which allows bands in the lower wave number region, from 1200 to 400 wave numbers to be observed. We have identified those bands which are affected by ultraviolet crosslinking.

The spectra for the kinetics of crosslinking are shown in Figs. 2.4-5 to 2.4-7 for which a System A silicone gel was consecutively cured for 1, 2, and 4 minutes respectively. The scans were taken from 4600 to 400 cm^{-1}. By comparing Figs. 2.4-5 and 2.4-6, we notice no new bands occurring. The transmission scale for Fig. 2.4-7 was enlarged for ease of band determination and is presented in Fig. 2.4-8. We notice here that at about 1000 wave numbers there is a sharpening of a band that does not occur in Figs. 2.4-5 and 2.4-6.

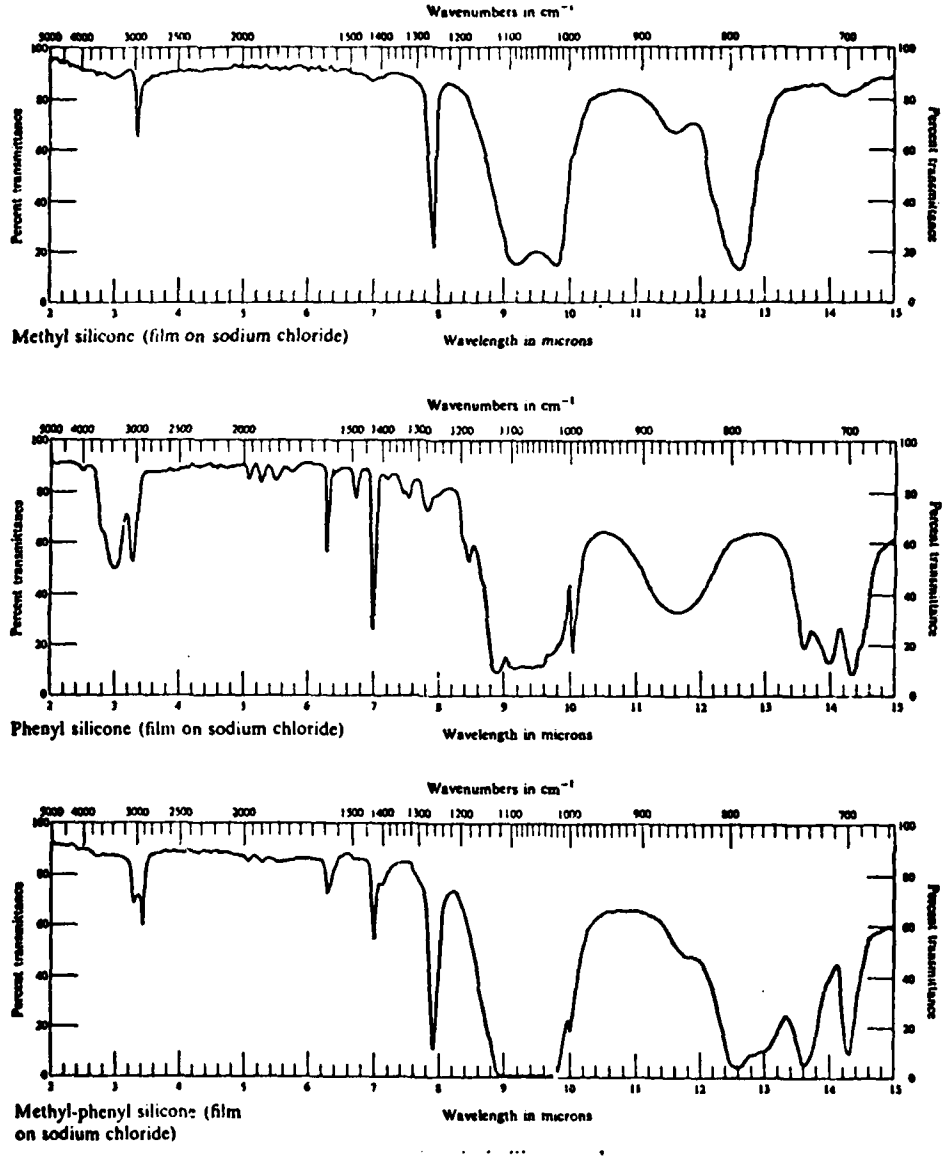

Figure 2.4-4 Spectra of Typical Silicone Polymers From Reference 1.

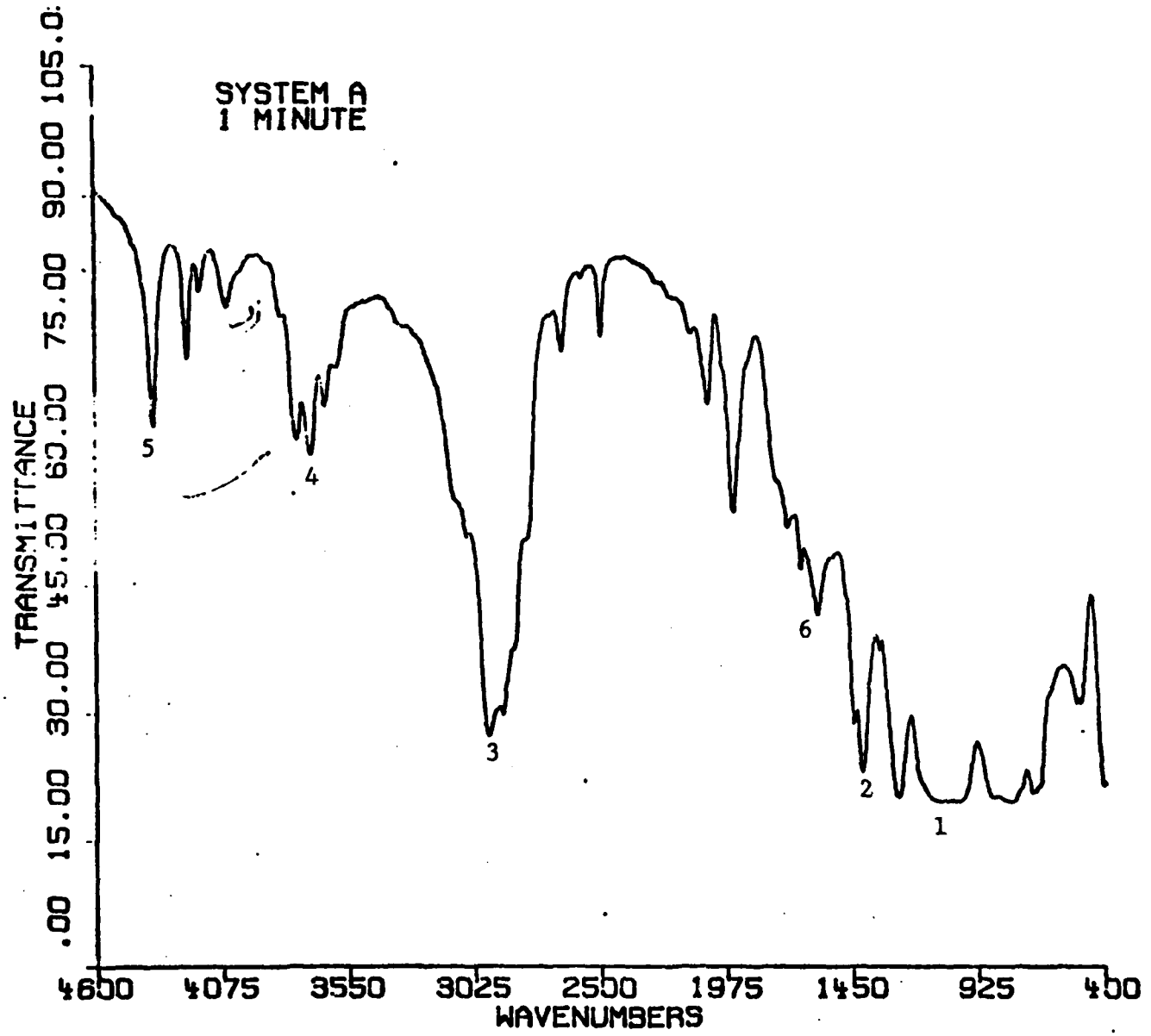

Figure 2.4-5 Transmittance of System A cured for 1 Min. The six bands used for the crosslinking kinetics of System A are labelled.

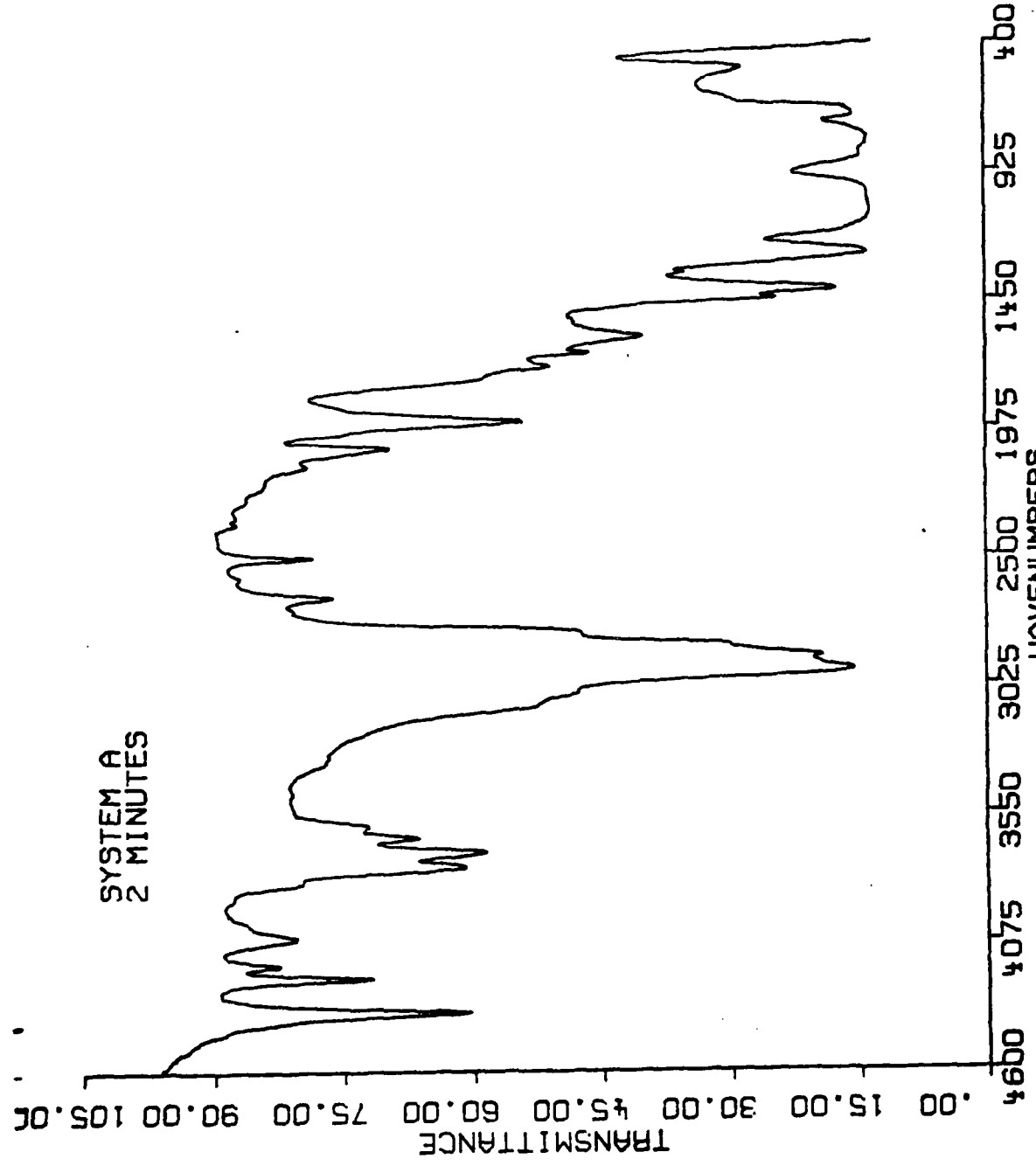

Figure 2.4-6 Transmittance of System A Cured for 2 Mins.

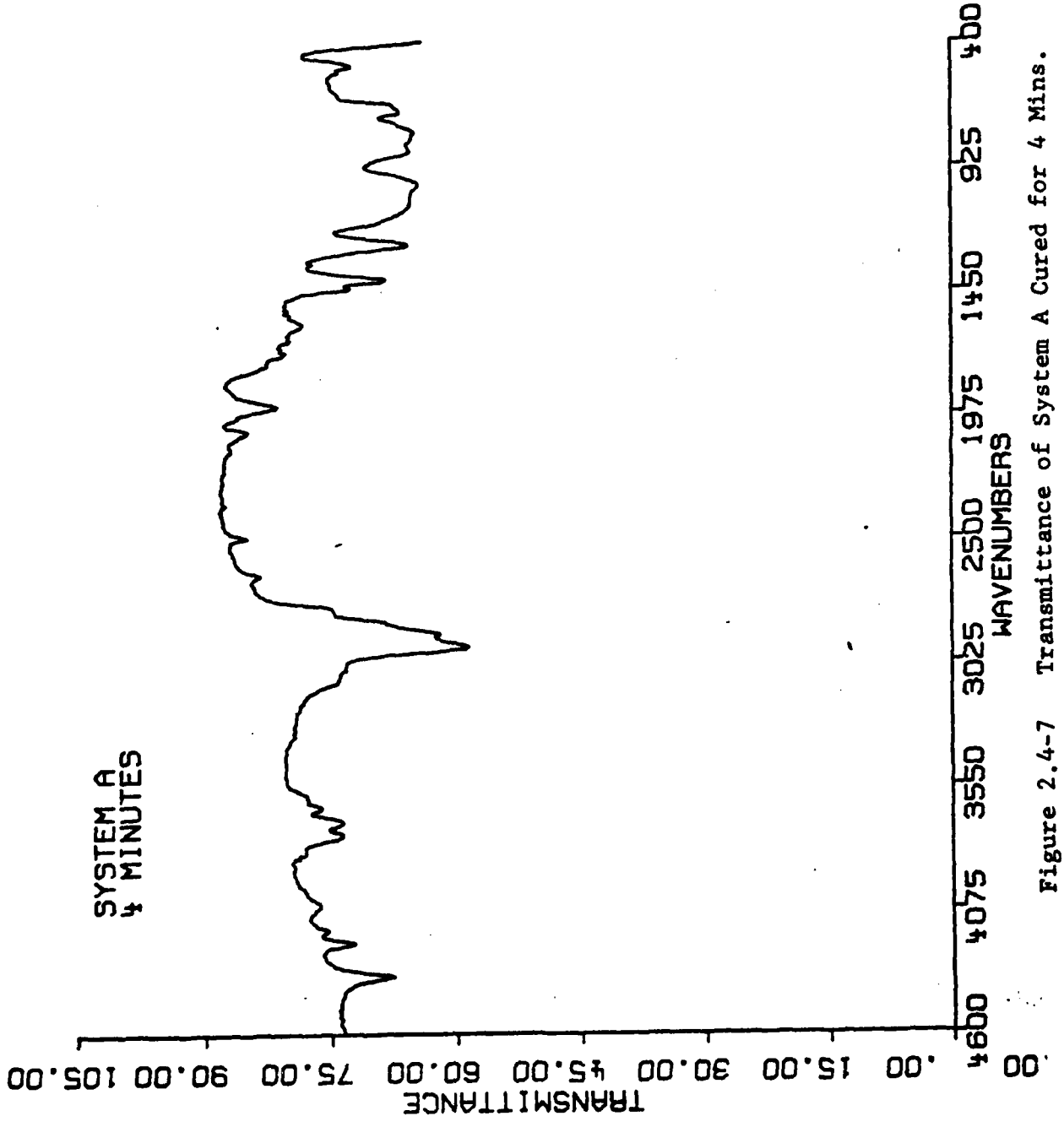

Figure 2.4-7 Transmittance of System A Cured for 4 Mins.

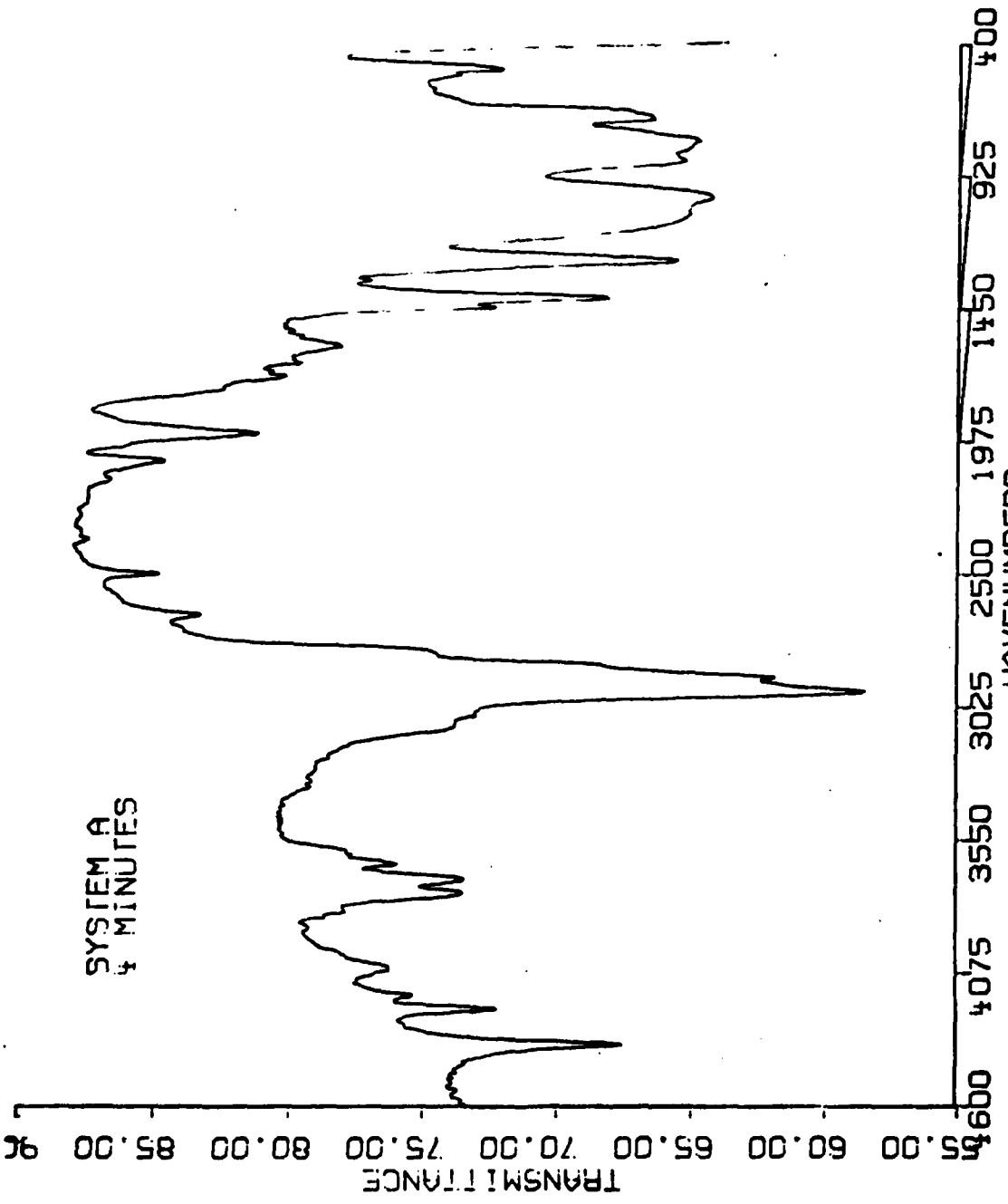

Figure 2.4-8 Enlargement of the Transmittance of System A Cured for 4 Mins.

For the 1 and 2 minute cures the transmission monotonically increased above 3000 wave numbers, whereas, for the 4 minute cure there was a monotonic decrease in transmission for this region. We therefore find that U.V. curing appears to increase the opacity of the gels for the higher wave numbers on the border of the near infrared ($4000cm^{-1}$).

In order to determine changes in the bands due to crosslinking, six reference bands were chosen as marked in Figs. 2.4-5 - 2.4-7. According to Beer's Law, the absorbance, as defined below, is directly proportional to a selected bond or concentration as follows:

$$A = \log (1/T) = abc \qquad (2.4\text{-}1)$$

where A = absorbance

T = transmission

b = path thickness

a = frequency dependent cross section

c = concentration of substance or bond of interest

By forming the ratio of the absorbance of a non-reactive bond (constant concentration) such as $Si\text{-}CH_3$ or Si -O to a U.V. reactive double bond C = C, the kinetics of crosslinking (opening of C = C) may be followed. As noted from Eq. 2.4-1, this ratio is independent of sample thickness.

The six bands identified in Fig. 2.4-5 are listed below in Table 2.4-I.

Table 2.4-I (Band Identification)

Peak Number	Band
1	SiO band
2	CH_3 bending
3	C - H stretch
4	--
5	--
6	C = C band

The values of the transmission of the bands as a function of time are listed in Table 2.4-II.

Table 2.4-II

Transmission Values (T) as a Function of Time

Peak(% Transmission)	1	2	3	4	5	6
Time(min)						
1	19	23	27	60	64	62
2	13	17	15	58	61	40
4	64	68	59	74	67	78

The absorbances calculated for bands 1, 2, 3, and 6 are

Table 2.4-III

Absorbances (-ln T)

Band No.	Time(min)		
	1	2	4
1	.721	.886	.193
2	.638	.769	.167
3	.568	.823	.229
6	.376	.397	.107

Forming the ratios of the absorbance of band 6(C = C) to bands 1, 2, and 3,we found the relative change of the carbon double bond due to crosslinking as listed in Table 2.4-IV.

Table 2.4-IV

Relative Absorbances of Band 6

	Time(min)		
Relative Band	1	2	4
3	.662	.482	.467
2	.589	.516	.640
1	.521	.448	.554

We observed that the relative absorbance of the C = C band to the C - H stretch band (band 3) decreased for the 2 minute cure and has a slightly lower value for that at 4 minutes. This appears to match the trend of the previous results presented for the % extractables for System A in the bulk, which are shown in Fig. 2.3-1. At present we do not know why this trend does not occur for bands 1 and 2.

2.4.3 Crosslinking Kinetics of System B

FTIR spectra were also taken for System B in order to study the kinetics of crosslinking. The sample was prepared by placing a drop of System B on a KBr window. The drop was successively exposed to U.V. for 5, 10, and 15 minutes. The values of the transmission and absorbance spectra were measured by IR for each curing time. The recorded transmission and absorbance spectra

in order of increasing cure times are in Figs. 2.4-9 to 2.4-16. A list of the bands chosen to yield ratios of relative absorbance is given in Table 2.4-V.

The absorbances for each band were read from digital output on the FTIR.

Table 2.4-V

Absorbances for Cures of System B

Absorbances

Band (cm^{-1})	Cure Time (min.)			
	0	5	10	15
800.0	2.00	2.04	1.88	2.15
1597.0	0.08	0.09	0.10	0.13
1667.5	0.07	0.05	0.00	0.00
1724.0	0.00	0.06	0.11	0.16
2168.6	1.03	0.97	0.83	0.86
2964.0	1.37	1.46	1.27	1.46

2.4.4 Description of Spectra

We observe from the Figs. 2.4-9 to 2.4-16 that in the region of 1600 wave numbers, one peak at 1667.5 cm^{-1} decreases with curing time and another at 1724 cm^{-1} increases. The carbon double bond stretching occurs at about 1600 cm^{-1} for conjugated bonds and as high as 1670 cm^{-1} for the nonconjugated species. The

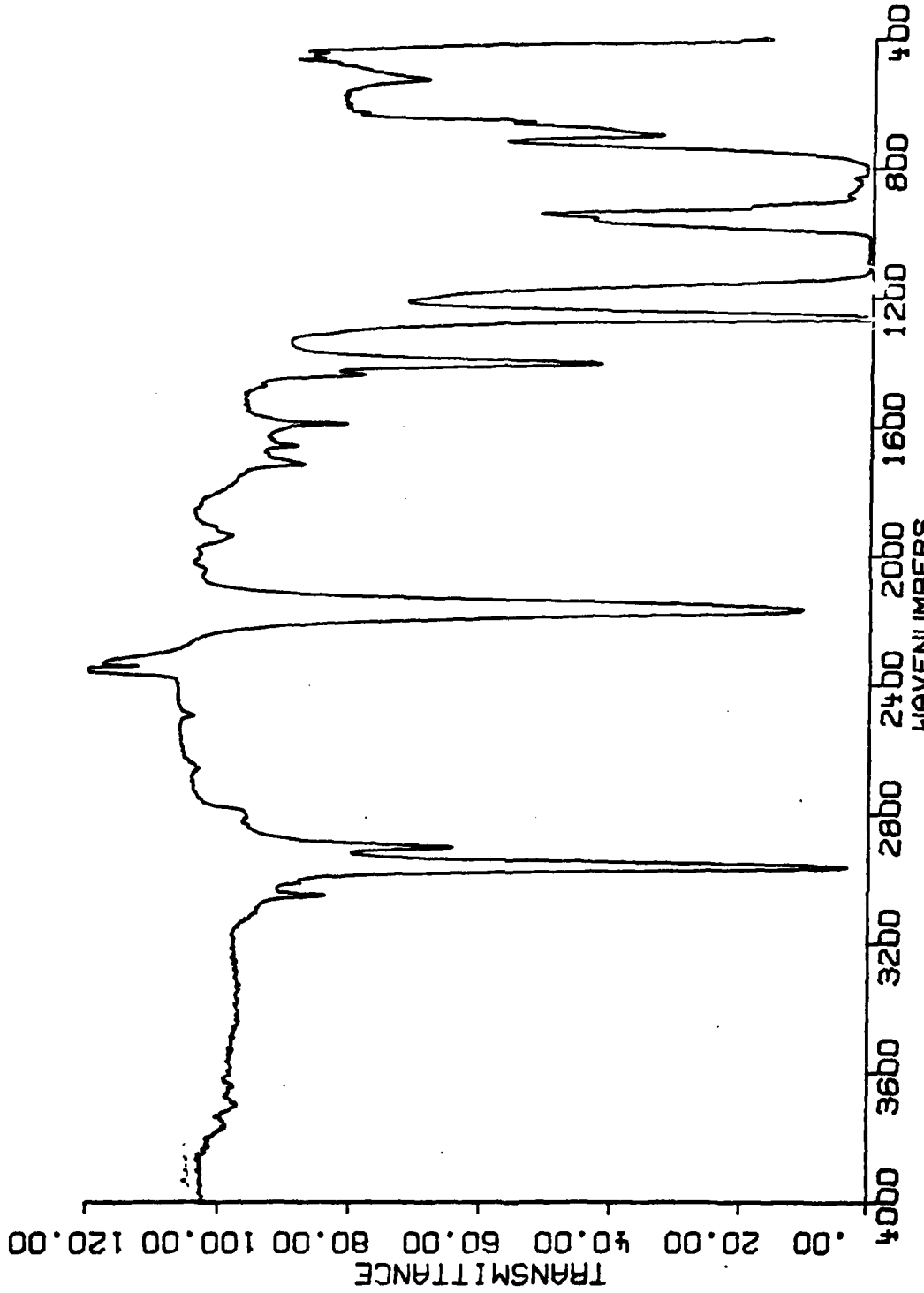

Figure 2.4-9 Transmittance of Uncured System B

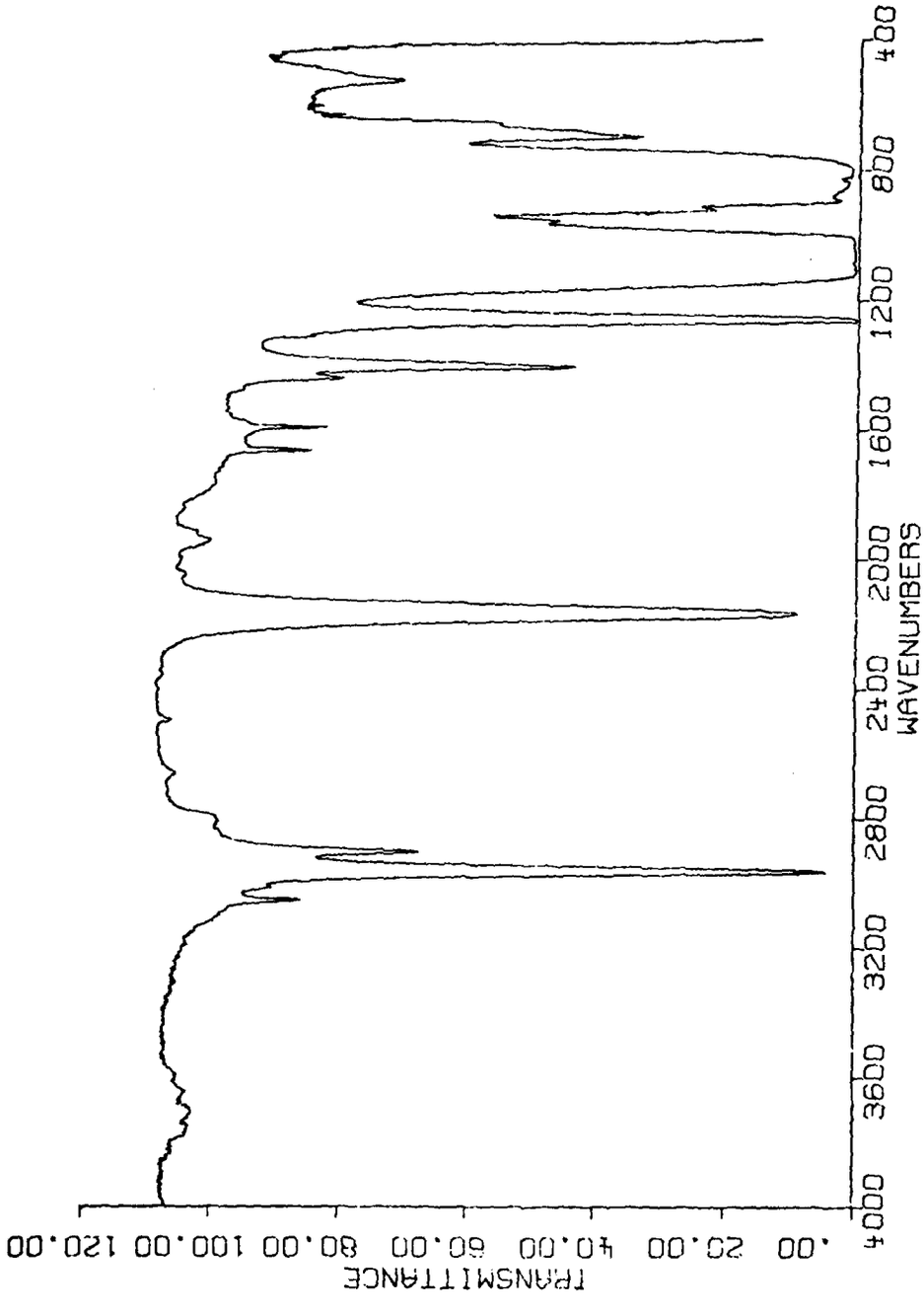

Figure 2.4-10 Transmittance of System B Cured for 5 Mins.

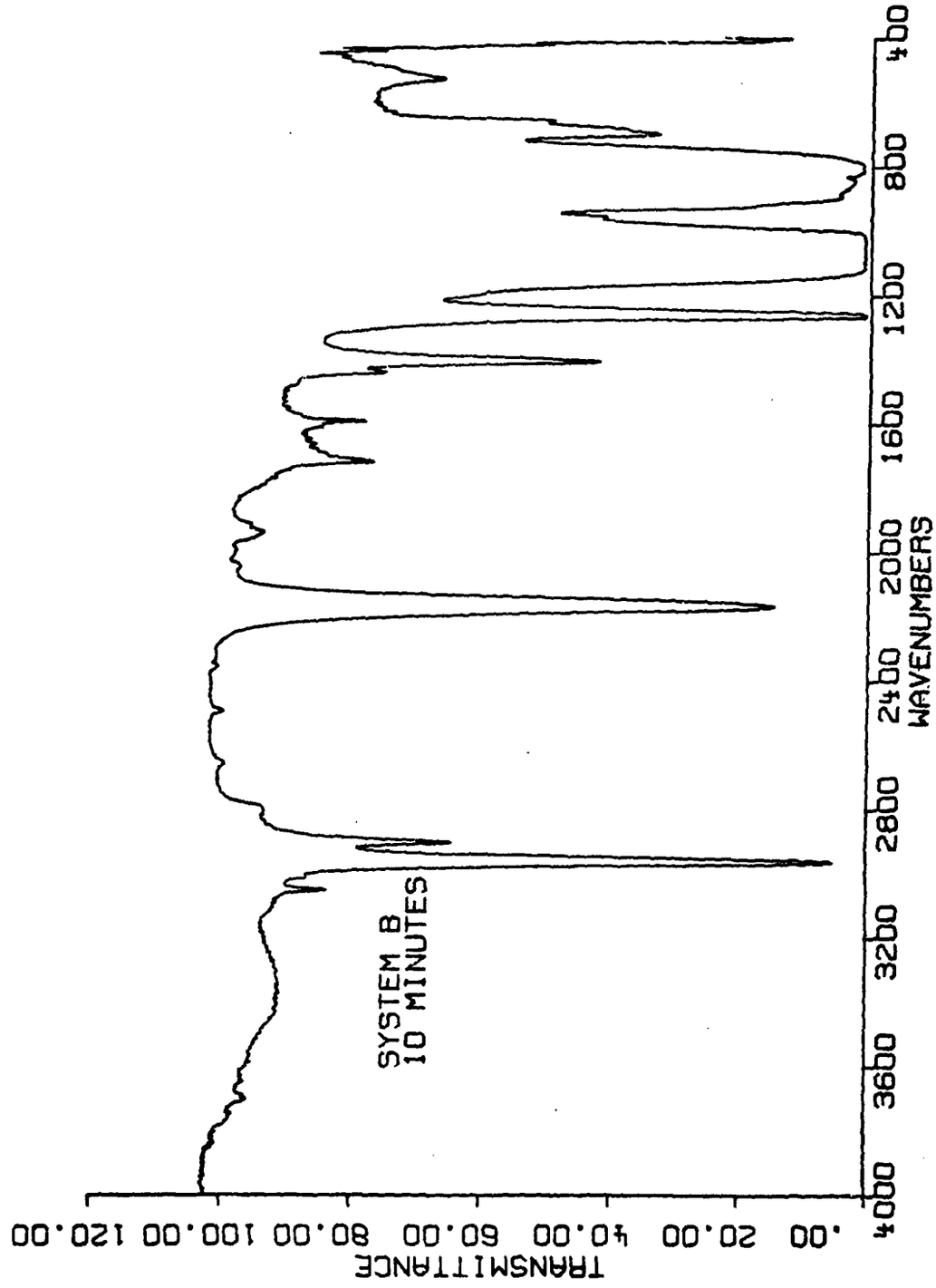

Figure 2.4-11 Transmittance of System B Cured for 10 Mins.

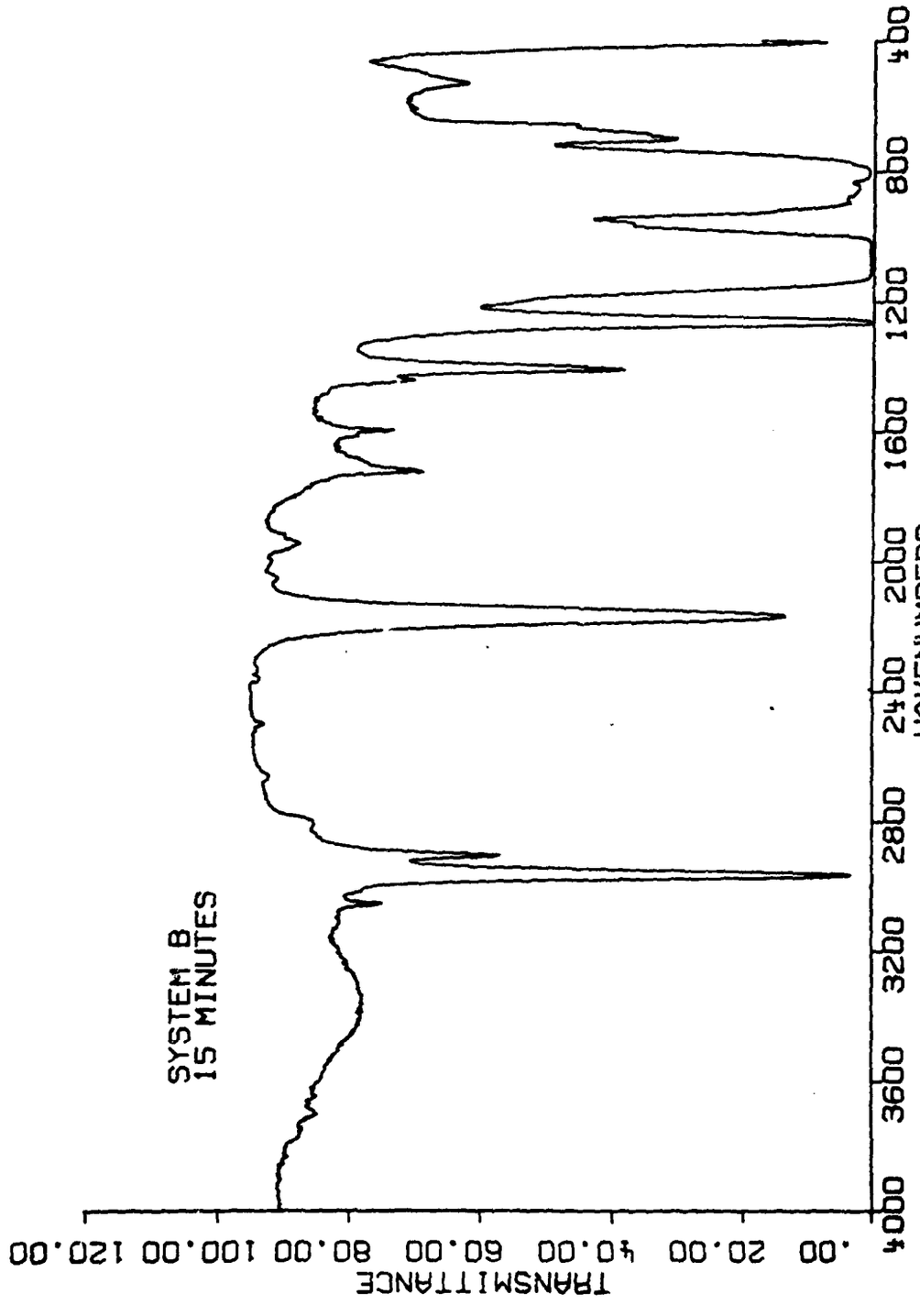

Figure 2.4-12 Transmittance of System B Cured for 15 Mins.

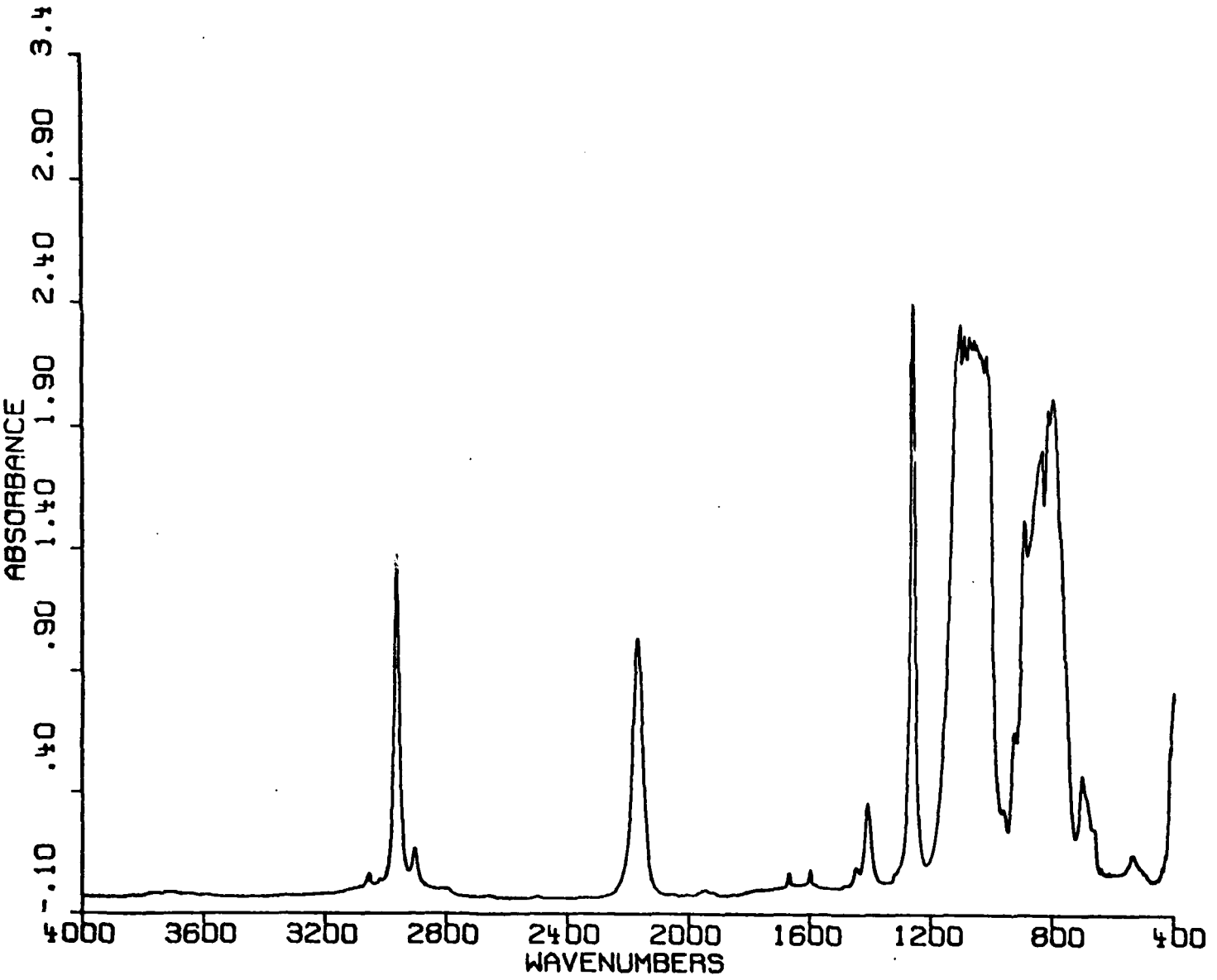

Figure 2.4-13 Absorbance of Uncured System B

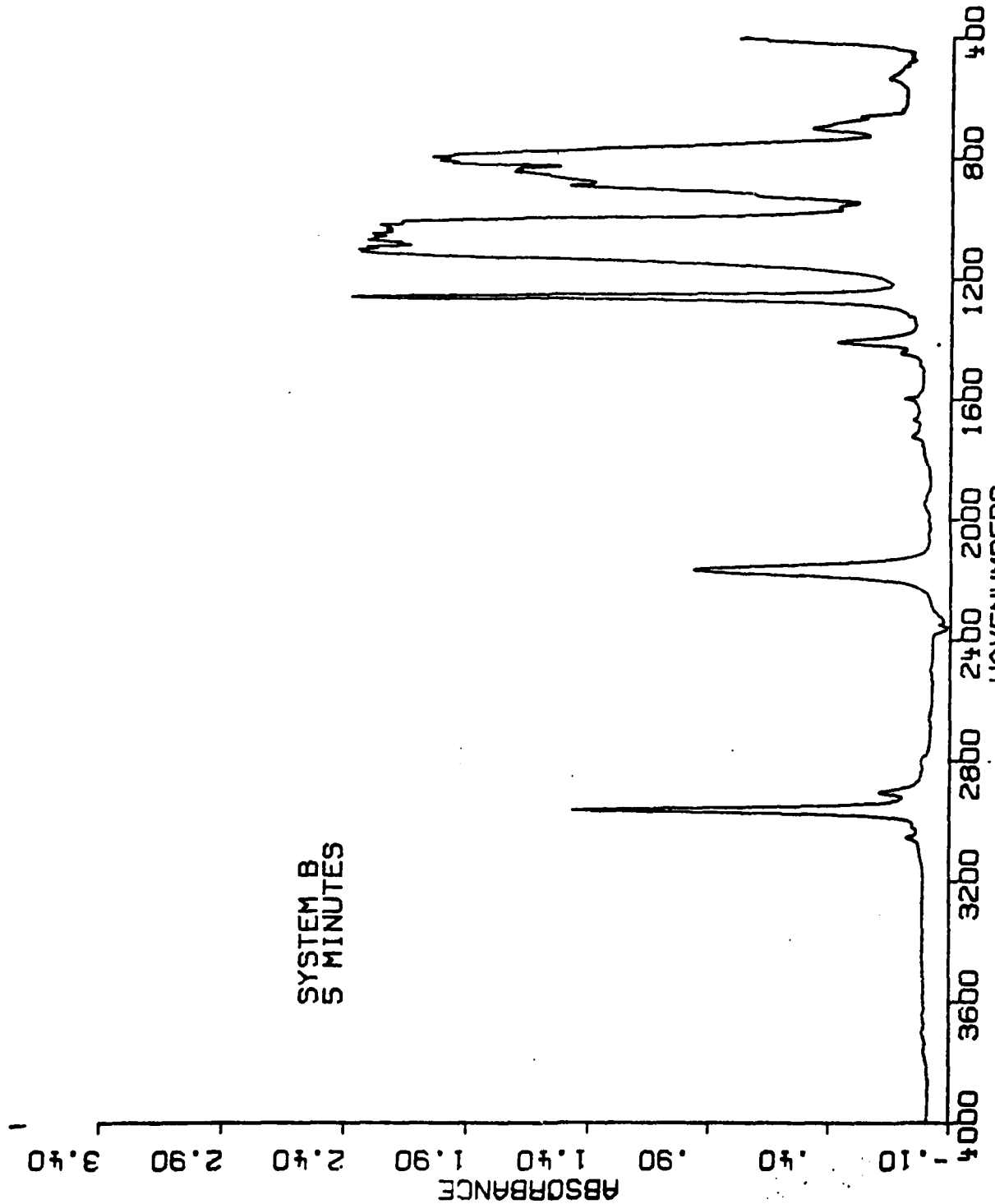

Figure 2.4-14 Absorbance of System B Cured for 5 Mins.

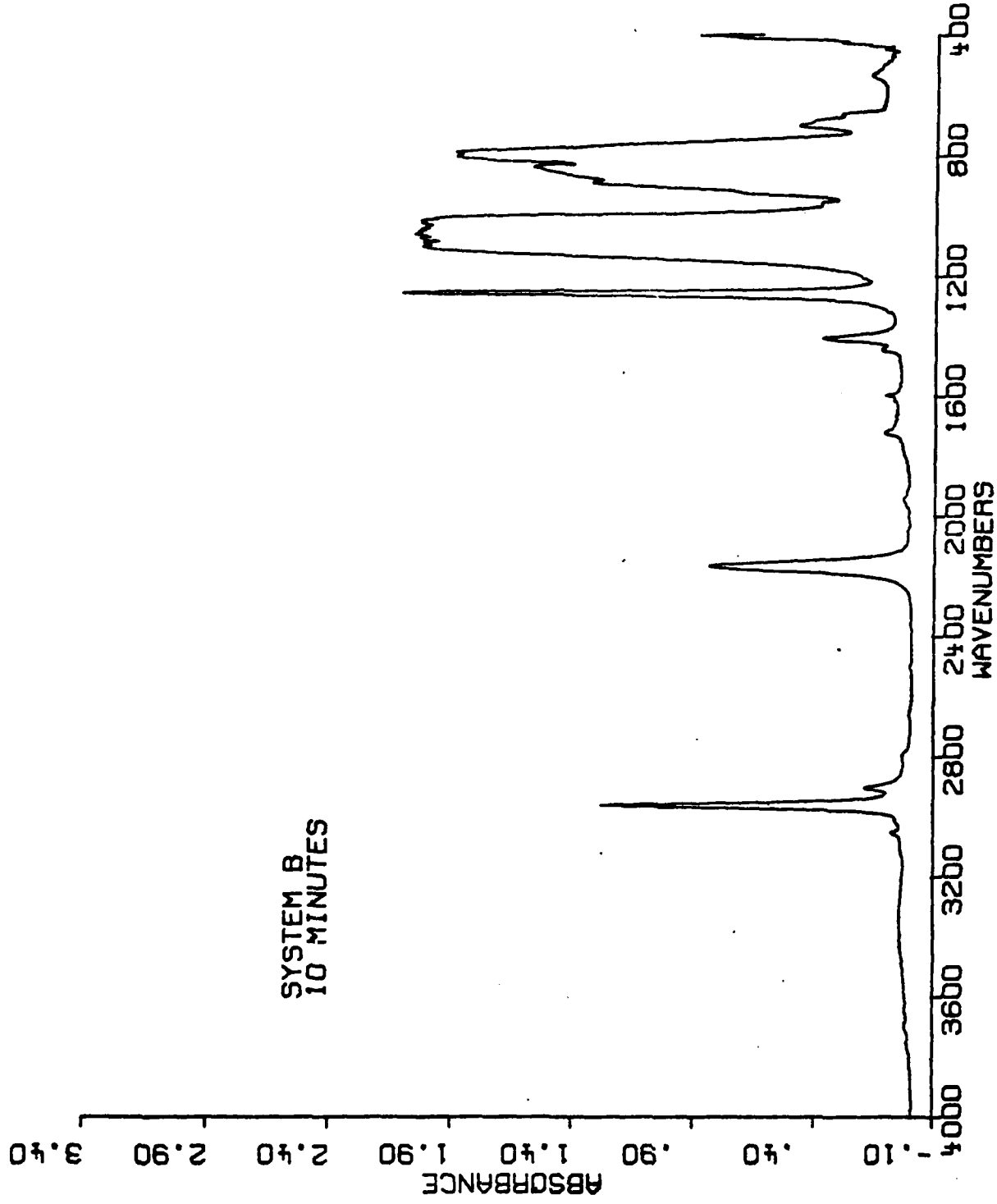

Figure 2.4-15 Absorbance of System B Cured for 10 Mins.

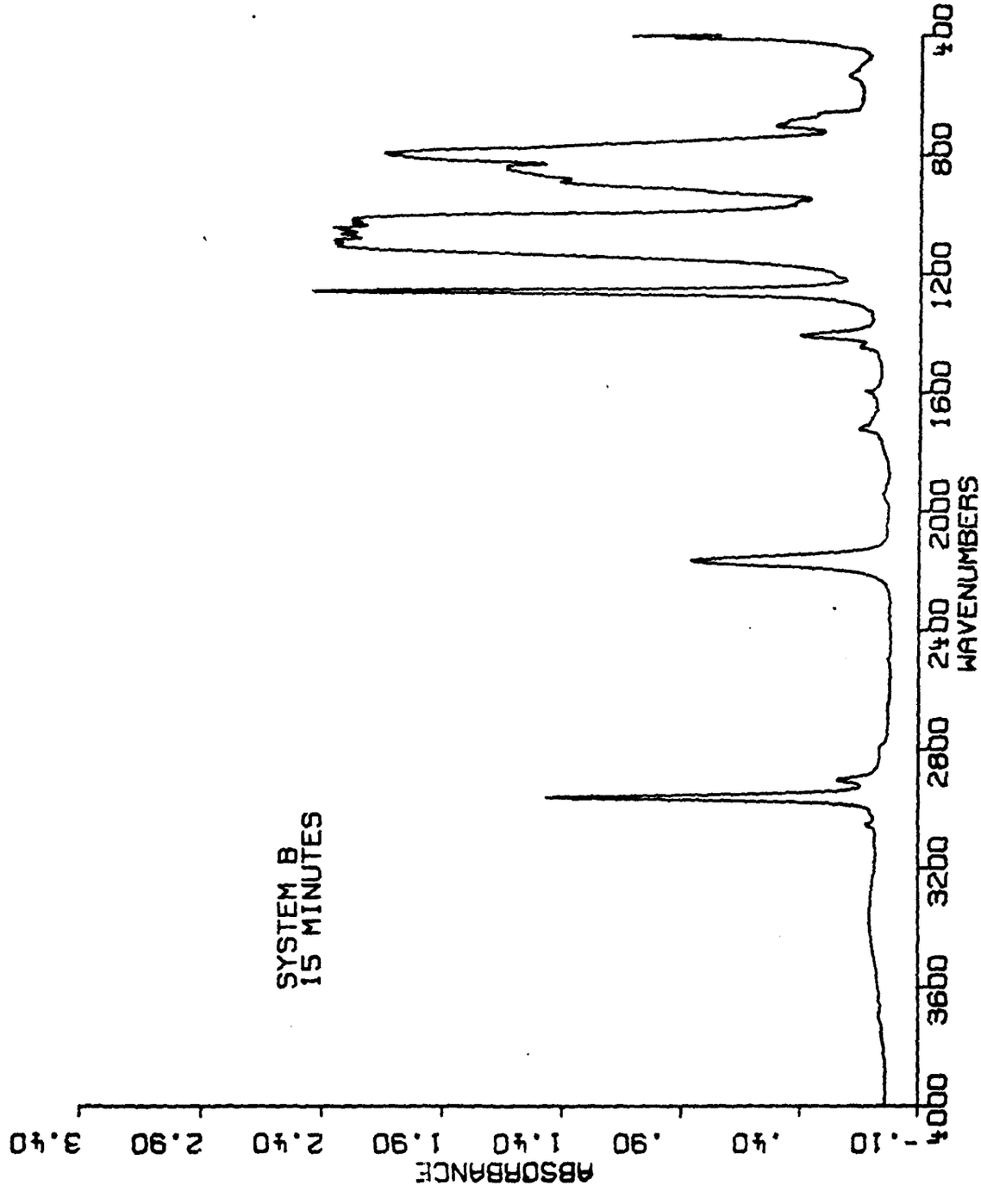

Figure 2.4-16 Absorbance of System B Cured for 15 Mins.

double bond transmittance is very weak in the unconjugated case, but very intense for conjugated cases [2]. This is in agreement with the value of 1667.5 assigned to the C = C bond as the PDMS structure does not have conjugation.

We also note that for wave numbers of about 3350 there is an absorption peak developing. This could be due to water absorption on the samples, which also has a broad absorption at these wave numbers. A more pronounced effect of the transmittance reduction was found for System A in the region of 3000 - 4000 wave numbers.

We expect that the bands at 2964 cm^{-1} (C-H stretch) and 800 cm^{-1} (Si-C stretch) remain unchanged during the crosslinking reaction. In order to trace those bands active in the crosslinking kinetics, the relative absorbances were calculated relative to the C-H and Si-C bands. This method of ratios normalizes the results for different thicknesses of the polymer film scanned by the IR. The relative absorbances are listed in Tables 2.4-VI and 2.4-VII.

Table 2.4-VI

Absorbances Relative to C-H Band

Cure Time(min.)	Band (cm^{-1})					
	800	1597	1667.5	1724	2168.62	2964
0	1.45	0.06	0.05	0.00	0.75	1.00
5	1.39	0.06	0.03	0.04	0.66	1.00
10	1.48	0.08	0.00	0.09	0.66	1.00
15	1.47	0.09	0.00	0.11	0.59	1.00

Table 2.4-VII

Absorbances Relative to Si-C Band

Cure Time(min.)	Band (cm^{-1})					
	800	1597	1667.5	1724	2168.6	2964
0	1.00	0.04	0.04	0.04	0.52	0.80
5	1.00	0.04	0.02	0.03	0.47	0.72
10	1.00	0.05	0.00	0.06	0.44	0.67
15	1.00	0.06	0.00	0.07	0.40	0.68

Except for the data for the 5 minute cure, the absorbances for the C-H and Si-C bands are fairly stable. The 2168 band and the C = C band at 1667 decrease during the curing as expected. However, as indicated by the absorbance data, the crosslinking kinetics appears to saturate after 5 minutes of curing. For a more complete study, data is needed within this time interval.

2.4.5 The Absorbance of System A

The absorbance in the infrared as a function of the silicone thickness was measured for System A. The uniform films were prepared by using mylar strips as spacers. The thicknesses varied between 6.4 μm to 50.8 μm and are listed in Table 2.4-VIII. A drop of silicone was deposited on a KBr window between the mylar strips, and then drawn down by the edge of a microscope slide guided by the spacers. This drawdown was repeated in case polymer relaxation caused the thickness to increase. The films and substrate were then exposed to U.V. for 5 mins. This is the time needed to obtain near maximum curing according to sol-gel content analysis presented in Section 2.3.3.

The IR absorbance curves for two sample thicknesses of 6.4 μm and 23.4 μm are illustrated in Figs. 2.4-17 and 2.4-18. Although the absorbances increase, as expected, for the thicker sample, there appears to be structure in the peaks for the 23.4 μm sample. This indicates that new bands may occur when increasing the volume of the gel. These new bands indicate a polymer - polymer interaction in the gel with

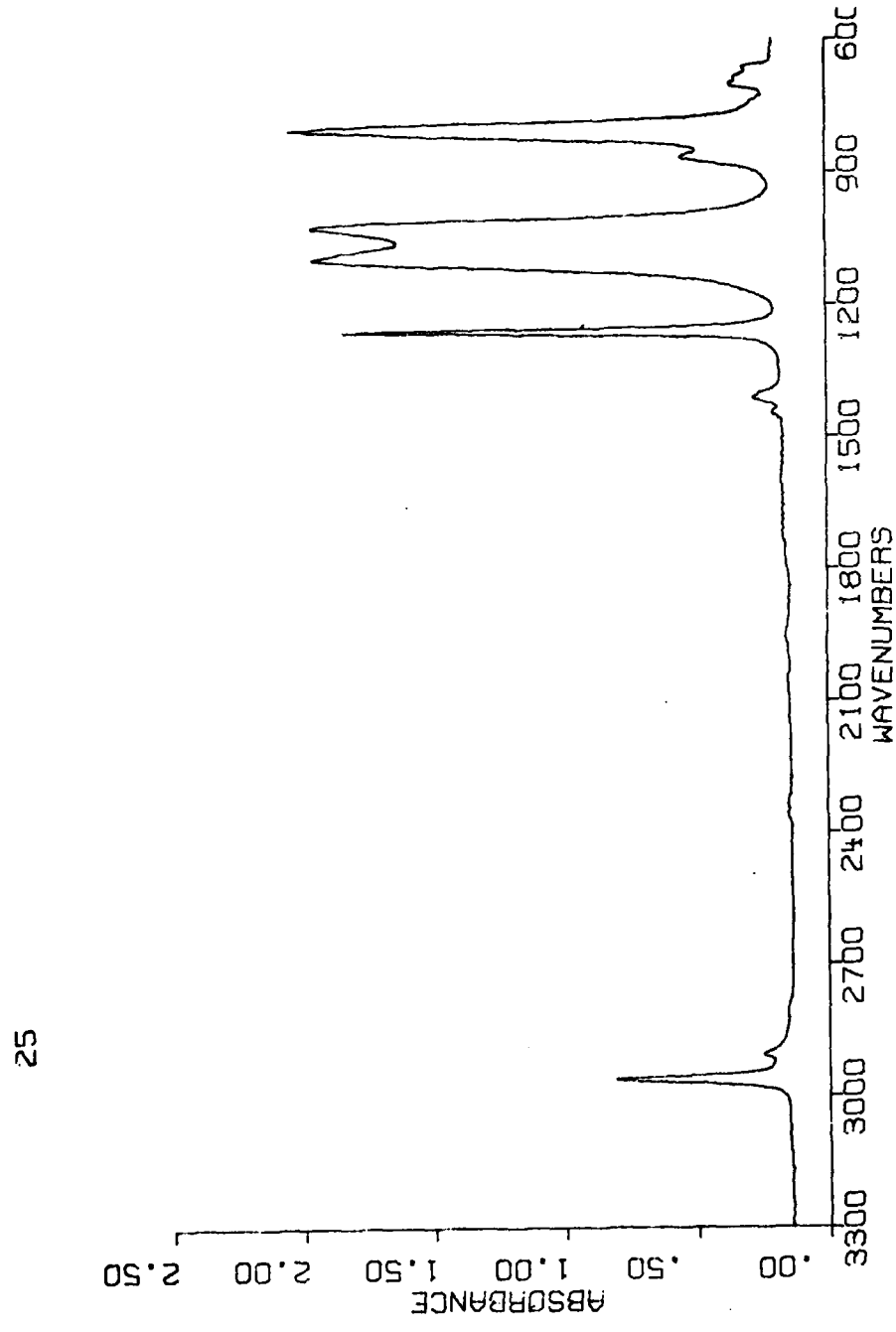

Figure 2.4-17 Absorbance of a 6.4μm thick gel of System A Cured for 5 Mins.

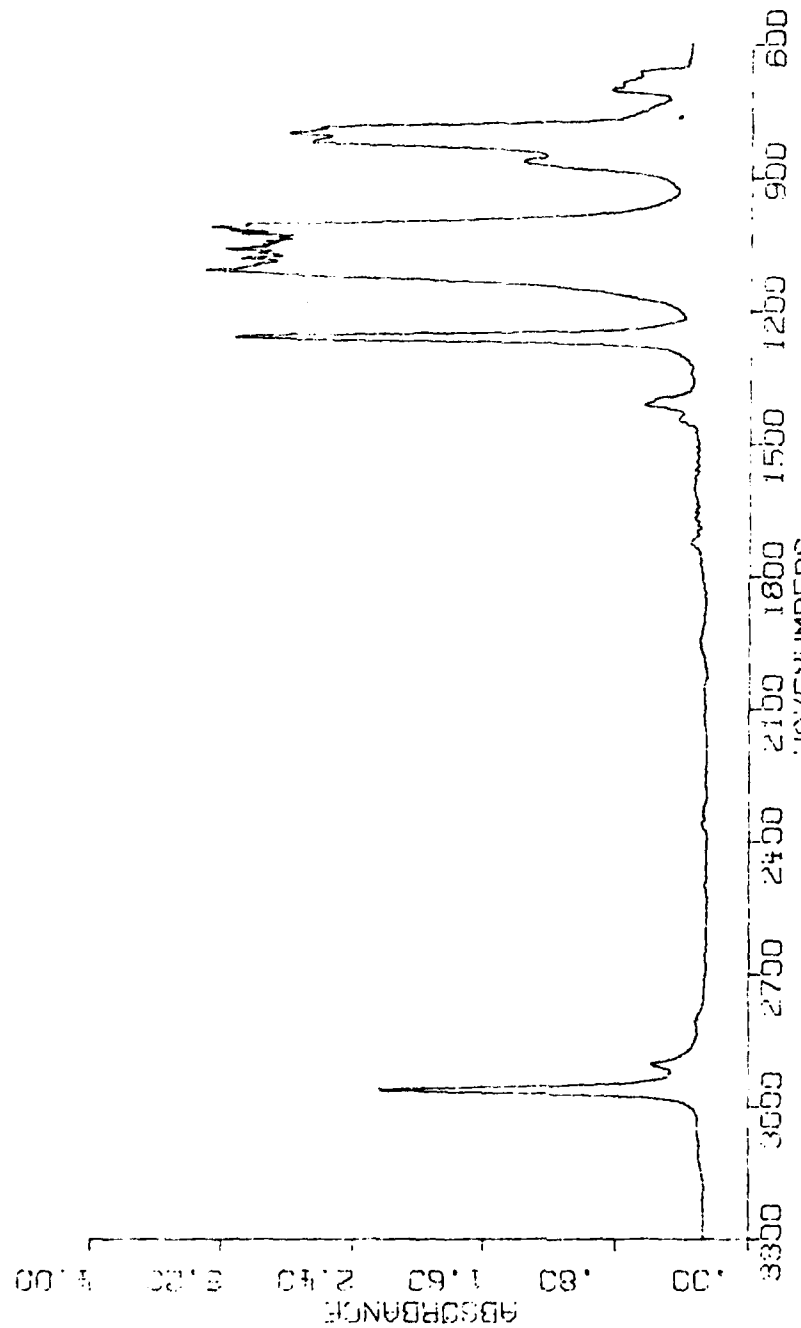

Figure 2.4-18 Absorbance of 23.4µm thick gel of System A Cured for 5 Mins.

increasing volume. If this occurs we may not expect the linearity between absorbance and thickness inherent in Beer's Law for the data. The bands for this analysis are those that are not altered during the crosslinking reaction. The following bands should be unreactive:

Wave number (cm^{-1})	Band Assignment
1022.00	Si-O
1412.93	CH_3 bending
2964.70	C-H vibration

The wave numbers and absorbances were read digitally from the FTIR. The data are listed in Table 2.4-VIII below.

Table 2.4-VIII

Absorbance of 5 minute Cured System A

Sample Thickness (μm)	Absorbance Wavelength (cm^{-1})		
	1022.00	1412.93	2964.70
6.4	1.959	0.280	0.813
12.7	2.716	0.398	1.489
19.1	2.497	0.363	1.622
23.4	3.232	0.637	2.230
36.1	3.256	0.860	2.946
50.8	3.965	0.915	3.021

2.4.6 Summary

IR spectra over the interval from 5000 to 400 cm^{-1} were taken for System A, System B, and the Dielectric Gel. The bands active in crosslinking were identified according to the bond structure of PDMS. This method of characterization is much more convenient than that of swelling for the case of thin films. For long exposure times to U.V., the silicones are altered as is evidenced by the reduced I.R. transmission at the longer wave numbers.

References

1. R. T. Conley, Infrared Spectroscopy, Allyn and Bacon, Inc., Boston, 1966.

2. J. B. Hendrickson, D. J. Cram, G. S. Hammond, Organic Chemistry, 3rd Edition, McGraw Hill (1970), Sec. 7-5.

2.5 Deformation Models

The dynamics of thin structures have been modelled using a compressional displacement. The first model which used an electrostatic field as an external driver was solved for an incompressible isotropic medium such as a silicone elastomer. This model has been extended by the addition of the more correct boundary condition of a vanishing displacement field of the structure at the gel - glass substrate interface. This boundary condition adds a geometrical shape factor into the dynamical equations. Equations including the viscoelastic response of a more general nature are presented in Chapter 3. The equations presented below have been used to calculate an order of magnitude of static deflections.

2.5.1 Electrostatic Deformation

The microstructure can be envisaged as a capacitor with a dielectric of silicone elastomers. A diagram of the structure and the labelling coordinate system to be used is shown in Figure 2.5-0; The elastomer is assumed to be incompressible and isotropic in the unstrained state. The deformation due to the force of gravity can be neglected.

When a potential is applied across the structure, the total energy of the deformed system consists of two terms, the electrostatic energy, E_e, and strain energy, E_s, such that

$$E_{(tot)} = E_e + E_s \qquad (2.5\text{-}1)$$

For a uniaxial compression in the z-direction the net normal stress, F_z, is

$$F_z = \frac{\partial E}{\partial Z} = \frac{\partial E_e}{\partial Z} + \frac{\partial E_s}{\partial Z} \qquad (2.5\text{-}2)$$

AD-A105 707 SYRACUSE UNIV NY DEPT OF ELECTRICAL AND COMPUTER EN--ETC F/G 11/9
POLYMERIC MICROELECTRONICS.(U)
JUN 81 S T KOWEL, E BALIZER, T T SU, I H LOH DAAK70-80-C-0053
UNCLASSIFIED TR-81-6 NL

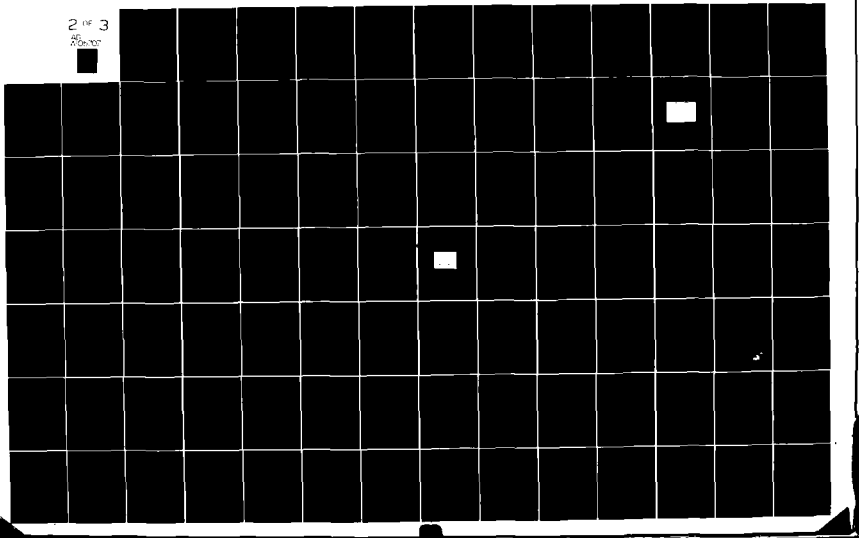

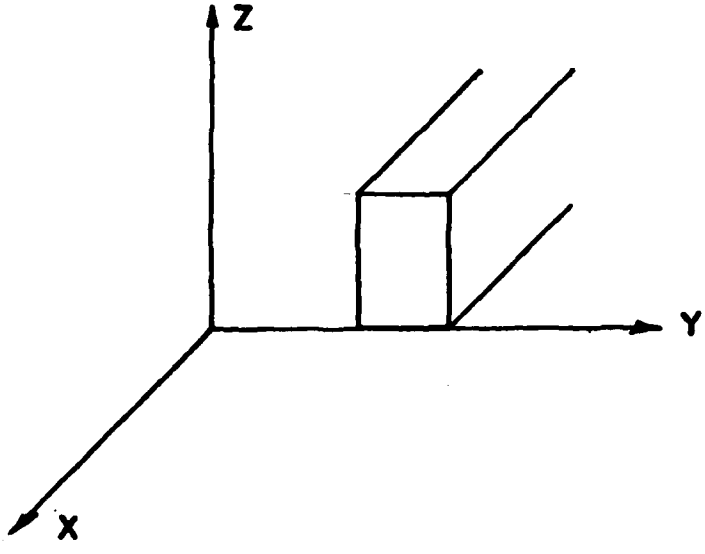

Figure 2.5-0 The Coordinates System for the Deformable Microstructure

where the partial derivatives are evaluated at constant voltage. At equilibrium the net normal stress is zero and the electrostatic attraction is balanced by the mechanical strain

$$\frac{\partial E_e}{\partial Z} = \frac{-\partial E_s}{\partial Z} \qquad (2.5\text{-}3)$$

or $F_e = -F_s$

For a parallel plate capacitor with dielectric materials between the plates, the capacitance is

$$C = \varepsilon\varepsilon_o A/d$$

where ε is the dielectric constant,

ε_o is the permittivity constant,

A is the area,

and d is the thickness of the dielectric,

The stored energy E_e in the capacitor at a static voltage is

$$E_e = \frac{1}{2} Cv^2 = \frac{1}{2} \frac{\varepsilon\varepsilon_o A}{d} V^2 = \frac{1}{2} \varepsilon\varepsilon_o AV^2 \frac{1}{d} \qquad (2.5\text{-}4)$$

Therefore F_e is

$$F_e = \frac{\partial E_e}{\partial d} = -\frac{1}{2} \varepsilon\varepsilon_o AV^2 \frac{1}{d^2} \qquad (2.5\text{-}5)$$

From the statistical theory of rubber elasticity the strain energy per unit volume of a deformed rubber which has a shear modulus G can be expressed as

$$E_s = \frac{1}{2} G(\lambda_1^2 + \lambda_2^2 + \lambda_3^2 - 3) \qquad (2.5\text{-}6)$$

Where λ_1, λ_2, λ_3 are the linear extension ratios in the X, Y, and Z directions respectively. For a incompressible, isotropic uniaxial compression along the Z axis, where d_o is the initial length and d the deformed length,

$$\lambda_1\lambda_2\lambda_3 = 1$$

$$\lambda_1^2 = \lambda_2^2 = \frac{1}{\lambda_3} = \frac{d_o}{d} \qquad (2.5\text{-}7)$$

Thus, using (2.5-6) and (2.5-7) eq. (2.5-2) becomes

$$F_s = \frac{\partial E_s}{\partial \lambda_3} = G\left(\frac{d}{d_o^2} - \frac{d_o}{d^2}\right) d_o \qquad (2.5\text{-}8)$$

At equilibrium,

$$F_e = -F_s$$

Thus, from (2.5-8) and (2.5-5),

$$-\frac{1}{2}\frac{\varepsilon\varepsilon_o A V^2}{d^2} = G\left(\frac{d}{d_o^2} - \frac{d_o}{d^2}\right) d_o \qquad (2.5\text{-}9)$$

For unit volume $Ad_o = 1$, and the deflection for a potential V becomes

$$d = \left(d_o^3 - d_o\, \varepsilon\varepsilon_o V^2/2G\right)^{1/3} \qquad (2.5\text{-}10)$$

Equation 2.5-10 can be used to estimate the deformation of the microstructure or to calculate the elastic modulus of a deformed gel.

It was shown in the theoretical derivation (Equation 2.5-10) that the deformation of microelectronic components is dominated by three factors: the applied voltage , the moduli of the gels, and the microelectronic component geometry (thickness). The linear percentage deformation $((d_o - d)/d_o)$ for microelectronic components under various static voltages has been calculated for two gels with shear moduli of 10^4 Pa and 10^5 Pa. In the analysis, 5 μm, 10 μm, and 20 μm thick samples were considered with an applied voltage between 50 and 400 volts. The results are shown in Figures 2.5-1 and 2.5-2. For a sample with a thickness of 10 μm, 450 volts are required to induce a 10% deformation in a gel with a modulus of 10^4 Pa.

Since the shear modulus G (G = E/3) for System B obtained from the equilibrium swelling study was on the order of 10^4 Pa to 10^5 Pa, the above results are readily applicable to estimate the microcomponent deformations.

2.5.2 Deformation by a Microstructure with One Stationary Electrode

The expression derived for the equilibrium of the structure in Section 2.5.1 did not implicitly contain the boundary condition of a stationary or fixed surface. For the microstructure the bottom electrode is mounted on a rigid glass slide and, therefore, at the interface, the gel cannot undergo a deformation. A theoretical treatment for small compressions including this boundary condition has been derived previously.

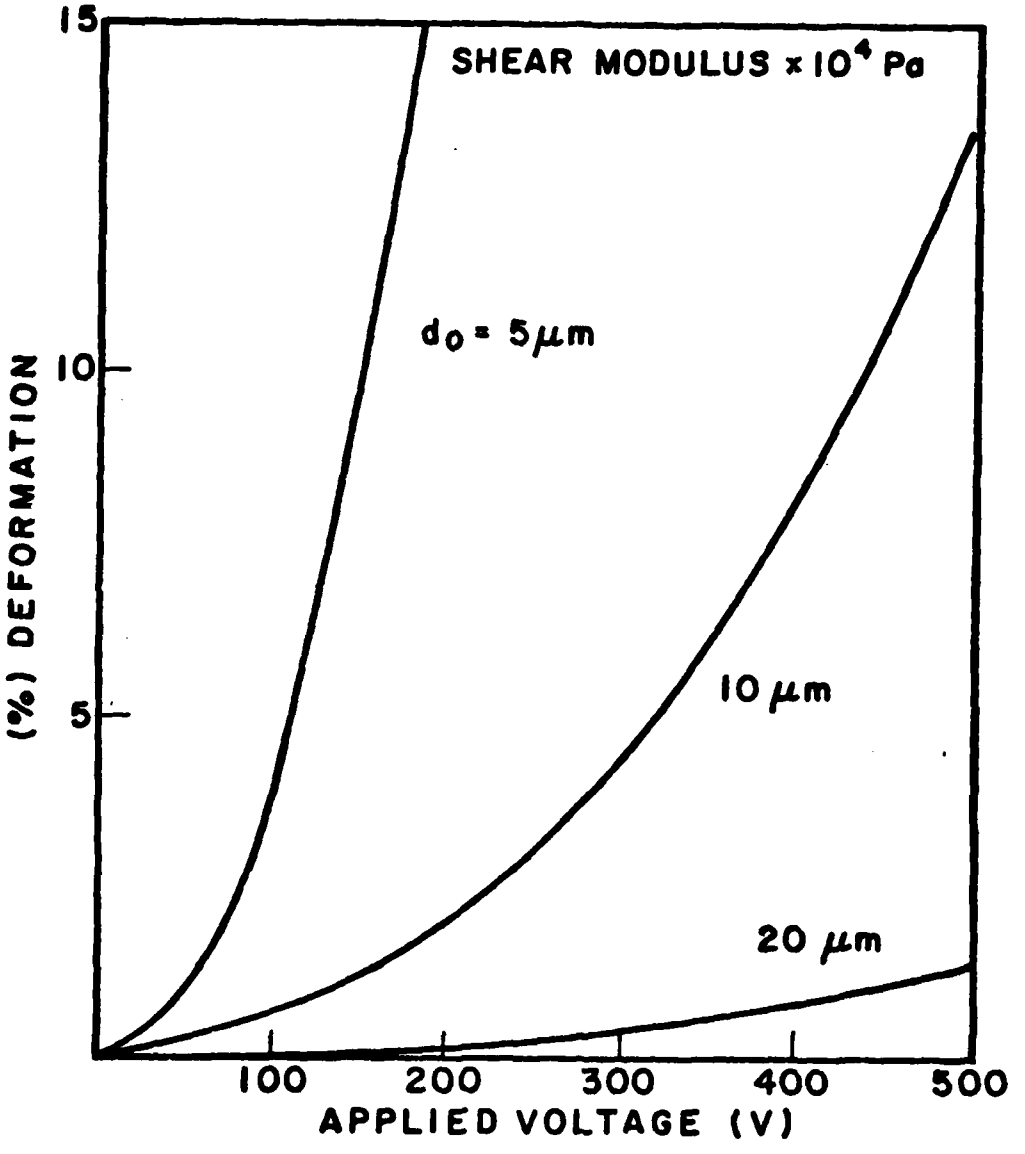

Figure 2.5-1 Component Percentage Deformation Versus Applied Voltage (Shear Modulus x 10^4Pa) From Equation (2.5-10).

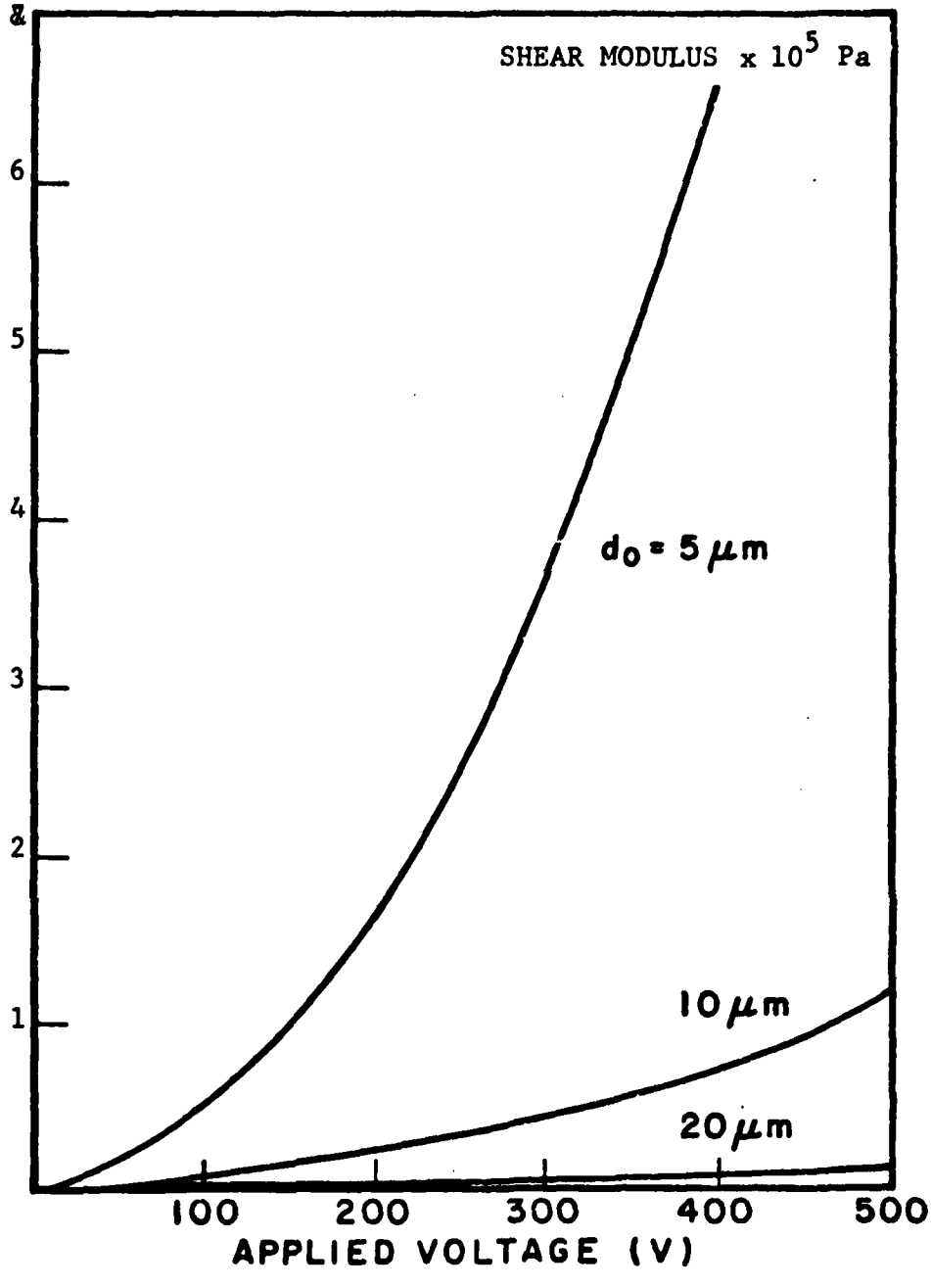

Figure 2.5-2 Component Percentage Deformation Versus Applied Voltage (Shear Modulus x 10^5Pa) From Equation (2.5-10).

The overall deformation is assumed to consist of the superposition of two simple deformations:

(1) Homogeneous compressions, brought about by the same deformation as for free surfaces.

Here, the force F_1 is given as

$$F_1 = KEA\ (d_o - d)\ /d_o \qquad (2.5\text{-}11)$$

where E = Young's modulus

$d_o - d$ = deformation displacement

K = a constant, which is equal to 4/3 for a structure where the length exceeds five times the width.

(2) A second force due to the outward bulging of the initially vertical planes, arising from the requirements that the volume of rubber is conserved and that a stationary deformation exists along one surface. This force is

$$F_2 = (4/3)\ S^2EA(d_o - d)/d_o \qquad (2.5\text{-}12)$$

where S = shape factor, depending on the structure, which is equal to $B/2d_o$, for a long strip structure.

B = the width of the structure.

The total force F_s is given by the sum.

$$F_s = F_1 + F_2$$

$$= 4/3\ EA\ (1 + S^2)(d_o - d)/d_o \qquad (2.5\text{-}13)$$

Using the equilibrium condition,

$$F_s = -F_e \qquad (2.5\text{-}14)$$

and Eq. 2.5-5, we find,

$$(1 + S^2)\ EA\ (d_o - d)/d_o = (3/8)\ \varepsilon\varepsilon_o AV^2/d^2 \qquad (2.5\text{-}15)$$

Figures (2.5-3) and (2.5-5) indicate how the deformation depends on shape factor and electric field. The dependence of the displacement on applied voltage is shown for two values of the modulus, 10^4 Pa and 10^5 Pa. The curves are very dependent on the thickness, d_o, of the structure; increasing the thickness reduces the electrostatic force and, therefore, reduces the deformation whereas decreasing the thickness increases the deformation. This explains the trend on the thickness in the figures. However, increasing the thickness also diminishes the shape factor which hinders the deformation.

When the displacement versus thickness is plotted as in Figure 2.5-5, it is found that there is an optimal thickness which coincides with maximum deformation. This optimal thickness depends on the applied voltage and the elastomer modulus.

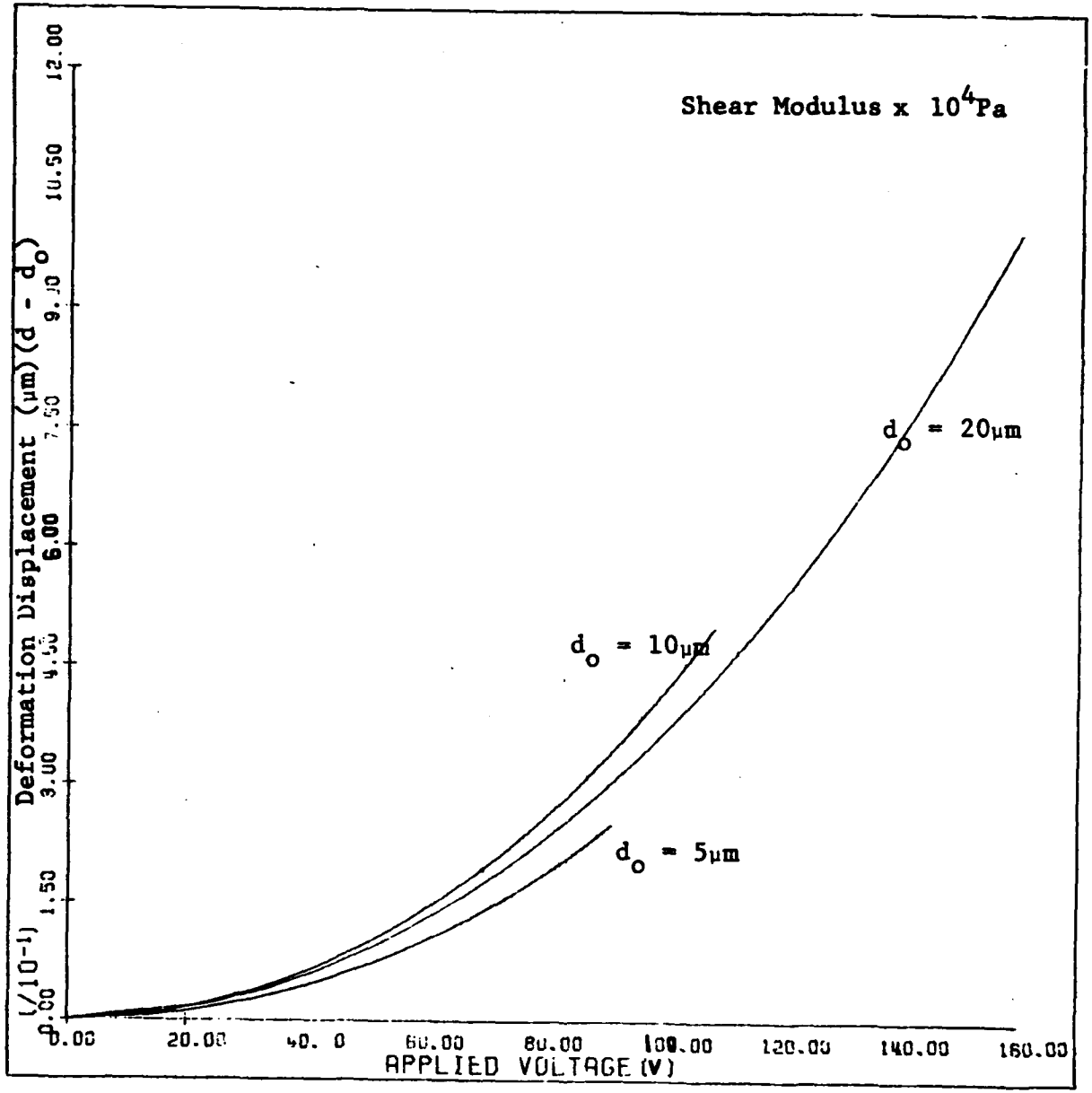

Figure 2.5-3 Component Deformation Versus Applied Voltage (Shear Modulus x 10^4Pa) From Equation (2.5-15).

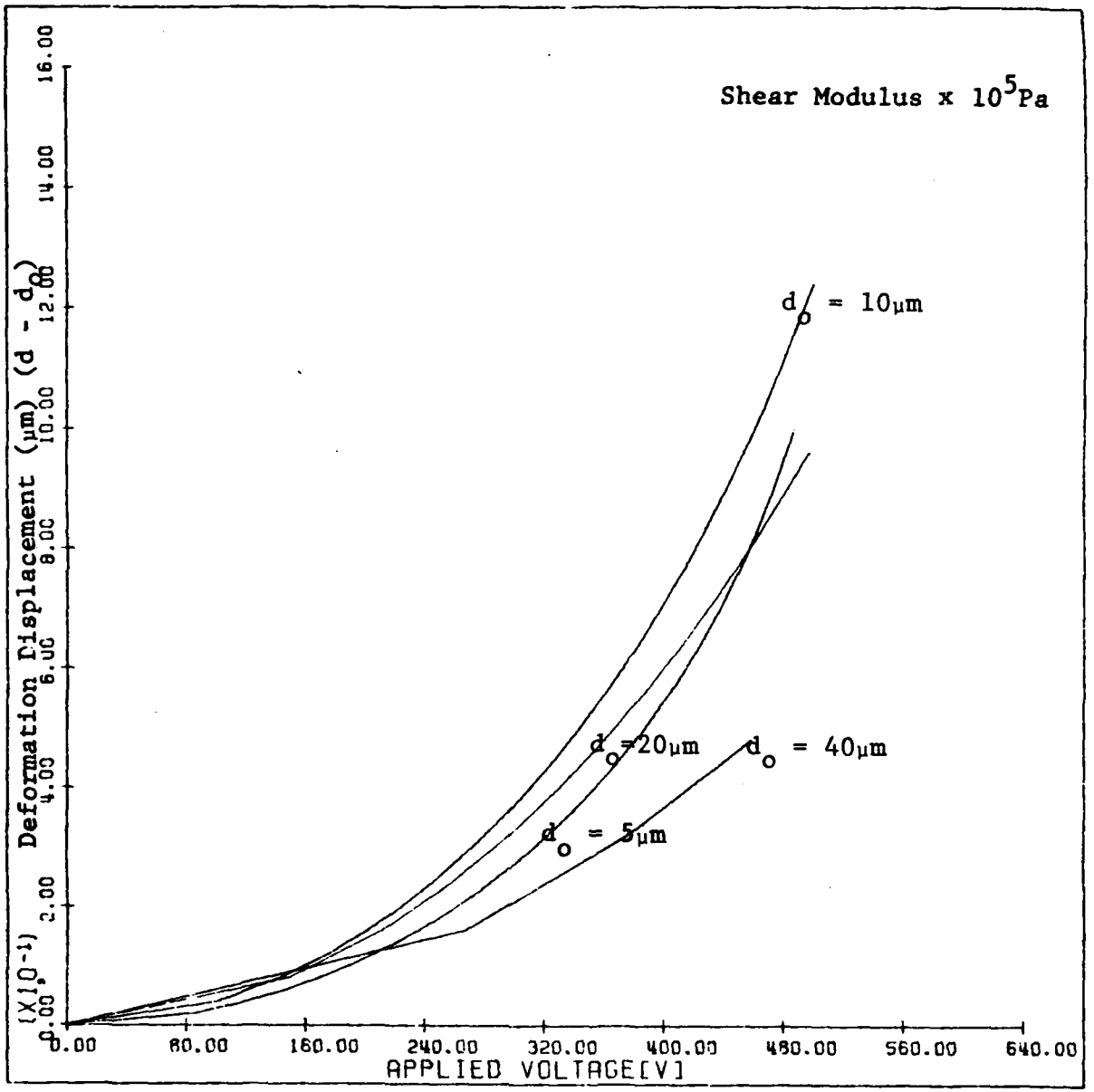

Figure 2.5-4 Component Deformation Versus Applied Voltage (Shear Modulus x 10^5Pa) From Equation (2.5-15).

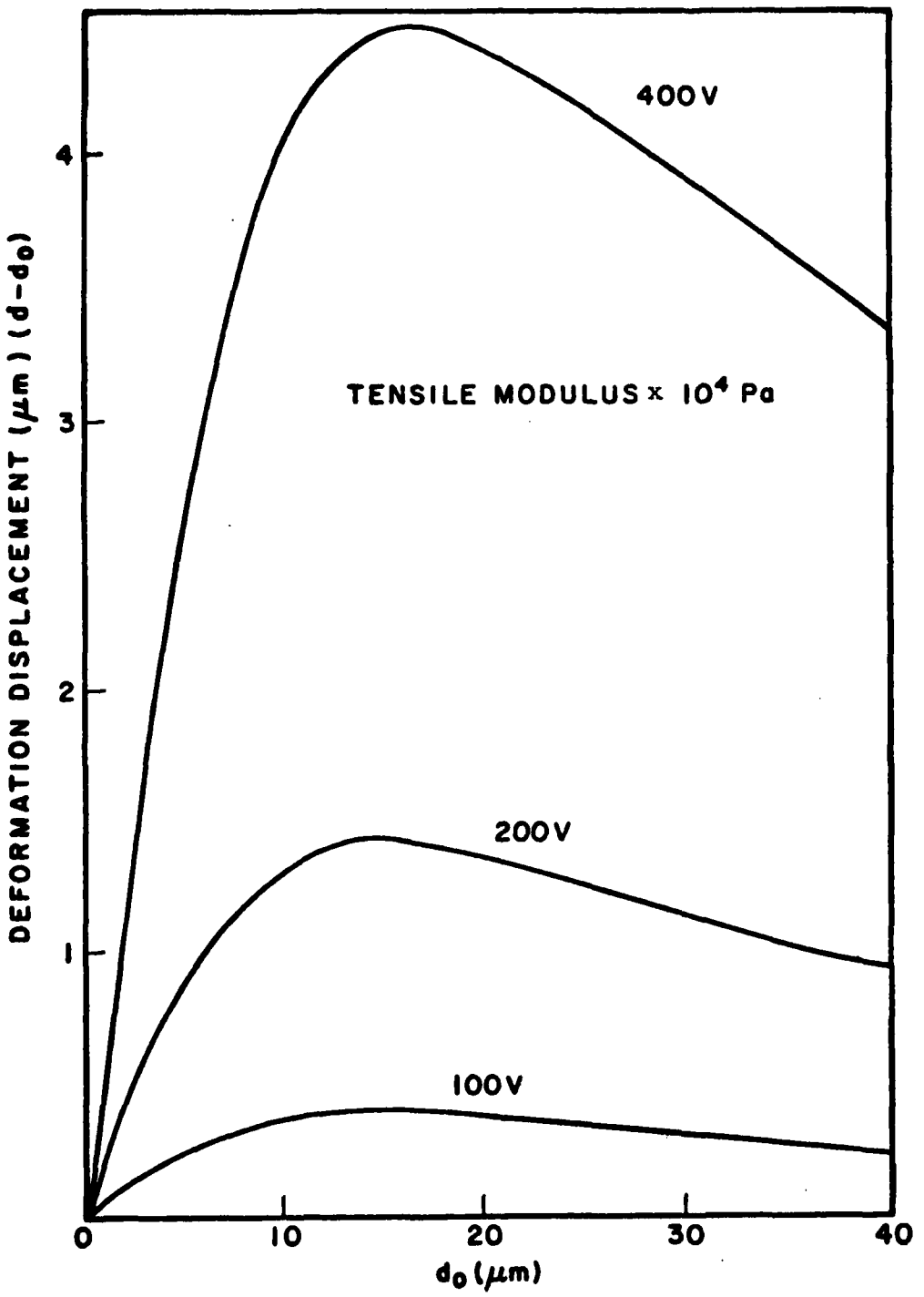

Figure 2.5-5 Deformation Displacement Versus Polymer Thickness (Tensile Modulus x 10^4Pa) at several Voltages

2.6 Experimental Evaluation of Deformation

An optical interference experiment was set up to detect displacements of the gels to a fraction of the wavelength used (HeNe laser source). Problems such as metal breakdown, charge conductance through the gel and metallization conditions of the reflecting surface were investigated.

In order to insure that charge was stored on the aluminum electrodes the I/V curves were measured for devices of several electrode geometries. Our geometry was a metal film for the bottom electrode, the other electrode was a metal finger pattern. None of the changes in the I/V curves, for voltages up to 500 volts indicated breakdown. A problem arose in achieving a specular reflecting surface for the finger electrodes. This led to investigation of the optimum processing conditions of the metal films that would yield good transmission in the U.V. and still be conducting. The results indicated the optimal choice for an aluminum film to be 120 to 140 Å thick.

2.6.1 The Interference Experiment

A schematic of the system is illustrated in Fig. 2.6-1. The laser beam is divided into two optical paths by the beam splitter at B. One path uses the reflected light from B to shine on the sample at C then through B to the screen at E. The other path is transmitted through the splitter, then reflected from a mirror at D and combined with the first beam at E. Care was taken to eliminate vibration so that, when the beams overlapped on the screen (E), an interference fringe pattern could be observed. The de-

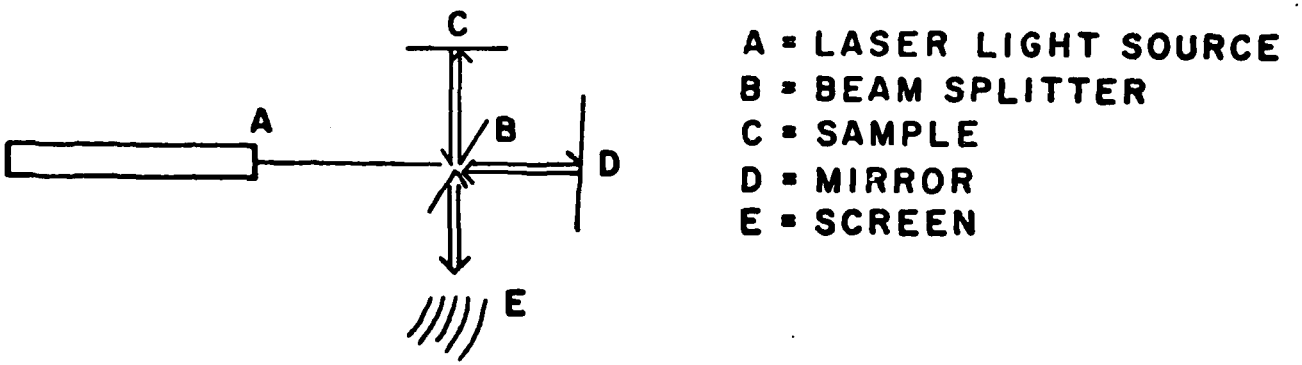

Figure 2.6-1 The Set-up of the Light Interference

formation of the metal surface on the polymer is expected to shift this pattern.

2.6.2 The Deformation Experiment Using Gold Electrodes

It was found that a sharper interference pattern occurs for a gold than an aluminum film. To this end, a structure was made of a glass substrate (0.846 cm thick, dielectric constant of 4.7), was coated with a silicone dielectric gel (800 μm thick, dielectric constant of 2.95), and then a thin gold film of 400 Å was evaporated onto the gel at cryogenic conditions. The pattern of the gold film is shown in Fig. (2.6-2). A positive potential was placed at the T pattern and the metal holder was grounded. A separate island of gold film was used as a reference which did not deform when placed in the laser beam path when a potential was applied to the T. This two-position sampling procedure insured that the shift was caused by the deformation of the gel.

Shifts in the interference pattern were observed for a range of voltages applied between the metal holder and the gold film. The deformation of the gel surface was calculated from the measured shift using Eq. (2.6-1)

$$d = \lambda (\Delta X) / 2h \qquad (2.6\text{-}1)$$

where d is the deformation,

λ is the laser wavelength,

ΔX is the displacement of the fringe,

and h is the width between two constructive interference fringes.

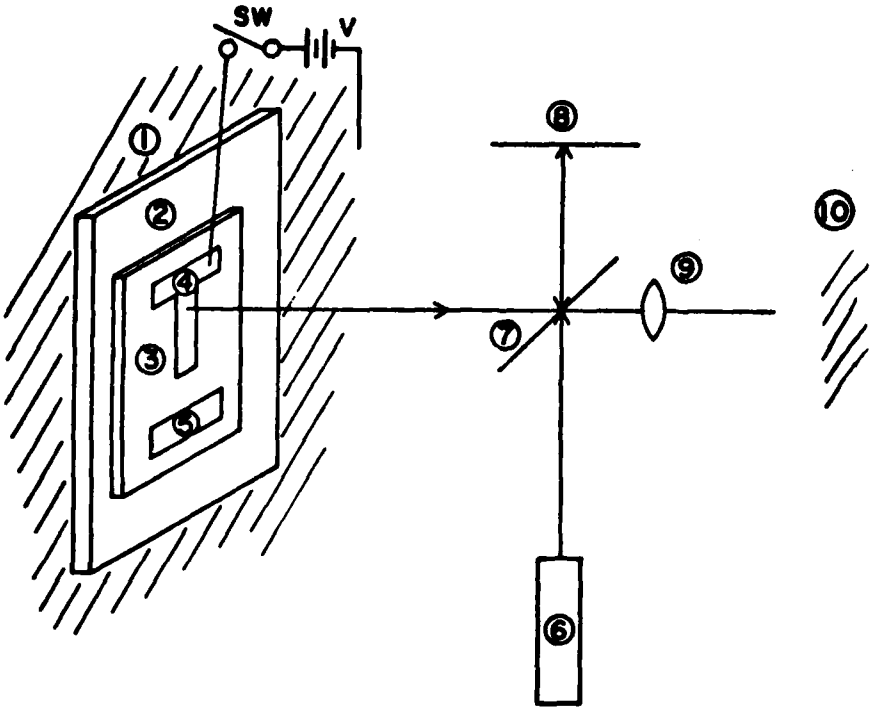

① METAL HOLDER
② GLASS SUBSTRATE
③ SILICONE DIELECTRIC GEL
④ & ⑤ GOLD THIN FILM
⑥ LASER
⑦ BEAM SPLITTER
⑧ MIRROR
⑨ BEAM EXPANDER
⑩ SCREEN

Figure 2.6-2 Schematic of the Experimental Set-up

The values of the deformation for h = 2.4 cm are listed in Table 2.6-I. Since the potential was applied across both the glass and the gel, the correct potential across the gel was calculated using the thickness dimensions and the dielectric constants. The resulting values are listed in the second column of Table 2.6-I. These values were then substituted into Eq. 2.5-15, the theoretical equation for the displacement.

The deformation is plotted for different values of the tensile modulus as shown in Figure 2.6-3. The best fitting value of the modulus is about 3000 Pa. This is a low value as compared to the value expected from the swelling experiments (10^4 Pa.). Experimental errors involving the measurement of the thickness of the gel and the electric field across the gel may account for this discrepancy.

2.6.3 Bulk Current Measurements for Aluminum Electrodes

Two sets of capacitive devices were constructed for the deformation study. One set consisted of an aluminum metal layer on glass, a crosslinked 20 μm layer of silicone (System B) and a layer of indium or aluminum metal evaporated when the substrate was cooled by liquid nitrogen. The second set of capacitors had metal fingers instead of a metal film as the electrode on the glass. The fingers were 20 μm wide with a separation spacing of 8 μm. The surface for these samples was indium. In order for the deformation to occur and be maintained, charge must be stored on the electrodes.

Table 2.6-I - Calculated Displacements

Applied Voltage	Voltage Across the Polymer Gel V	Fringe Displacement Δx (cm)	Deformation by eq.(1) d (Å)
200	120	0.5	658
250	150	0.7	924
300	180	1.1	1455
350	210	1.3	1709
400	240	1.8	2373
450	270	2.4	3164
500	300	2.9	3822

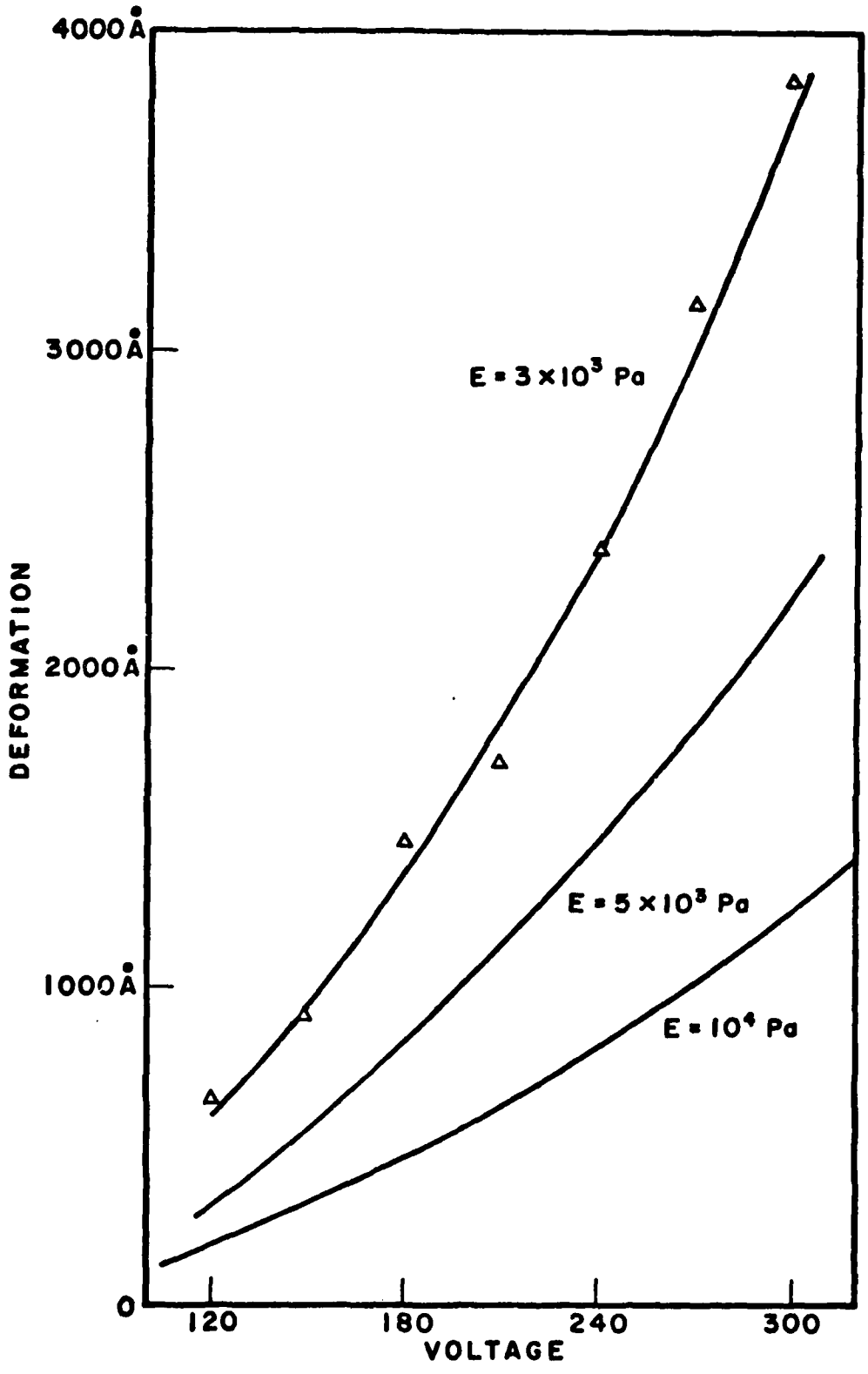

Figure 2.6-3 The Experimental Deformation Curve Compare With the Theoretical Curves.

To investigate the charge storage capacity a voltage supply, a capacitor device, an electrometer and a 100 kΩ safety resistor were connected in series to measure the I/V characteristics of the devices.

If breakdown of the gel occurs, the current versus voltage curve changes slope and the breakdown voltage can be determined where this change occurs. No noticeable current was measured in the tenth of a milliampere range for values of applied voltages between 0 and 500 volts. Since breakdown of the gel did not occur, the 100 kΩ safety resistor was removed and currents on the order of 10^{-9} amps were measured. The positions of the leads were fixed in place since minor positional adjustments may cause differences in readings for the polymer devices for such small currents. The leads at the voltage supply were also alternated so that the I/V curves were taken for both polarities of the electrode. The I/V curve for a capacitor is shown in Fig. 2.6-4. The open circles refer to the bottom electrode on the glass surface being connected to the high voltage, the dark circles for this electrode being grounded. The I/V curves for both polarities appear similar. The range from 0 to about 360 volts appears linear and another linear section of increased slope lies above 360 V. There is no noticeable saturation for either polarity as previously reported for a Ruticon type device.(1) Figs. 2.6-5 and 2.6-6 are the I/V curves for the second set of structures which have metallized fingers for the bottom electrode. The data for such a structure, Fig. 2.6-6, should be read with care as two different vertical scales are used depending upon the polarity

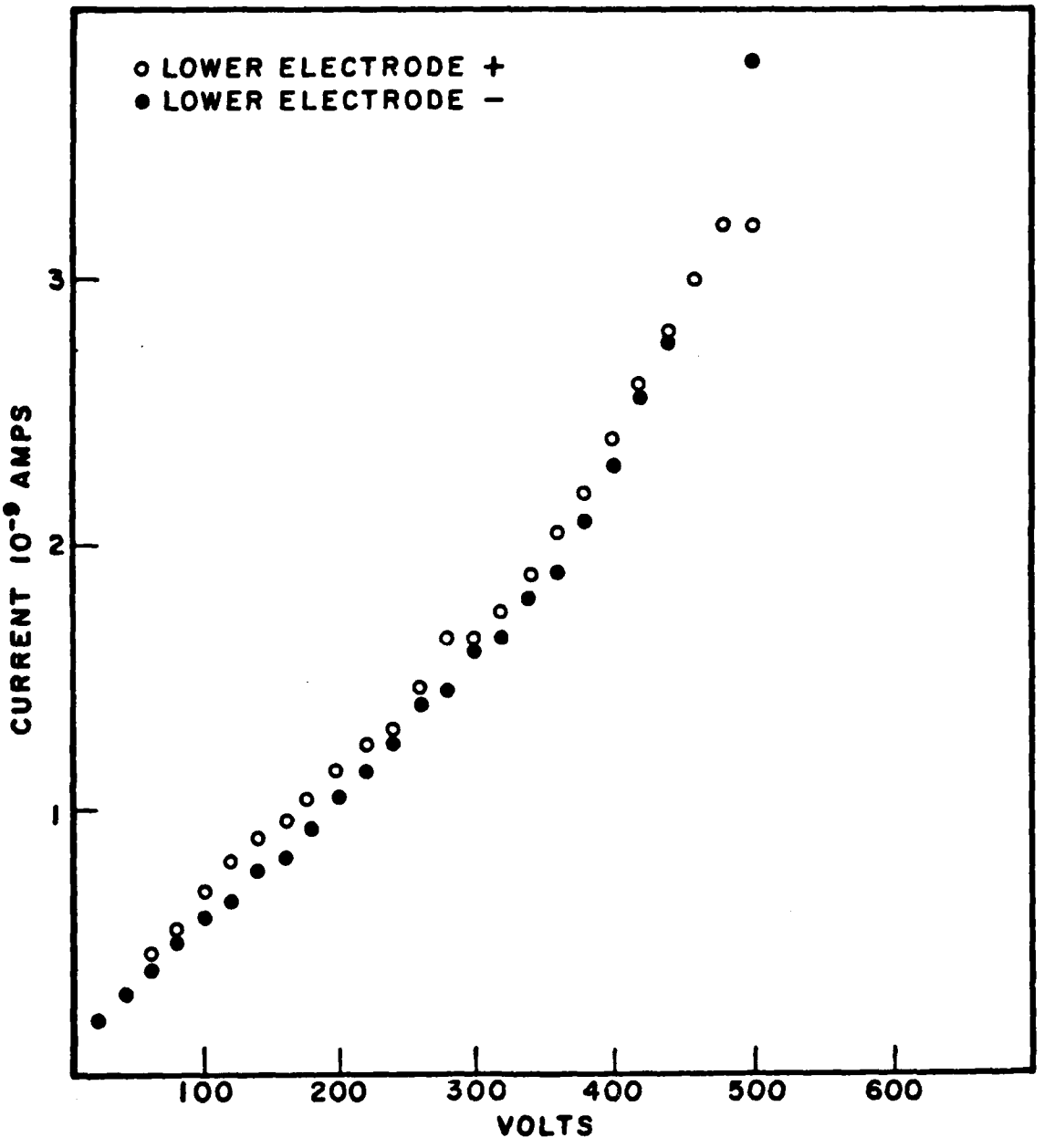

Figure 2.6-4 I/V Curve for an Electroded System B Gel

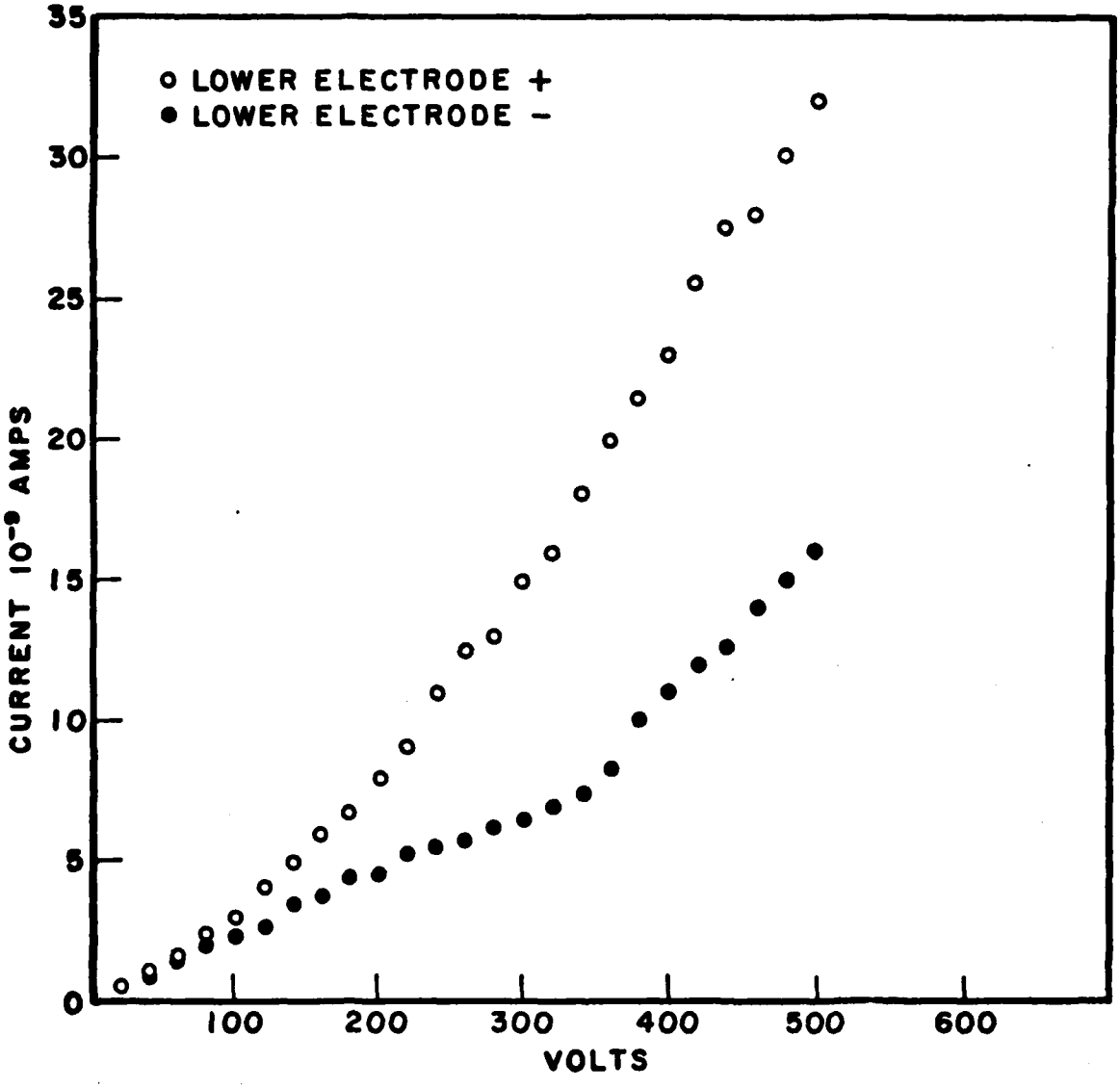

Figure 2.6-5 I/V Curve for an Aluminum Interdigital Electrode on System B

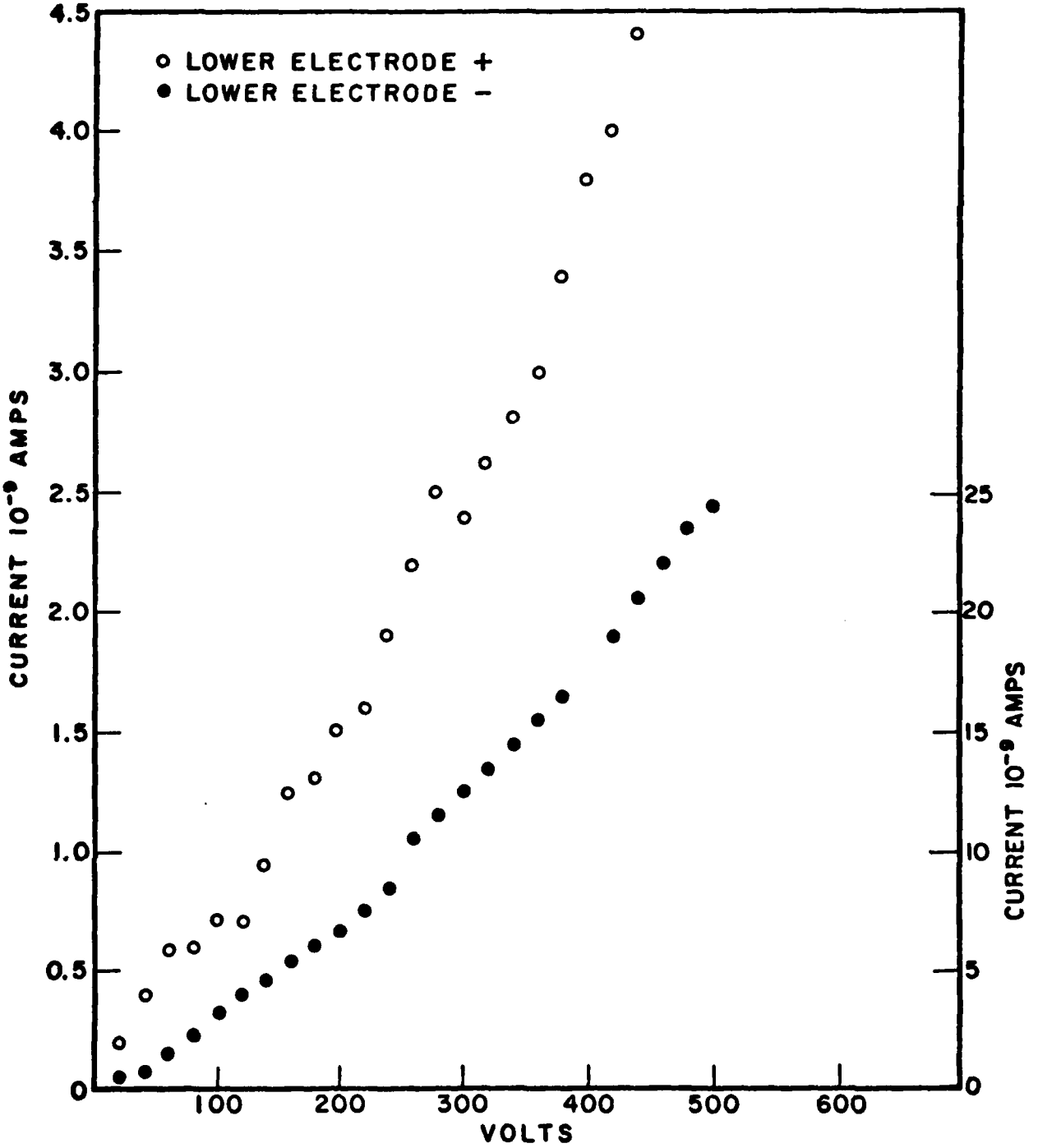

Figure 2.6-6 I/V Curve for an Indium Interdigital Electrode.on System B. The Vertical Scale on the Left is for the Bottom Electrode at a Positive Potential; that on the right is for the Bottom Electrode at a Negative Potential.

of the voltage applied to the fingers. In both cases, when the bottom electrode fingers were at a negative voltage, the current was largest. The I/V curve for a negative polarity of the fingers also appears to have some curvature. For positive polarity of the fingers, the I/V curve has a break in slope at 360 V, with a sharper slope above this value. It was expected that, since the top electrode has a greater area in contact with the polymer than the fingers, a larger injected current would result upon application of a negative bias to this surface. However, the method of deposition of this metal layer is different than that of the fingers. The effect on the charge injection is expected to be different for these two metallization processes. There was no evidence for a breakdown or transport of a large quantity of charge for either sample.

2.6.4 Surface Metallization Studies

We noticed that the surface metallization of the capacitive devices with finger electrodes on the glass substrate was not as smooth as that on just the glass substrate. Light could not be specularly reflected thus causing difficulty in forming an interference pattern to observe the deformation. The reflecting metal surface on the gel over the fingers was studied by microscopy; the coarseness of the surface can readily be seen in Fig. 2.6-7.

The coarseness of the metal surface was thought to be caused by insufficient or non-homogeneous crosslinking thus

Figure 2.6-7 Picture of Coarse Metallized Surface on Gel Over Al Fingers.

creating a polymer structure with surface variation. For the formation of the microstructure element, U.V. light must pass through a thin metal film and then enter the polymer for curing. This film must also be conductive to act as an electrode. The deposition process was investigated to optimize the thickness of the metal film.

A major characterization parameter of the film is its thickness, d, which can be estimated from equation 2.6-2 (2) below:

$$d = \frac{M_e}{\pi\rho h^2(1 + (\ell/h)^2)^2} \qquad (2.6\text{-}2)$$

where M_e = the evaporated mass (gms),

ρ = the density of the film material,

h = the distance between the substrate and the evaporated source,

ℓ = the distance from the center of the substrate

For $h >> \ell$ and an M_e of 3mg. of aluminum wire a 6nm metal film layer results.

Previous conductance measurements of films of similar thicknesses indicate conductance properties that are not reproducible. The characteristics of the metallization of the glass substrate is not only controlled by the thickness but also by the kinetics of film growth. Therefore, the conductance is also dependent upon the evaporation rate and the substrate temperature. An experimental investigation was conducted on the effect of evaporation rate on the U.V. transmission and conductances of the films in order to optimize their effectiveness.

2.6.5 Experimental Details for Characterizing Thin Metal Films

Thin films of high purity aluminum were prepared by thermal evaporation from a tungsten boat in a high vacuum system at 10^{-5} torr. The films were deposited onto glass slides at room temperature. The rates of deposition were between 0.5 and 5.0nm/sec. The film thickness was measured by a quartz - crystal thickness monitor. The resistivities of these films were measured by a four point probe. The U.V. transmission was measured by a U.V. visible spectrophotometer.

The resistivity of thin films as found by the four point probe method was calculated from equation (2.6-3) (3)

$$\rho/d = R_s = 4.532\ V/I \qquad (2.6-3)$$

where ρ = resistivity

d = the thickness of the thin film

R_s = sheet resistance

V = voltage

I = current

The calculated resistivities for 17 samples are listed in Table 2.6-II. For some of the samples, a variation in resistivity values for the metal surface were measured and for these cases the term "Random" was assigned. The values in Table 2.6-II are also plotted as resistivity vs. thickness in Fig . 2.6-8. Table 2.6-II shows that at about 8nm the films start to conduct, but not reproducibly over the entire surface.

Sample No.	Thickness (A)	Evaporation Rate	Resistivity ($\mu\Omega$-cm)	Comment
1	46	5 - 15 Å/sec		1. The "Random" means there are different resistivities at the different points of the sample.
2	55	5 - 15 Å/sec	Random	
3	59	30 - 40 Å/sec	7.75	
4	66	5 - 10 Å/sec	Random	
5	88	5 - 10 Å/sec	Random	2. Evaporation Rate is read from thickness and rate monitor.
6	109	1 - 5 Å/sec	32.3	
7	113	10 - 20 Å/sec	1.54	
8	129	20 - 30 Å/sec	2.02	
9	138	10 - 15 Å/sec	1.98	
10	149	10 - 15 Å/sec	1.96	
11	161	10 - 15 Å/sec	1.13	
12	165	5 - 10 Å/sec	22.5	
13	165	10 - 15 Å/sec	3.17	
14	181	10 - 15 Å/sec	2.35	
15	212	10 - 15 Å/sec	1.13	
16	215	10 - 15 Å/sec	0.808	
17	328	10 - 15 Å/sec	0.838	

Table 2.6-II

Resistivity vs. Thickness for Gold Films

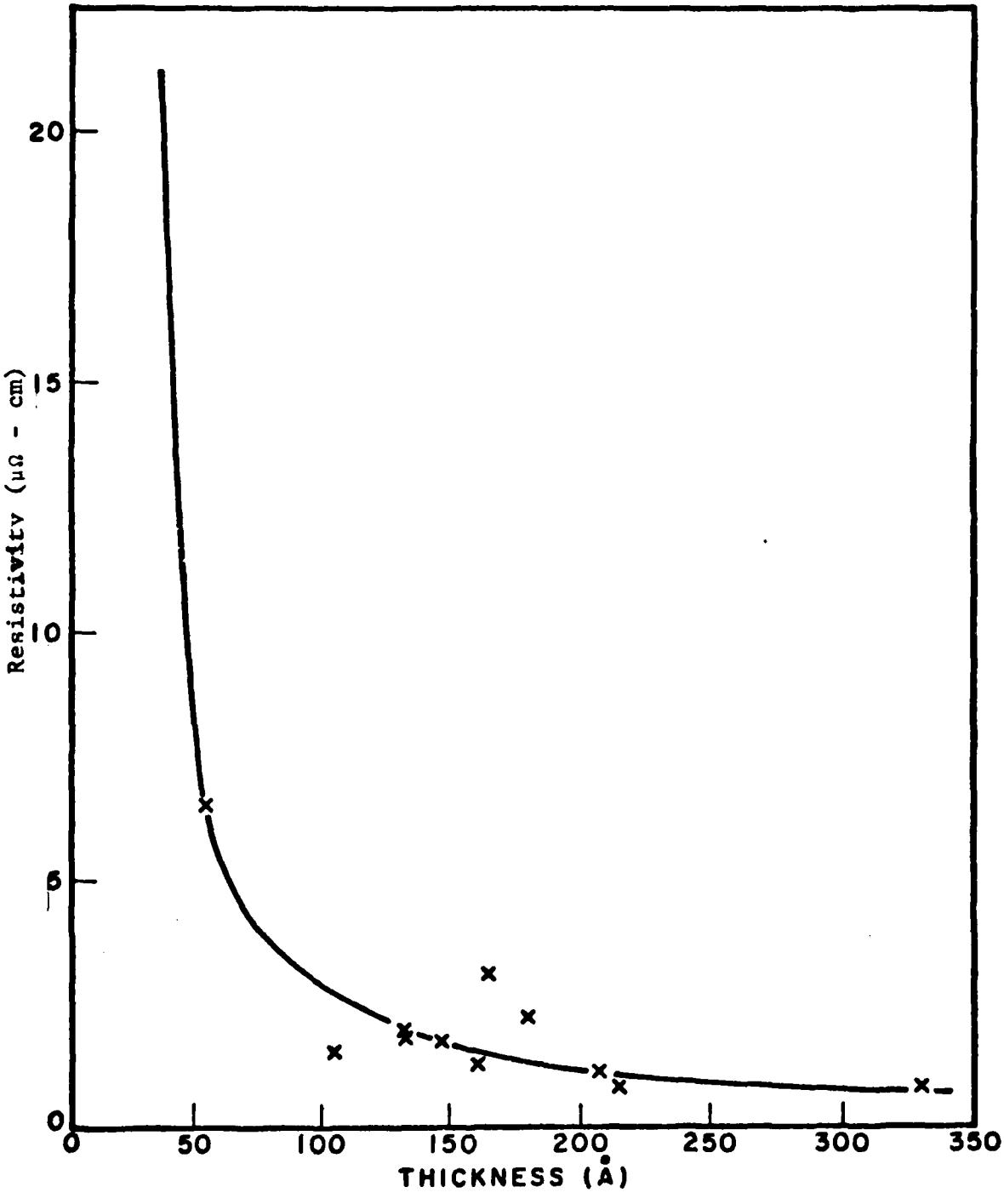

Figure 2.6-8 Resistivity vs. Thickness for Gold Films.

The effect of evaporation rate on the resistivity was found by comparing the values for samples 11, 12, and 13. The film thicknesses are comparable for these samples; however, the resistivity of these films is inversely proportional to the evaporation rate. This result is in agreement with thin film theory in that low substrate temperatures and high deposition rates enhance the formation of a continuous thin film.

The U.V. transmission vs. metal thickness appears in Fig. 2.6-9. The cutoff at 320 nm is due to the properties of the glass; this restricts the usable portion of the U.V. spectra to between 300 to 400 nm for curing the polymer. The U.V. spectra of the polymer was measured to determine if this range overlaps the absorption peaks of the reactive groups for crosslinking. If the frequencies transmitted by the glass are causing the photchemistry, an optimal choice of an aluminum metal thickness is 120 to 140 nm deposited at a fast rate. The resistivity is fairly low, 1.0 - 2.0 $\mu\Omega$-cm, and the U.V. transmittance is about 50%. These values may be improved by substitution of another type of galss that transmits over a broader U.V. range as well as choosing a common metal (Au, Ag, or Cu) that has a higher transmission. Presently, the above investigations are being extended by employing a special Nesa glass from Corning Glass and a gold metal film for the surface reflecting electrode.

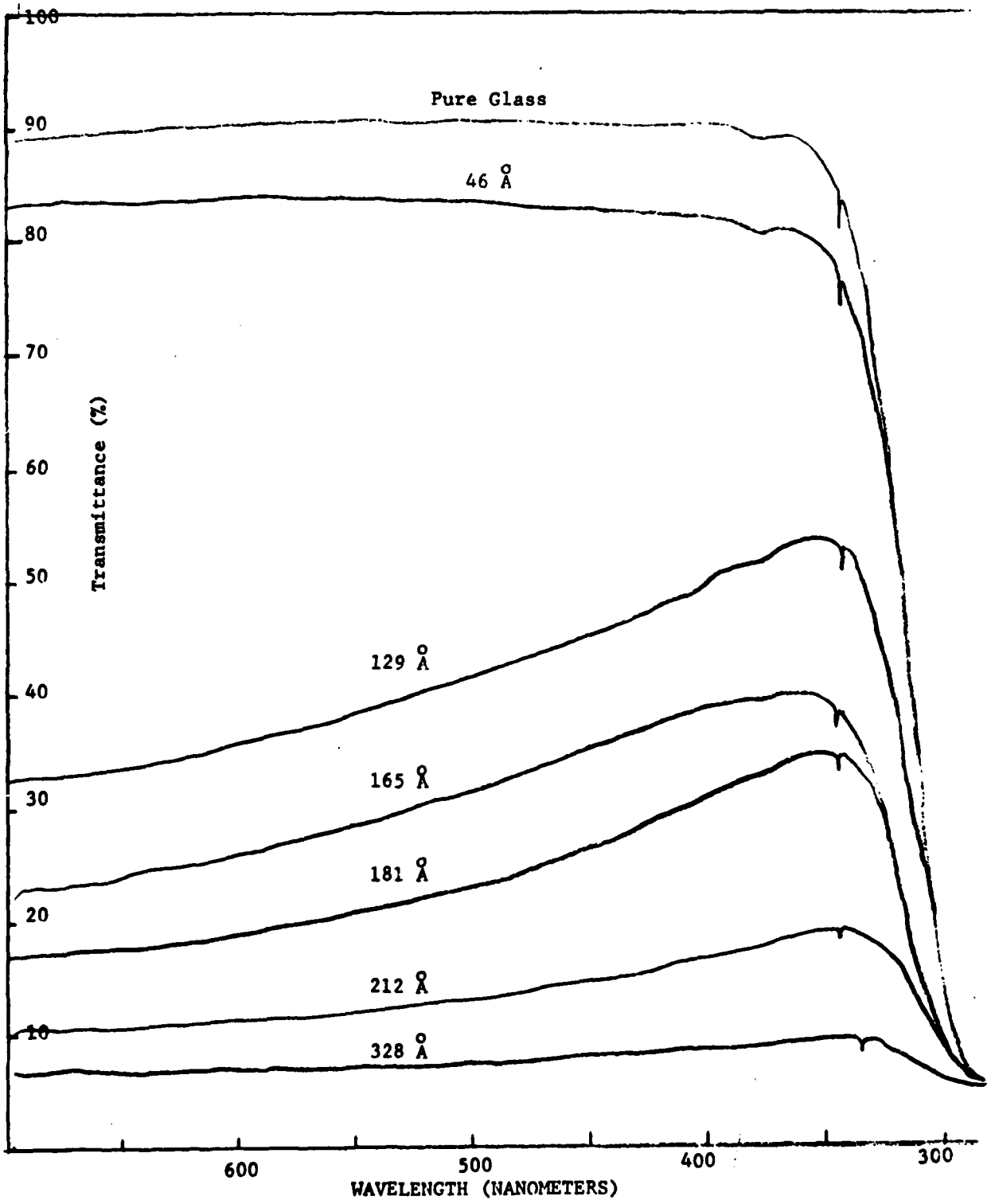

Figure 2.6-9 Light Transmittance Versus Wavelength at Different Aluminum Film Thickness.

References

1. J. J, Wysocki, "Electrical Evaluation of Elastomer-Based Capacitors," OMDA Letter Report 76-8, Xerox WRC, 24 June 1976.

2. Handbook of Thin Film Technology, Edited by L. I. Maissel and R. Glang, p. 56, McGraw Hill, New York, 1970.

3. L. B. Valdes, Proc. IRE, 42, 420, (1954).

Chapter 3: Microstructure Dynamics

3.0 Introduction

The dynamics of the microstructures depend on both the elastic and viscous properties of the silicone polymers. Thus, equilibrium compression does not occur instantaneously, but depends upon the frequency of deformation. Similarly the rise time, that time interval which the structure takes to reset itself to the initial isotropic state, does not occur instantaneously but is dependent on the viscous parameters. At kilohertz frequencies the viscous relaxation corresponds to localized bond rotations of the polymers, for lower frequencies in the Hertz region,the motion corresponds to whole chain motion such as chain slippage. These relaxations are also dependent on the orientation of the molecules in the gels as well as on any crystallinity present. The above mentioned effects occur for the bulk of a structure and are intrinsic properties of the material. However, for thin films and structures, additional complexity of the relaxations occur due to boundary conditions. The boundary conditions confer relations on the stresses and strains that couple the elastic and viscous loss constants and may also involve the geometry of the sample. Thus, the relaxation times for modes satisfying boundary conditions will be a function of both the loss and elastic constants. These functions for plate modes have been found in the regions of low frequency and long wave lengths and are presented in this section.

For an isotropic material, such as silicone, there are four independent elastic and viscous constants. The plate mode relations coupling these constants may be used to determine

each of the four constants. Once these fundamental constants are known the relaxation times of any geometrical microstructure with imposed boundary conditions may be found.

To illustrate the use of the plate mode relations in determining elastic constants, the elastic hysteresis constants for anisotropic PVF_2 were evaluated.

In general oriented polymers films are anisotropic and the relations between the elastic and loss constants are found experimentally from acoustic velocities and losses. The dispersion relations for the losses and velocities are mathematically complex for an anisotropic plate. However, by an approximation technique developed by Mindlin (1), the dispersion relations for the low frequency modes may be directly obtained. This procedure was extended to viscoelastic materials and the equations of motion for the displacement fields were obtained. The calculation and resulting solutions of these equations are presented in Appendix 3A. In the following section, the solutions of the displacement fields and the effects of the boundary on the coupling of these fields are illustrated.

3.1 Description of Plate Acoustic Waves

In an infinite isotropic medium three elastic modes of propagation exist, which are independent of each other. At the free boundary of a plate certain of these modes are coupled. The solutions are separated into four classes according to the directions and symmetry of their displacements. The first two classes are shear waves, i.e., one-dimensional displacements of layers of the thickness parallel to the face of the plate. The two shear classes depend on whether the symmetry of the displacement is odd or even about a midplane through the thickness. The lowest frequency symmetric shear wave is illustrated in Fig. 3.1-1, along with the lowest frequency waves of

Plate Modes

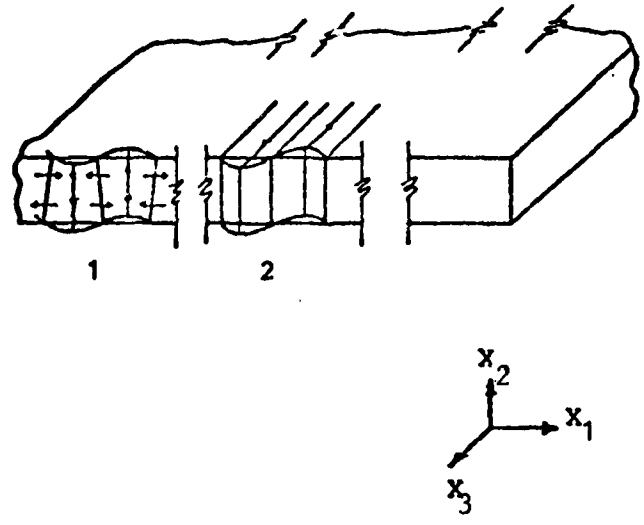

Figure 3.1-1

The three lowest frequency plate modes at long wavelengths: 1 Flexure, 2 Face-Shear, 3 Extension. (after Y. H. Pao and R. K. Kaul, ref. 4)

the two classes to be discussed. The remaining two classes of solutions have coupled displacements in the thickness and the propagation directions. The lowest frequency wave of the antisymmetric class is the extensional which consists of antisymmetric displacements in the thickness direction and a symmetric longitudinal displacement. The corresponding lowest frequency symmetric mode is the flexural wave whose displacements are symmetric in the thickness direction and antisymmetric in the longitudinal direction. These modes occur in the region of low frequency and long wavelength and are of experimental interest in characterizing thin films as to their elastic and loss constants.

3.1.1. Tensor Modulation

Due to the large acoustic losses in polymers we have added to the elastic constituitive equations which yield the above three (low frequency) modes a loss term which represents a viscous or a hysteretic loss. The dispersion relations derived for the above three modes are in terms of the components of the tensors of elastic coefficients as well as those of the viscous or hysteretic loss tensor . As a general example, consider the coefficients compatible with the symmetry of a biaxially oriented polymer film of thickness b.

The coordinates are choosen such that X_1 and X_3 are in the plane of the film and X_2 is normal to the plane. For this film, the orientations of the amorphous and crystalline regions may not align along the draw direction, thus a triclinic symmetry for the elastic constants is assumed. The components of the elastic tensor conforming to this symmetry are

$$C_{ij} = \begin{bmatrix} C_{11} & C_{12} & C_{13} & C_{14} & C_{15} & C_{16} \\ C_{12} & C_{22} & C_{23} & C_{24} & C_{25} & C_{26} \\ C_{13} & C_{23} & C_{33} & C_{34} & C_{35} & C_{36} \\ C_{14} & C_{24} & C_{34} & C_{44} & C_{45} & C_{46} \\ C_{15} & C_{25} & C_{35} & C_{45} & C_{55} & C_{56} \\ C_{16} & C_{26} & C_{36} & C_{46} & C_{56} & C_{66} \end{bmatrix} \qquad (3.1\text{-}1)$$

Subclasses of this matrix that will be useful are those of 2mm symmetry for PVF_2 (13 constants) of isotropic symmetry for a polymer gel (2 constants). It is assumed that the con-

stituitive constants of a viscous or a hysteretic loss will conform to the same symmetry as the elastic constants. The constituitive equations for the two loss mechanisms are:

$$t_{ij} = C_{ijkl}S_{kl} + \eta_{ijkl}\dot{S}_{kl} \qquad (3.1\text{-}2)$$

for the viscous loss, where t_{ij} is the stress, and S_{kl} and $\dot{S}_{kl}$ are the strain and its time derivative;

$$t_{ij} = C_{ijkl}S_{kl} + Jh_{ijkl}S_{kl} \qquad (3.1\text{-}3)$$

for the hysteretic loss where J is $\sqrt{-1}$. The (C),(η), and (h) are arrays of the elastic, viscous and hysteresis constants respectively. By assuming the boundary conditions of the vanishing of the surface tractions on the plate surfaces and that the plate is infinite in extent in the X_3 direction, the wave equations for the flexural and extensional modes were derived and appear in Appendix 3D. These equations for triclinic symmetry for extensional displacements u_1 along X_1 and u_3 along the X_3 direction are

$$\ddot{\rho u}_1 = c'''_{11} u_{1,11} + c'''_{15} u_{3,11} + \eta'''_{11} u_{1,11}$$
$$+ \eta'''_{15} u_{3,11} - \frac{b^2}{3} \frac{c'_{14}}{c'_{44}} \left[1 - \frac{c''_{16}}{c''_{66}}\right] \left[c'''_{51} u_{2,111} + \eta'''_{51} u_{2,111}\right]$$
$$- \frac{b^2}{3} \frac{c''_{16}}{c''_{66}} \left(c'''_{11} u_{2,1111} + \eta'''_{11} u_{2,1111}\right) \tag{3.1-4}$$

$$\ddot{\rho u}_2 = c'''_{51} u_{1,11} + c'''_{55} u_{3,11} + \eta'''_{51} u_{1,11} + \eta'''_{55} u_{3,11}$$
$$- \frac{b^2}{3} \frac{c'_{54}}{c'_{44}} \left[1 - \frac{c''_{56}}{c''_{66}}\right] \left[c'''_{51} u_{2,111} + \eta'''_{51} u_{2,111}\right]$$
$$- \frac{b^2}{3} \frac{c''_{56}}{c''_{66}} \left[c'''_{11} u_{2,1111} + \eta'''_{11} u_{2,1111}\right] \tag{3.1-5}$$

For the flexure mode the wave equation is

$$\ddot{\rho u}_3 = -\frac{b^2}{3} \left[c'''_{11} u_{2,1111} + \eta'''_{11} u_{2,1111}\right] \tag{3.1-6}$$

The constants used in the above equations are defined as follows:

$$c'_{pq} = c_{pq} - \frac{c_{p2} c_{2q}}{c_{22}} \qquad \eta'_{pq} = \eta_{pq} - \frac{c_{p2} \eta_{2q}}{c_{22}}$$

$$c''_{pq} = c'_{pq} - \frac{c'_{p4} c'_{4q}}{c'_{44}} \qquad \eta''_{pq} = \eta'_{pq} - \frac{c'_{p4} \eta'_{4q}}{c'_{44}}$$

$$c'''_{pq} = c''_{pq} - \frac{c''_{p6} c''_{6q}}{c''_{66}} \qquad \eta'''_{pq} = \eta''_{pq} - \frac{c''_{p6} \eta''_{6q}}{c''_{66}}$$

For triclinic symmetry the extensional displacements are coupled to all three displacements. However, a decoupling occurs for the 2mm symmetry of a biaxially oriented polymer. The elastic constants for this symmetry are given by

$$[c_{ij}] = \begin{vmatrix} c_{11} & c_{12} & c_{13} & 0 & 0 & 0 \\ c_{12} & c_{22} & c_{23} & 0 & 0 & 0 \\ c_{13} & c_{23} & c_{33} & 0 & 0 & 0 \\ 0 & 0 & 0 & c_{44} & 0 & 0 \\ 0 & 0 & 0 & 0 & c_{55} & 0 \\ 0 & 0 & 0 & 0 & 0 & c_{66} \end{vmatrix} \tag{3.1-8}$$

The wave equations for this symmetry decouple and become for extensional displacements

$$\rho\ddot{u}_1 = c'_{11}u_{1,11} + \eta'_{11}\dot{u}_{1,11}$$

$$\rho\ddot{u}_3 = c_{55}u_{3,11} + \eta_{55}\dot{u}_{3,11}$$

and (3.1-9)

$$\rho\ddot{u}_2 = -\frac{b^2}{3}\left(c'_{11}u_{2,1111} + \eta'_{11}\dot{u}_{2,1111}\right)$$

for the flexural equation.

When the function for a wave of decaying amplitude is substituted into the equation of motion for the extensional modes, the real and imaginary components of the wave vector are given as, for u_1,

$$k^2 = \omega^2[1 + (1+\omega^2\eta_{11}'^2/c_{11}'^2)^{1/2}] / 2c_{11}(1+\omega^2\eta_{11}'^2/c_{11}'^2)$$

$$\alpha^2 = \omega^2[-1 + (1+\omega^2\eta_{11}'^2/c_{11}'^2)^{1/2}]/2c_{11}'(1+\omega^2\eta_{11}'^2/c_{11}'^2) \quad (3.1\text{-}10)$$

which reduces for small η_{11}'/C_{11}' to

$$\alpha^2 = \rho/4 \frac{\eta_{11}'^2}{c_{11}'^2} \omega^4$$

The characteristic dependence for a viscous loss of α on ω^2 is demonstrated in the above equation. The results for the flexure mode are presented in Appendix 3A and will not be discussed in this section. The dispersion relations for a viscous loss can be converted to that of a hysteretic loss by the substitution of the hysteretic coefficient h_{11}' for $\eta_{11}'\omega$. This results in an attenuation coefficient which is linearly dependent on ω and is observed for semicrystalline polymers. The extensive calculations for the hysteretic loss are shown in the Appendix.

Further reduction occurs for the evaluation of the constants for an isotropic medium such as a silicone gel. Here, there are two independent elastic constants C_{11} and C_{12} and two viscous constants. The coefficients for the extensional wave equations in terms of these constants are

$$C_{11}' = C_{11} - \frac{C_{12}^2}{C_{11}}$$

$$\eta_{11}' = \eta_{11} - \frac{C_{12}\eta_{21}}{C_{11}}$$

for the displacement u_1.

and $$C_{55} = C_{44} = \frac{C_{11} - C_{12}}{2}$$

$$\eta_{55} = \eta_{44} = \frac{\eta_{11} - \eta_{12}}{2}$$

for the displacement u_3. The four viscoelastic constants C_{11}, C_{12}, η_{11}, and η_{12} can be completely determined experimentally from the velocities of shear and extensional modes and their respective attenuations. Experimental results to illustrate the use of these equations for the 2mm symmetry of PVF_2 are presented in the next section.

3.2 Experimental Measurements

The measurements were made with delay apparatus following that of Horvat.[2] It consisted of two blocks, one adjustable, upon which the PZT transducers were fixed by double-stick tape. The delay line is shown in Fig. 3.1-2.

The PVF_2 films were biaxially oriented Kureha films of thicknesses 25μm and 12μm. Sample strips were cut 1 cm wide along the roll direction and transverse to this direction. These directions were labelled 1 and 2 respectively. One side of each strip consisted of the factory finished edge which was aligned along the transducer dimension in order to orient the PVF_2. No further, analysis of the film orientation was made and it was assumed that the finished edges were along the symmetry axis. The films were held to the transducer by double stick tape. Measurements were taken for decreasing values of the distance of the polymer film as it was found that removal of the double stick tape distorted the PVF_2 film.

For the propagation of the SH_o model (shear mode), the PVF_2 strip was placed along the length direction of the transducers such that the displacement motions were those of u_3. The

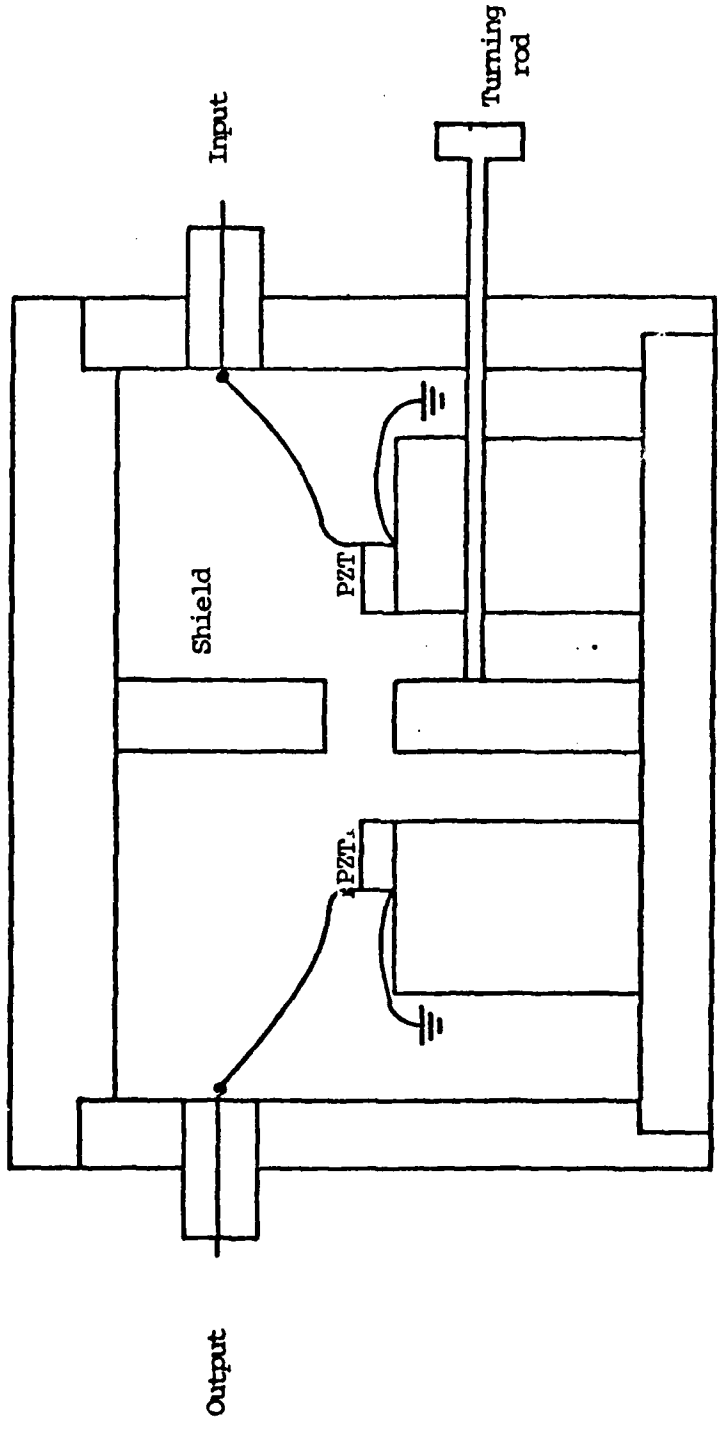

Figure 3.1-2 Delay Line

extensional displacement u_1 was driven by aligning the strip along the width direction of the transducer. (These configurations are illustrated in Fig. 3.1-3).

Two signals were generated, one a pulse mixed with a cw, the other was a cw mode. As shown in Fig. 3.1-4, the mixed pulse and cw were fed into an amplifier before being sent to the delay-line. This amplifier was necessary since 6 to 12 volts was needed to drive the transducers. For the cw measurement the signal was directed to the delay line, the output amplified and connected to a network analyzer. The circuitry is shown in Fig. 3.1-5.

3.2.1 Time Measurements

An output signal in response to the input is shown in Fig. 3.1-6. The input pulse width was kept at 100 μs. For the 180 KHz signal the inout voltage was 6 volts and the output was in the millivolt range. The delay time was measured from the beginning of the output signal to the beginning of that of the input.

Measurements were taken in the continuous wave mode. The resonance peak was located on the network analyzer after each sample was mounted and the phase of the propagating wave was measured as a function of distance. The results were linear and the velocity was determined from the slope. Unfortunately, in order to observe the phase change, the velocities could only be determined with a precision of $\pm$ 7%.

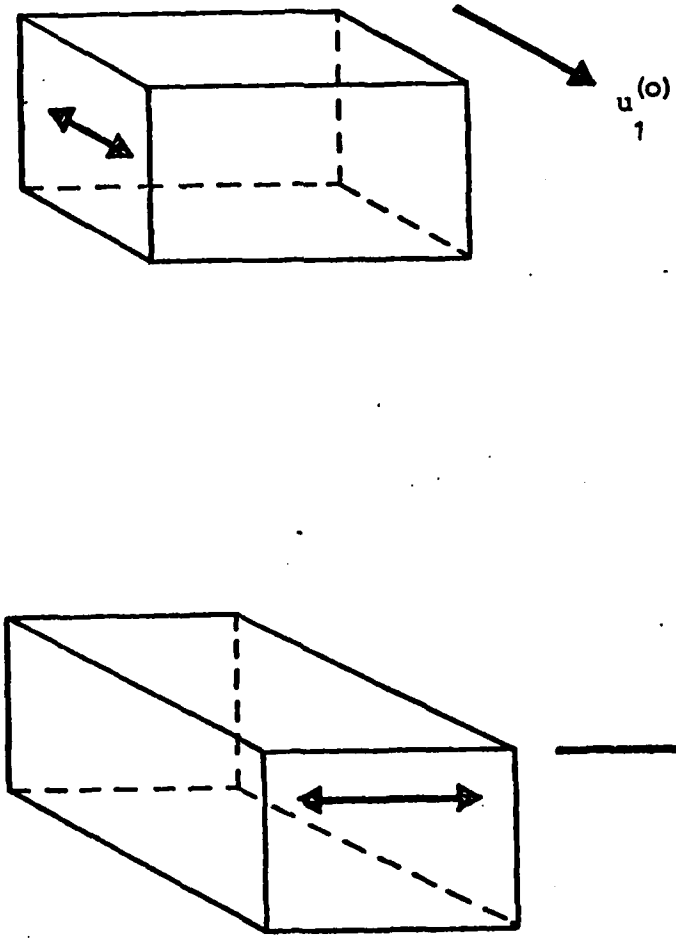

Figure 3.1-3 The allignment of the PZT transducers to generate the displacements $u_1^{(o)}$ and $u_3^{(c)}$.

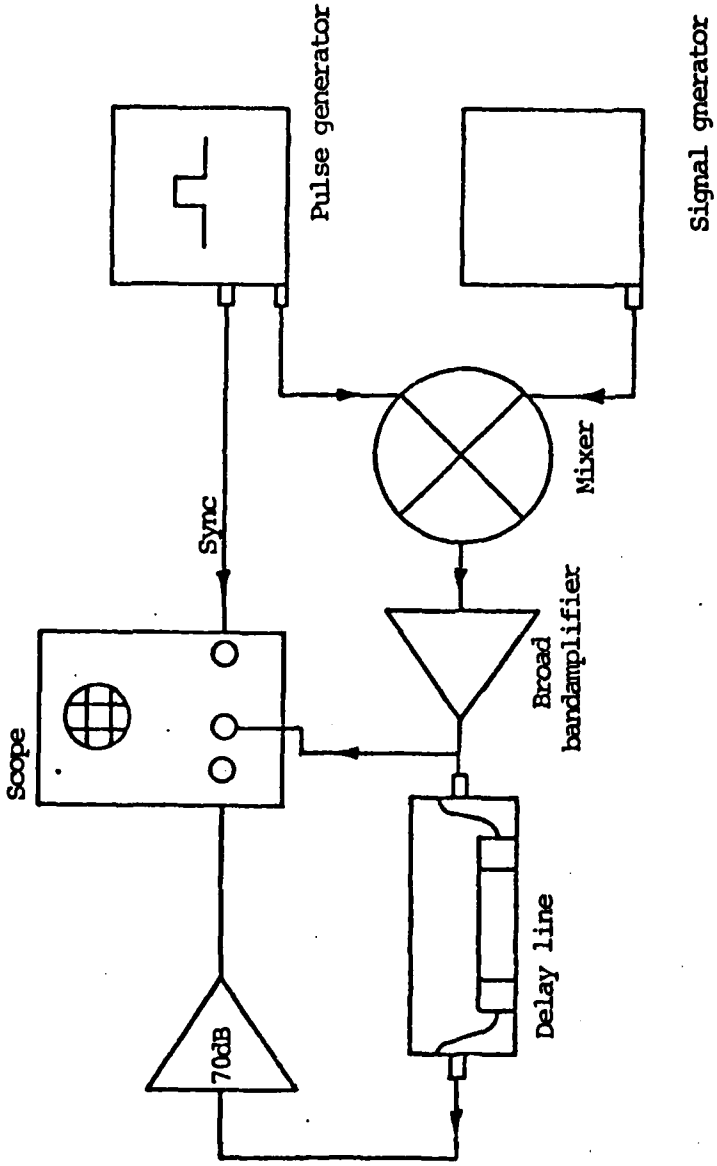

Figure 3.1-4 Mixed Pulse Attenuation Measurement Circuit

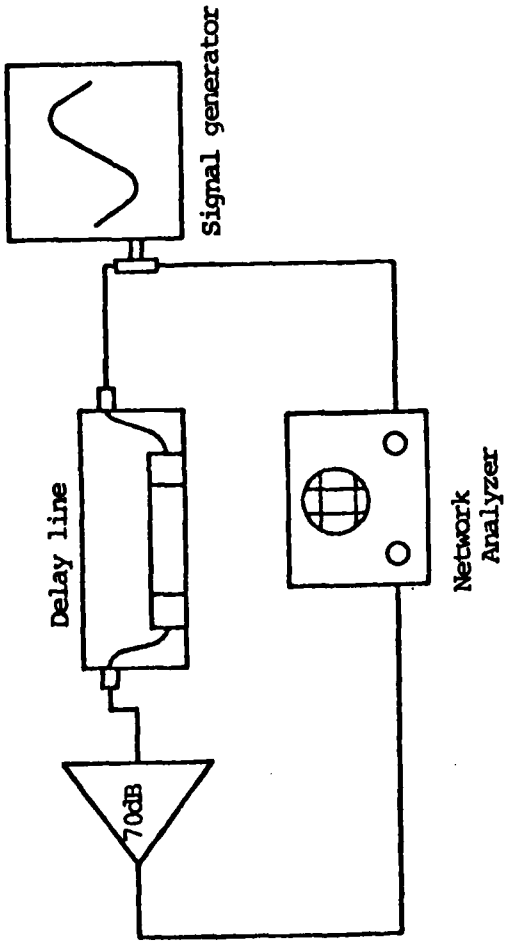

Figure 3.1-5 Continuous wave mode velocity measurement circuit.

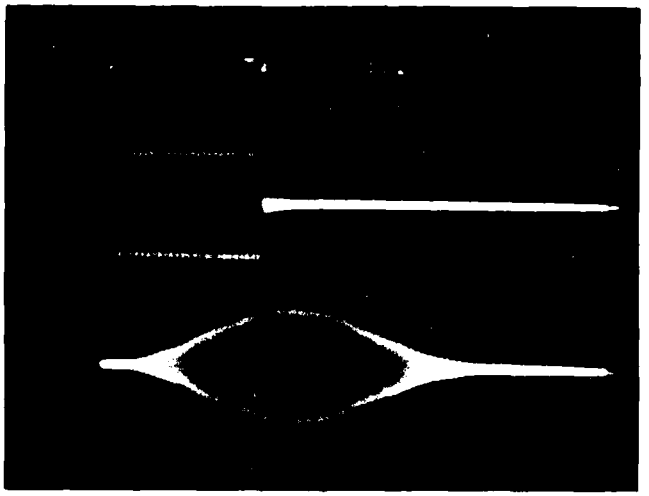

Figure 3.1-6 Input and output for an SH_o wave at 182 KH_z for 25μ PVF_2 film (distance = 1.9cm).

3.2.2 Attentuation Measurements

The attenuation measurements were made by measuring the peak-to-peak values of the output signal. These values were normalized to the input voltage and the decibel loss was plotted against distance. The width of the input pulse was adjusted to 200 μs to insure that the output voltage represented the full illumination of the transducers. An attempt was also made to drive the input transducers with a continuous wave but the output voltage did not monotonically increase with decreasing distance, because of the reflection of the wave by the receiving transducer.

3.2.3 Experimental Results

The measurements of the velocity made at room temperature on PVF_2 along the 1 and 2 axis are listed in Table 3.1-I.

		Velocity (m/s)	
	Axis	12μm	25μm
P_o Wave	1	1728	1897
	2	1656	1704
Sh_o Wave	1	1762	841
	2	1662	893

Table 3.1-I - Velocities in biaxially oriented PVF_2 films. The data are the average of two measurements.

Measurements were taken on two thicknesses, 25 μm and 12 μm. The data for the change of phase angle with distance for the longitudinal wave along the 1 axis are given in Figure 3.1-7. Resolution of the velocities could be made between the 1 and 2 axis for the 25 μm film within limits of the experimental errors.

The attentuations are listed in Table 3.1-II for both shear and longitudinal waves. The shear attenuation values are in agreeement with a linear frequency dependence to data taken at 300 kHz and its overtones.[2]

		Attenuation in dB/cm	
	Axis	12μm	25μm
P_o Wave	1	8.9	10.6
	2	4.4	4.7
Sh_o Wave	1	9.7	10.7
	2	4.5	6.2

Table 3.1-II - Attenuation at 200 kHz in biaxially oriented PVF_2 film. The data are the average of two measurements.

The plate elastic and hysteretic constants according to the theory derived in Equations 3.1-9 and 3.1-10 are given in Table 3.1-III for both thicknesses of PVF_2. Scheyer *et al*[3] suggested that the hysteretic loss may be accorded to a metastable orientation of polymer chains.

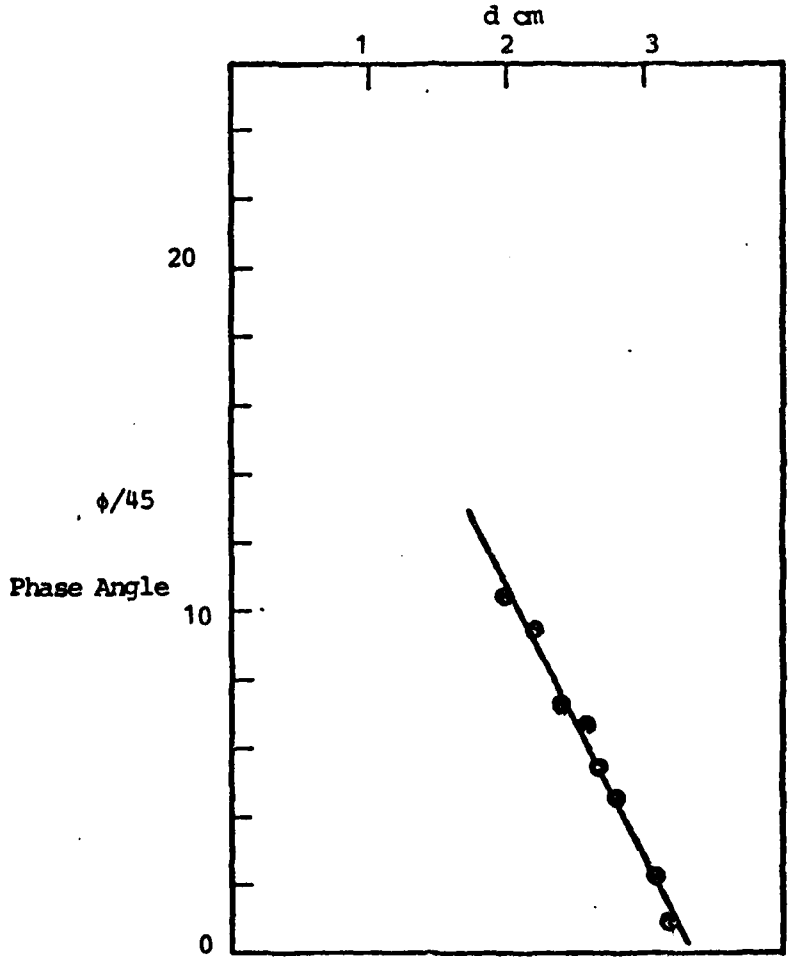

Figure 3.1-7 The velocity data taken at 185 KHz of a P_o wave along 1 axis in 25μ PVF_2. V = 1890 m/sec

Elastic and Hysteresis Constants in N/m^2

	12μm	25μm
$\overline{C_{11}}$	$5.34(10^9)$	$6.44(10^9)$
$\overline{C_{22}}$	$4.91(10^9)$	$5.19(10^9)$
C_{66}(along 1)	$5.55(10^9)$	$1.26(10^9)$
C_{66}(along 2)	$4.94(10^9)$	$1.42(10^9)$
$\overline{h_{11}}$	$1.50(10^9)$	$2.37(10^9)$
$\overline{h_{22}}$	$0.65(10^9)$	$0.76(10^9)$
h_{66}(along 1)	$1.73(10^9)$	$0.21(10^9)$
h_{66}(along 2)	$0.67(10^9)$	$0.14(10^9)$

Table 3.1-III - The elastic and hysteresis loss coefficients as calculated by Equations 17 and 18, where

$$\overline{C_{ii}} = C_{ii} - \frac{C_{i3}^2}{C_{33}} - \frac{h_{33}h_{i3}C_{i3}}{C_{33}^2}$$

and

$$\overline{h_{ii}} = h_{ii} - \frac{C_{i3}h_{3i}}{C_{33}} + \frac{h_{33}C_{i3}^2}{C_{33}^2}$$

An interesting possibility for this orientation effect is a consequence of stress-induced crystallization. The stress wave could stabilize a secondary crystal nucleation site on the crystal that would not be favored by thermodynamic equilibrium under ordinary conditions. Once formed, the lifetime of such metastable nuclei may be enhanced by the crystal bulk and cause a hysteresis effect. Thus the process measurement may cause a reorganization of the sample material.

References

1. R. D. Mindlin, "An Introduction to the Mathematical Theory of the Vibrations of Elastic Plates," Signal Corps Engineering Laboratories, Fort Monmouth, New Jersey, 1955.

2. P. Horvat, J. J. Gagnepain, and B. A. Auld, 1979 Ultrasonics Symp. Proc., 511, (1980).

3. R. D. Scheyer, J. E. Herserman, and E. F. Carome, 1979 IEEE Ultrasonics Symp. Proc., 499, (1980).

4. Y. H. Pao, and R. J. Kaul, "R. D. Mindlin and Applied Mechanics", edited by G. Herrmann, Pergamon Press Inc., New York, 1974.

Chapter 4: Liquid Crystal Lens

4.0 General

Precision optical systems are limited in performance by a variety of phenomena. Manufacturing tolerances, design faults, material instability, and thermal expansion all contribute to performance degradation. Optical theorists commonly determine the performance degradation in terms of the composite effect on the optical path length through the system, especially its variation over the aperture. Good optical performance calls for small optical path length over the aperture. This is true not only for variations within the optics but also for variations in the external propagation path. Thus, when viewing a star through a telescope, the star image which should be a small diffraction pattern may be spread by turbulence produced variations in the atmospheric index of refraction. If these variations could be compensated, the image could be restored to its proper size.

Attempts have been made to actively compensate for the optical path length variations over the aperture of optical systems. This is accomplished by servo deforming a mirror in the optical train by just the right amount to correct the path length errors. To achieve a significant improvement a sizeable number of points on the mirror must be controlled leading to a sizeable number of servo loops. Further, the servos must be provided with a command signal proportional to the desired correction. The servos must have a bandwidth adequate to respond to the temporal variations of the disturbances that are to be corrected. In the field of adaptive optics, systems have been built and have been shown to per-

form as expected(1,2). A significant by-product of this technique is the automatic compensation of both static and dynamic structural path length errors in the optics.

Although mirrors have been the primary mechanism for adaptive optics, any mechanism which changed the optical path length (either distance or index of refraction) could be used.

Lenses play a critical role in almost all optical processing systems. From the crude and inexpensive plastic lens to the diffraction limited, ultra-expensive, finely polished lens made of highly pure material, their role in the optical world is unique. Whatever the application and type of lens, one thing has been common, the need for focusing. The focusing of a lens is accomplished by mechanical motion of one portion of the lens relative to the desired focal plane or correspondingly to other elements of the lens. This mechanical movement, even when electronically controlled, requires sophisticated and expensive hardware to be precise.

This investigation addresses the electronically controlled creation of a lens. Since the actual focusing is electronically operated, it can readily adapt and change the ultimate focal point. Also since the index of refraction is controlled point-to-point on the lens, it can become the mechanism for adaptive optics.

Unlike electronic focus in television cameras and image intensifiers, it is not the bending or positioning of a beam of electrons that is considered. Instead, it is the direct electronic control of the index of refraction.

4.1 Background

Several methods for adaptively changing the focal length of a lens have been investigated. One method is to vary the pressure on a fluid contained in a lens structure (3). It is limited by the small change in index of refraction obtainable by pressure changes. Another technique consists of putting rods or Kerr cell material in front of a lens (4). By varying the voltages across the cylinders, the index of refraction and ultimately the focal length of the entire assembly can be altered. Here, the limitations are granularity of the cylinder stage and the large voltages (kilovolts) required.

Another, much more practical technique is to fill a hollow spherical lens structure with liquid crystal (5). On the inside faces of the structure, transparent electrodes allow varying of the voltage across the cell which alters the index of refraction for appropriately polarized light. Limitations here arise from constraints on cavity size, the lens must be small for uniformity within the liquid crystal, and the inapplicability of other than a single incoming polarization.

Another area of background interest is the small lens formulation by vortex motion within a liquid crystal cell (6). Although not of practical worth as a lens, it does demonstrate the capability of varying the index of refraction within a liquid crystal.

4.2 The Liquid Crystal Lens Design

Lenses are classically created by varying the optical path length over an aperture by radially shaping a medium with a

fixed index of refraction. As Appendix 4A shows, if the structure has parallel walls but the index of refraction is varied, the effect is the same.

All crystals under the influence of an electric field or applied stress exhibit birefringence (7). That is, the index of refraction can be varied (See Appendix 4B). In solids, however, this effect is small since only distortions of the indicatrix are made. Liquid crystals are unique since the molecules re-orient under the influence of an applied field, either electric or magnetic (8). In addition, nematic liquid crystals are uniaxial and the optical axis is coincident with the molecular axis. Thus, as the molecules re-orient in the presence of a field, the entire indicatrix is rotated making large changes in the index of refraction possible (See Appendix 4C).

Liquid crystals can be divided into two groups. If the dielectric tensor is such that the component along the molecular axis (also the optical axis) is greater than the component perpendicular to the axis ($\epsilon_{11} > \epsilon_{\perp}$), the crystal is said to be positive. These molecules align parallel to an applied field. If the reverse is true ($\epsilon_{11} < \epsilon_{\perp}$), the crystal is said to be negative. In this case, the molecules will align perpendicular to an applied field. Either type can be used for creation of a lens. Only the voltages applied to the electrodes will differ as shown in Figure 4.2-1.

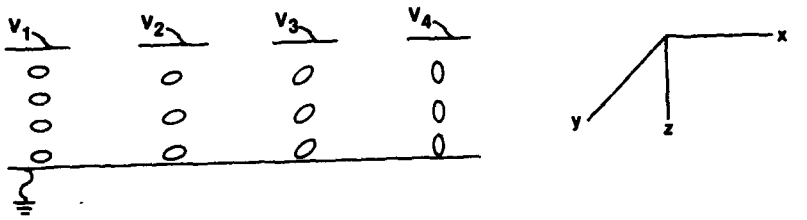

Figure 4.2-1 Cross Section of Liquid Crystal Lens

(See Fig. 4.2-1)

For positive dielectric	For negative dielectric
$V_1 \approx$ (but <) V_{th}	$V_1 > V_2$
$V_2 > V_{th}$	$V_2 > V_3$
$V_3 > V_2$	$V_3 > V_4$
$V_4 > V_3$	$V_4 \approx$ (but <) V_{th} (4.2-1)

With voltages appropriately set

$$n = n_e - \frac{r^2}{2\Delta f} \quad \text{for a wave polarized in X-direction} \qquad (4.2\text{-}2)$$

$$n = n_o \quad \text{for a wave polarized in Y-direction}$$

To obtain total polarization capability there must be a second stage with nematic director having preferential turn in Y-direction.

Consider the case of a positive liquid crystal. In order to have a workable lens, the molecules would be in a homogenous alignment without any voltages applied. Note that this means the axes of all the molecules align in the same direction. This preferential direction for the molecules is established when the lens is fabricated and can be accomplished in a number of ways (11, 19). The simplest method is preferential rubbing of the inside surface prior to assembly. As the voltage is applied across the electrodes above threshold, the molecules tend to align to the field. At

saturation, all but the molecules against the two surfaces will be aligned with the field (See Appendix 4D). If the preferential direction is in the $\hat{x}$-direction as the molecules move, the index of refraction for a wave traveling in the $\hat{z}$-direction and polarized in $\hat{x}$ has changed. The index of refraction for a wave polarized in the $\hat{y}$-direction has remained constant. Figure 4.2-2 shows graphically the alignment state and the corresponding indicatrix location of n, the index of refraction.

Thus Figure 4.2-1 with the light traveling in the $\hat{z}$ direction shows a configuration which with appropriately applied voltages could be a cross-section of a lens for light polarized in the $\hat{x}$-direction. To account for a $\hat{y}$-polarized component a second stage would be required. This would be an identical stage but rotated 90^{o} so that the preferential direction is now in the $\hat{y}$-direction.

It has been assumed in the previous discussion that the electrodes could be configured to give the required radial variation in the index of refraction. During this analytical phase, a great deal of time was spent in considering the electrode structure. What is desired is a radial variation in voltage. It would appear that radially symmetric electrodes would be ideal since they match the symmetry required of the lens. However, they require difficult mask fabrication and any connections made to them create obscurations.

With the trouble encountered using radially symmetric electrodes, rectangular electrodes similar to those used in liquid crystal displays were considered. In this case, it is much easier to address individual electrodes and mask fabrication

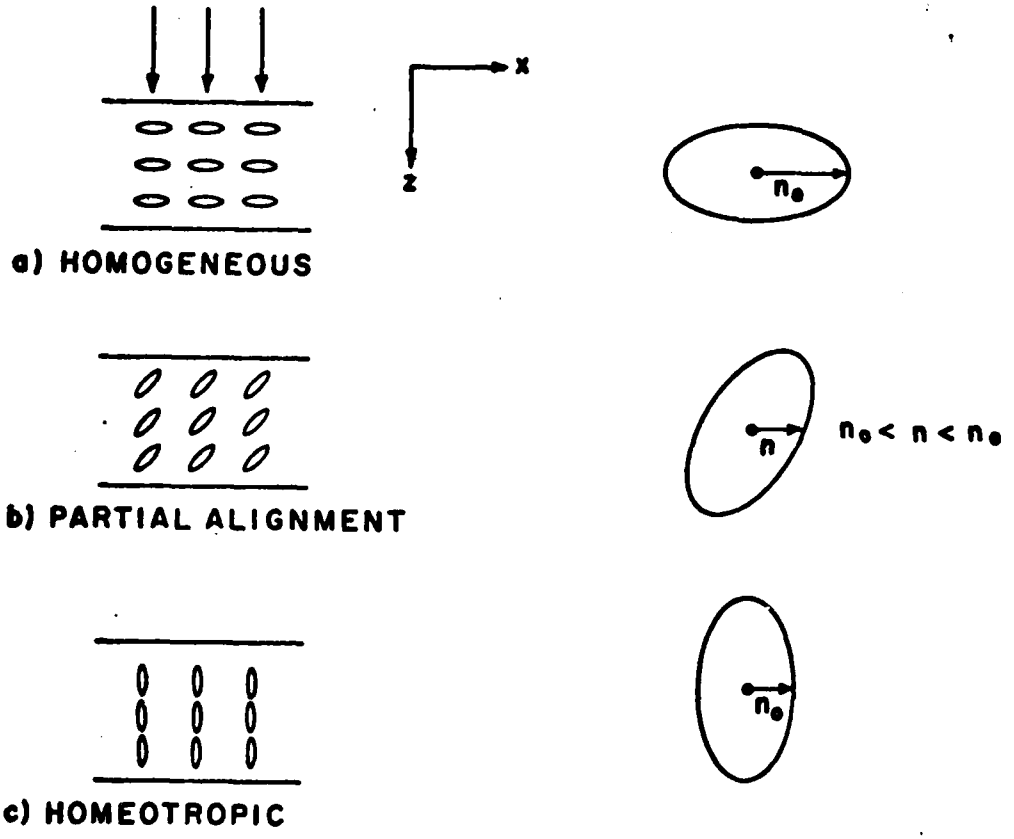

Note: Since angle variation is in X-Z plane, light polarized in Y-direction will be influenced by n_o in all three cases.

Figure 4.2-2 Liquid Crystal Alignment With Light Propagating in the Z-Direction and Polarized in the X-Direction.

is a simple process but the device inherently does not match the symmetry of a lens.

This problem was solved by considering a square aperture of width L centered at the origin. Let the transmission of the aperture be given by

$$t(x,y) = \text{rect}\left(\frac{x}{L}\right) \text{rect}\left(\frac{y}{L}\right) \exp\left[\, jk\Delta n(x) \,\right] \tag{4.2-3}$$

Where

k = wave number

Δ = thickness of the material

and $n(x) = n_e - \frac{|x|^2}{2\Delta f}$ = index of refraction

Just past the aperture, if it is illuminated by a unit-amplitude, normally incident plane wave, the field distribution u_1' is

$$u_1'(x,y) = \text{rect}\left(\frac{y}{L}\right) \text{rect}\left(\frac{x}{L}\right) \exp\left(jk\Delta\left(n_e - \frac{x^2}{2\Delta f}\right)\right) \tag{4.2-4}$$

Ignoring the constant phase term

$$u_1'(x,y) = \text{rect}\left(\frac{y}{L}\right) \text{rect}\left(\frac{x}{L}\right) \exp\left(\frac{-jkx^2}{2\Delta f}\right) \tag{4.2-5}$$

But note, if there was another transmission factor directly in front of the aperture with

$$n(y) = n_e - \frac{y^2}{2\Delta f} \tag{4.2-6}$$

Then

$$\begin{aligned} u_1' &= t,(x,y)\ tt_2(x,y) \\ u_1' &= \text{rect}\left(\frac{y}{L}\right) \text{rect}\left(\frac{x}{L}\right) \exp\left(\frac{-jk(x^2 + y^2)}{2f}\right) \end{aligned} \tag{4.2-7}$$

The ideal form of a lens is obtained with linear electrodes. By cascading two stages not only is the mask fabrication process simplified, the required symmetry is also maintained.

Figure 4.2-3 shows a single stage cross-section and a representative electrode structure. Figure 4.2-4 then shows a complete lens. "Complete" means that it works for all incoming polarizations. Note that four liquid crystal stages are required. Two are needed for $\hat{x}$ polarized light: one giving the required variation in index of refraction in $\hat{x}$ and one giving it in $\hat{y}$. Similarly, for the $\hat{y}$ polarized component, two stages are required.

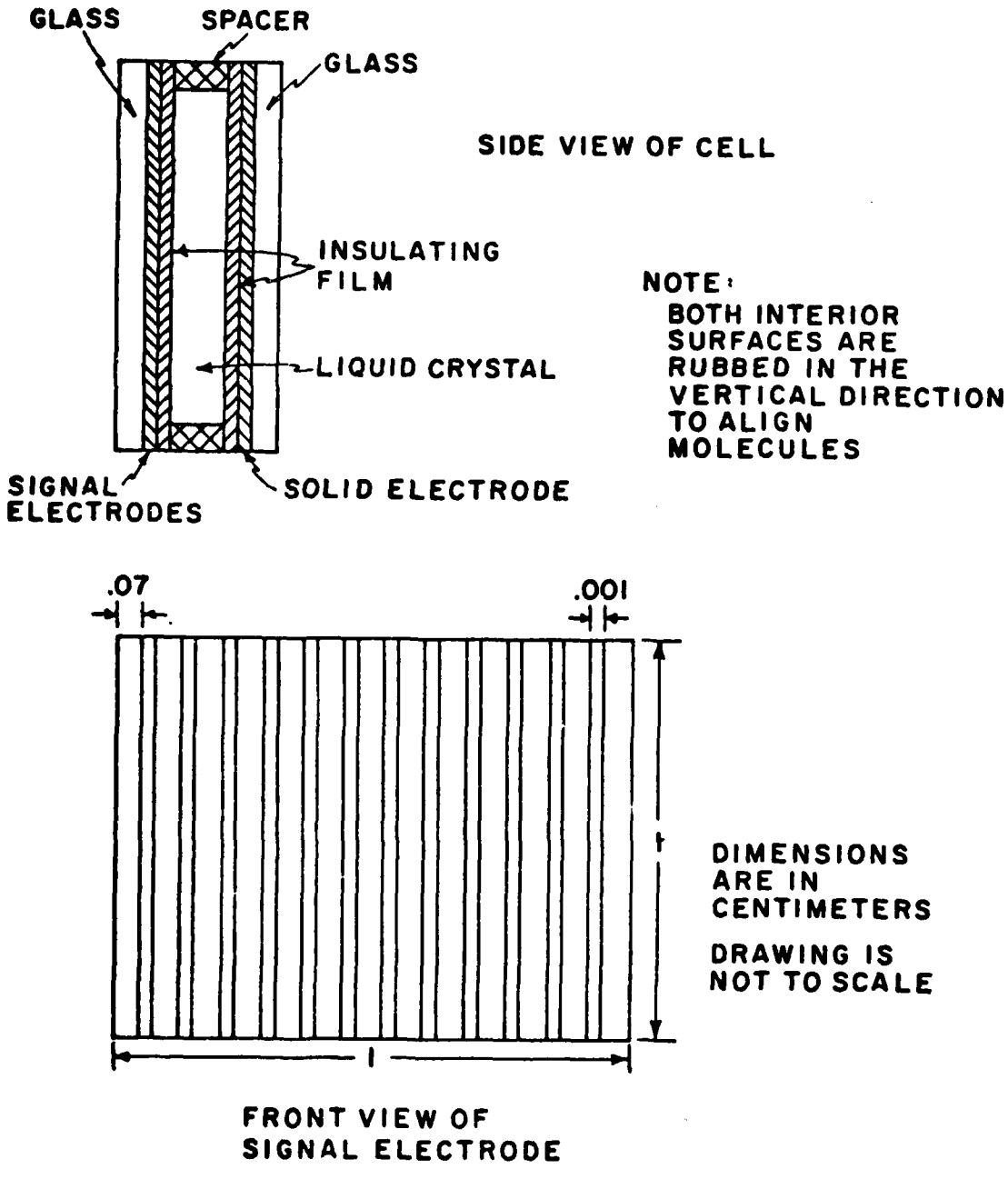

Figure 4.2-3 Single Stage of Liquid Crystal Lens

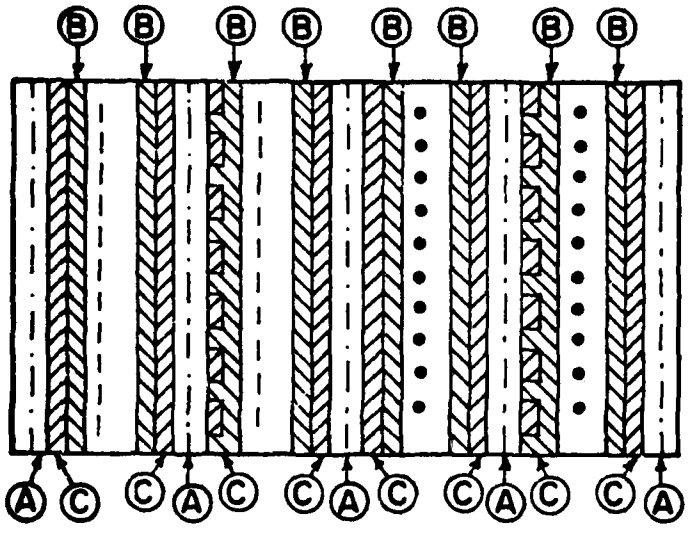

Figure 4.2-4 Four Stage Liquid Crystal Lens

4.3 Liquid Crystal Lens Performance Analysis

Although the lens described previously possesses the radial symmetry in index of refraction variation of a common circular lens, it does represent a square exit or entrance aperture. There is no loss in general applicability by considering the performance of the square configuration since either a round or rectangular field stop would be placed in the lens chain whose size would become the limiting factor or the square configuration could be the desired format (for example in television, infrared, or photographic system with 1 x 1 formats).

The common measure of lens fidelity is the Modulation Transfer Function (MTF). The MTF is the modulus of the Optical Transfer Function (OTF), which specifies the complex weighting factor applied by the system to the frequency component at (f_x, f_y) relative to the weighting factor applied to the zero frequency component.

To evaluate the OTF of the liquid crystal lens, it is first necessary to examine the ideal square lens. Ideal here means diffraction limited. An imaging system is said to be diffraction limited if a diverging spherical wave, emanating from a point-source object, is converted by the system into a wave, again perfectly spherical, that converges toward a point in the image plane.

4.4 Diffraction Limited Square Aperture

Following the nomenclature of Goodman (9), the OTF of a diffraction limited system can be written as

$$H(f_x, f_4) = \frac{\int_{-\infty}^{\infty}\int_{-\infty}^{\infty} P(\xi + \frac{\lambda d_i f_x}{2},\ \eta + \frac{\lambda d_i f_x}{2}) P(\xi - \frac{\lambda d_i f_x}{2},\ \eta - \frac{\lambda d_i f_x}{2}) d\xi d\eta}{\int_{-\infty}^{\infty}\int_{-\infty}^{\infty} P(\xi, \eta) d\xi d\eta} \qquad (4.3\text{-}1)$$

where

$P(x,y)$ = The pupil function

λ = Wavelength of light

d_i = Distance from the pupil to the image

f_x, f_y = Spatial frequencies

If $P(x,y) = \text{rect}\ \frac{x}{\ell}\ \text{rect}\ \frac{y}{\ell}$, (4.3-2)

then

$$\int_{-\infty}^{\infty}\int_{-\infty}^{\infty} P(\xi,\eta) d\xi d\eta = \int_{-\ell/2}^{\ell/2}\int_{-\ell/2}^{\ell/2} d\xi d\eta = \ell^2 \qquad (4.3\text{-}3)$$

and

$$\int_{-\infty}^{\infty}\int_{-\infty}^{\infty} P(\xi + \frac{\lambda d_i f_x}{2},\ \eta + \frac{\lambda d_i f_y}{2}) P(\xi - \frac{\lambda d_i f_x}{2},\ \eta - \frac{\lambda d_i f_y}{2}) d\xi d\eta =$$

$$\int_{\frac{-\ell+\lambda d_i|f_x|}{2}}^{\ell-\frac{\lambda d_i|f_x|}{2}}\int_{\frac{-\ell+\lambda d_i|f_x|}{2}}^{\ell-\frac{\lambda d_i|f_x|}{2}} d\xi d\eta = (\ell - \lambda d_i|f_x|)(\ell - \lambda d_i|f_y|) \qquad (4.3\text{-}4)$$

where

$$|f_x| \leq \frac{\ell}{\lambda d_i}$$

and

$$|f_y| \leq \frac{\ell}{\lambda d_i}$$

Substituting equations (4.3-3) and (4.4-4) into equation (4.3-1) gives the OTF as

$$H(f_x, f_y) = \frac{(\ell - \lambda d_i |f_x|)(\ell - \lambda d_i |f_y|)}{\ell^2} \qquad \begin{matrix} |f_x| \leq \frac{\ell}{\lambda d_i} \\ |f_y| \leq \frac{\ell}{\lambda d_i} \end{matrix} \tag{4.3-5}$$

Let

$$f_c \triangleq \frac{\ell}{\lambda d_i} \tag{4.3-6}$$

f_c then defines the spatial frequency along the axes where the OTF goes to zero. Using the definition of the triangle function, (9) the OTF of the diffraction limited, square aperture can finally be written as

$$H(f_x, f_y) = \Lambda\left(\frac{f_x}{f_c}\right) \Lambda\left(\frac{f_y}{f_c}\right) \tag{4.3-7}$$

4.4 OTF of the Liquid Crystal Lens

Due to the electrode structures used to create the index of refraction variation in the liquid crystal, a diffraction limited lens will not be formed. The wavefront leaving the lens will have phase distortions caused by the approximation of a smoothly

varying index of refraction by a sampled function. Thus, the liquid crystal lens will inherently have aberrations. The effect of those aberrations on lens performance as measured by the predicted OTF is the intent of this section.

The common method for analytically describing aberrations is to model them as a phase-shifting plate within the aperture. If the phase error at a point (x,y) in the aperture is represented by kW(x,y) where $k = \frac{2\pi}{\lambda}$ and W is an effective path-length error, then the complex transmittance $\bar{P}$ of the imaginary phase-shifting plate is given by

$$\bar{P}(x,y) = P(x,y)\exp[jkW(x,y)] \tag{4.3-8}$$

where P(x,y) is the pupil function used in the previous section. The complex function $\bar{P}$ is called the generalized pupil function.

Again following the nomenclature of Goodman (9), let $A(f_x f_y)$ be the area of overlap of

$$P(\xi + \frac{\lambda d_i f_x}{2},\ \eta + \frac{\lambda d_i f_y}{2}) \quad \text{and} \quad P(\xi - \frac{\lambda d_i f_x}{2},\ \eta - \frac{\lambda d_i f_x}{2})$$

When aberrations exist the OTF can then be written as

$$H(f_x, f_y) = \frac{\iint_{a(f_x,f_y)} \exp\{jk[W(\xi+\frac{\lambda d_i f_x}{2},\ \eta+\frac{\lambda d_i f_x}{2}) - W(\xi-\frac{\lambda d_i f_x}{2},\ \eta-\frac{\lambda d_i f_x}{2})\}d\xi d}{\iint_{a(0,0)} d\xi d\eta} \tag{4.3-9}$$

For the liquid crystal lens described previously, since the modulations in x and y are accomplished in successive stages, they

are independent and equation (4-9) can be written

$$H(f_x,f_y) = \frac{\int_{a(f_x)} \exp\{jk[W(\xi + \frac{\lambda d_i f_x}{2}) - W(\xi - \frac{\lambda d_i f_x}{2})]\}d\xi}{\int_{a(0)} d\xi} X$$

$$\frac{\int_{a(f_y)} \exp\{jk[W(\eta + \frac{\lambda d_i f_y}{2}) - W(\eta - \frac{\lambda d_i f_y}{2})]\}d\xi}{\int_{a(0)} d\eta} \qquad (4.3\text{-}10)$$

Only one of the terms (stages in the lens) needs to be considered since the effect in the x-direction is numerically equivalent to that in the y-direction.

Consider the electrode configuration depicted in Figure 4.4-5. The electrodes have appropriate voltages applied so that the index of refraction is identical to that desired at

$$x = \frac{\pm(4n + 1)a}{2} \quad ; \quad n = 0,1,2,\ldots,\frac{N + 1}{2}$$

and N is the number of electrodes. Assuming that the field underneath each electrode is uniform, the error in the index of refraction under the electrode is

$$\delta n(x) = \text{IDEAL} \quad - \quad \text{CREATED}$$

$$\delta n(x) = [n_c - \frac{x^2}{2\Delta f}] - [n_c - \frac{x_o^2}{2\Delta f}] = \frac{x_o^2 - x^2}{2\Delta f} \qquad (4.3\text{-}11)$$

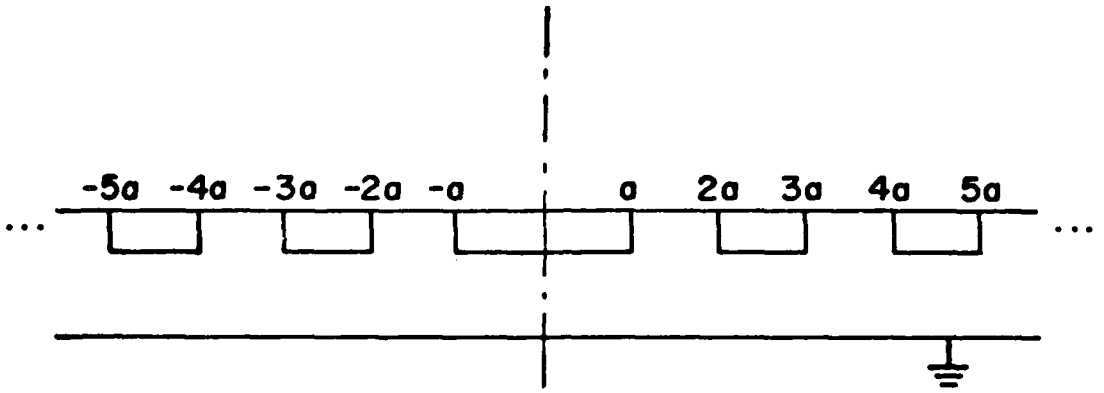

Figure 4.4-5 Liquid Crystal Electrode Configuration For Lens Performance Analysis

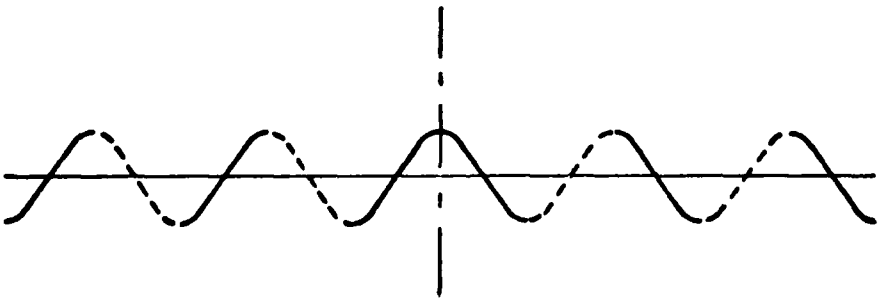

Figure 4.4-6 Error In Index Of Refraction

where x_o represents the center of the electrode. Figure 4.4-6 shows the error in the index of refraction.

In the spaces between electrodes it is assumed that cross-talk exists; i.e., the spacings are small enough that the liquid crystal molecules are reacting to a field strength, the magnitude of which varies between that of the bordering fields established by the two electrodes. If this cross-talk is symmetric, the index of refraction would also be appropriately sampled at $x = \pm \frac{(2n + 1)a}{2}$; $n = 1, 2, \ldots$ The dotted segments in Figure 4.6 illustrate this cross-talk within the spacings.

To account for the cyclic nature of the error in the index of refraction and the increasing error with distance from the center, the error in index of refraction is modelled as

$$\delta n(x) = -a^2\left[\frac{N^2 - (N - \frac{1}{2})^2}{2\Delta f}\right] \cos\left[\frac{\pi x}{a}\right] \qquad (4.3\text{-}12)$$

Equivalently,

$$\delta n(x) = -a^2\left[\frac{(N - \frac{1}{4})a^2}{2\Delta f}\right] \cos\left[\frac{\pi x}{a}\right] \qquad (4.3\text{-}13)$$

The variation given in equation (4.3-11) has been given a constant worst case value.

Now

$$W(x) = \Delta\delta n(x) = -a^2\left[\frac{N - \frac{1}{4}}{2f}\right] \cos\left[\frac{\pi x}{a}\right] \qquad (4.3\text{-}14)$$

Using this expression in the first integral of equation (4.3-10) yields,

$$N(f_x) = \int_{a(f_x)} \exp\{jk[W(\xi+\frac{\lambda d_i f_x}{2}) - W(\xi-\frac{\lambda d_i f_x}{2})]\}d\xi =$$

$$\int_{a(f_x)} \exp\{-jka^2[\frac{N-\frac{1}{4}}{2f}][\cos(\frac{\pi[\xi+\frac{\lambda d_i f_x}{2}]}{a}) - \cos(\frac{\pi[\xi-\frac{d_i f_x}{2}]}{a})]\}d\xi \qquad (4.3\text{-}15)$$

Using

$$\cos(\alpha+\beta) = \cos\alpha\cos\beta - \sin\alpha\sin\beta$$

And

$$\cos(\alpha-\beta) = \cos\alpha\cos\beta + \sin\alpha\sin\beta$$

Equation (4.3-15) can be expanded to

$$N(f_x) = \int_{a(f_x)} \exp\{-jka^2[\frac{N-\frac{1}{4}}{2f}][(\cos\frac{\pi\xi}{a}\cos\frac{\pi\lambda d_i f_x}{2a} - \sin\frac{\pi\xi}{a}\sin\frac{\pi\lambda d_i f_x}{2a})$$

$$- (\cos\frac{\pi\xi}{a}\cos\frac{\pi\lambda d_i f_x}{2a} + \sin\frac{\pi\xi}{a}\sin\frac{\pi\lambda d_i f_x}{2a})]\}d\xi \qquad (4.3\text{-}16)$$

Equivalently,

$$N(f_x) = \int_{a(f_x)} \exp\{jka^2\frac{[N-\frac{1}{4}]}{f}[\sin\frac{\pi\xi}{a}\sin\frac{\pi\lambda d_i f_x}{2a}]\}d\xi \qquad (4.3\text{-}17)$$

For simplicity, let

$$A = \frac{ka^2[N-\frac{1}{4}]}{f} \sin\frac{\pi\lambda d_i f_x}{2a} \tag{4.3-18}$$

So

$$N(f_x) = \int_{a(f_x)} \exp\{jA\sin\frac{\pi\xi}{a}\}d\xi \tag{4.3-19}$$

This expression can be evaluated by expanding the integrand in a Taylor series;

$$e^{jA\sin\theta} = 1 + \frac{jA\sin\theta}{1!} + \frac{[jA\sin\theta]^2}{2!} + \frac{[jA\sin\theta]^3}{3!} + \ldots \tag{4.3-20}$$

and integrating term by term. Considering those integrals in order

$$\int_{a(f_x)} 1d\xi = \int_{\frac{-\ell+ d_i|f_x|}{2}}^{\frac{\ell- d_i|f_x|}{2}} d\xi = \ell- \lambda d_i|f_x|$$

$$\int_{a(f_x)} jA\sin\frac{\pi\xi}{a}\,d\xi \int_{\frac{-\ell+\lambda d_i|f_x|}{2}}^{\frac{\ell-\lambda d_i|f_x|}{2}} jA\sin\frac{\pi\xi}{a}\,d\xi$$

$$= -jA\,\frac{a}{\pi}\left[\cos\frac{\pi}{a}\left(\frac{\ell-\lambda d_i|f_x|}{2}\right) - \cos\frac{\pi}{a}\left(\frac{\ell+\lambda d_i|f_x|}{2}\right)\right.$$

$$= 0 \qquad (4.3\text{-}22)$$

$$\int_{a(f_x)} \frac{A^2}{4}\sin^2\frac{\pi\xi}{a}\,d\xi = \int_{\frac{-\ell+\lambda d_i|f_x|}{2}}^{\frac{\ell-\lambda d_i|f_x|}{2}} \frac{A^2}{2}\sin^2\frac{\pi\xi}{a}\,d\xi$$

$$= -\frac{A^2}{2}\,\frac{a}{\pi}\xi - \frac{a}{4\pi}\sin\frac{2\pi\xi}{a}\Big]_{\frac{\pi}{a}\frac{-\ell+\lambda d_i|f_x|}{2}}^{\frac{\pi}{a}\frac{\ell-\lambda d_i|f_x|}{2}}$$

$$= -\frac{A^2 a}{2\pi}\left[\frac{\pi}{a}\ell-\lambda d_i|f_x|\right) - \frac{1}{2}\left(\sin 2\left[\frac{\ell-\lambda d_i|f_x|}{2}\right] - \sin 2\left[\frac{-\ell+\lambda d_i|f_x|}{2}\right]\right)$$

$$= -\frac{A^2 a}{2\pi}\left[\frac{\pi}{a}(\ell-\lambda d_i|f_x|) - \sin 2\left[\frac{\ell-\lambda d_i|f_x|}{2}\right]\right] \qquad (4.3\text{-}23)$$

The fourth term goes to zero and the rest of the series is small in comparison. Therefore, the numerator, $N(f_x)$, can be found by substituting (4.3-21), (4.3-22), and (4.3-23) into (4.3-19) yielding

$$N(f_x) = [\ell - \lambda d_i|f_x|] - \frac{A^2 a}{2\pi}\left[\frac{\pi}{2a}(\ell - \lambda d_i|f_x|) + \frac{1}{2}\sin(\frac{\pi}{a}\ell - \lambda d_i|f_x|)\right] \tag{4.3-24}$$

Equivalently,

$$N(f_x) = [1 - \frac{A^2}{4}](\ell - \lambda d_i|f_x|) + \frac{A^2 a}{4\pi}\sin(\frac{\pi}{a}[\ell - \lambda d_i|f_x|) \tag{4.3-25}$$

Since

$$H(f_x) = N(f_x)/\int_{a(0)} d\xi = N(f_x)/\ell \tag{4.3-26}$$

Then

$$H(f_x) = (1 - \frac{A^2}{4})\frac{(\ell - \lambda d_i|f_x|)}{\ell} + \frac{A^2 a}{4}\sin(\frac{\pi}{a}[\ell - \lambda d_i|f_x|]) \tag{4.3-27}$$

Equivalently,

$$H(f_x) = (1 - \frac{A^2}{4})\frac{(\ell - \lambda d_i|f_x|)}{\ell} + \frac{A^2}{4}\left[\frac{\sin\frac{\pi}{a}[\ell-\lambda d_i|f_x|]}{\frac{\pi}{a}[\ell-\lambda d_i|f_x|]}\right]\frac{(\ell-\lambda d_i|f_x|)}{\ell} \tag{4.3-28}$$

which, once again using the definitions of the triangle and sinc functions, can be written as

$$H(f_x) = [1 - \frac{A^2}{4} + \frac{A^2}{4} \text{ sinc } (\frac{\ell - \lambda d_i |f_x|}{a})] \Lambda (\frac{f_x}{f_c}) \qquad (4.3\text{-}29)$$

Figure 4.4-7 shows a comparison of two configurations of liquid crystal lenses and the diffraction limit for the aperture they fill.

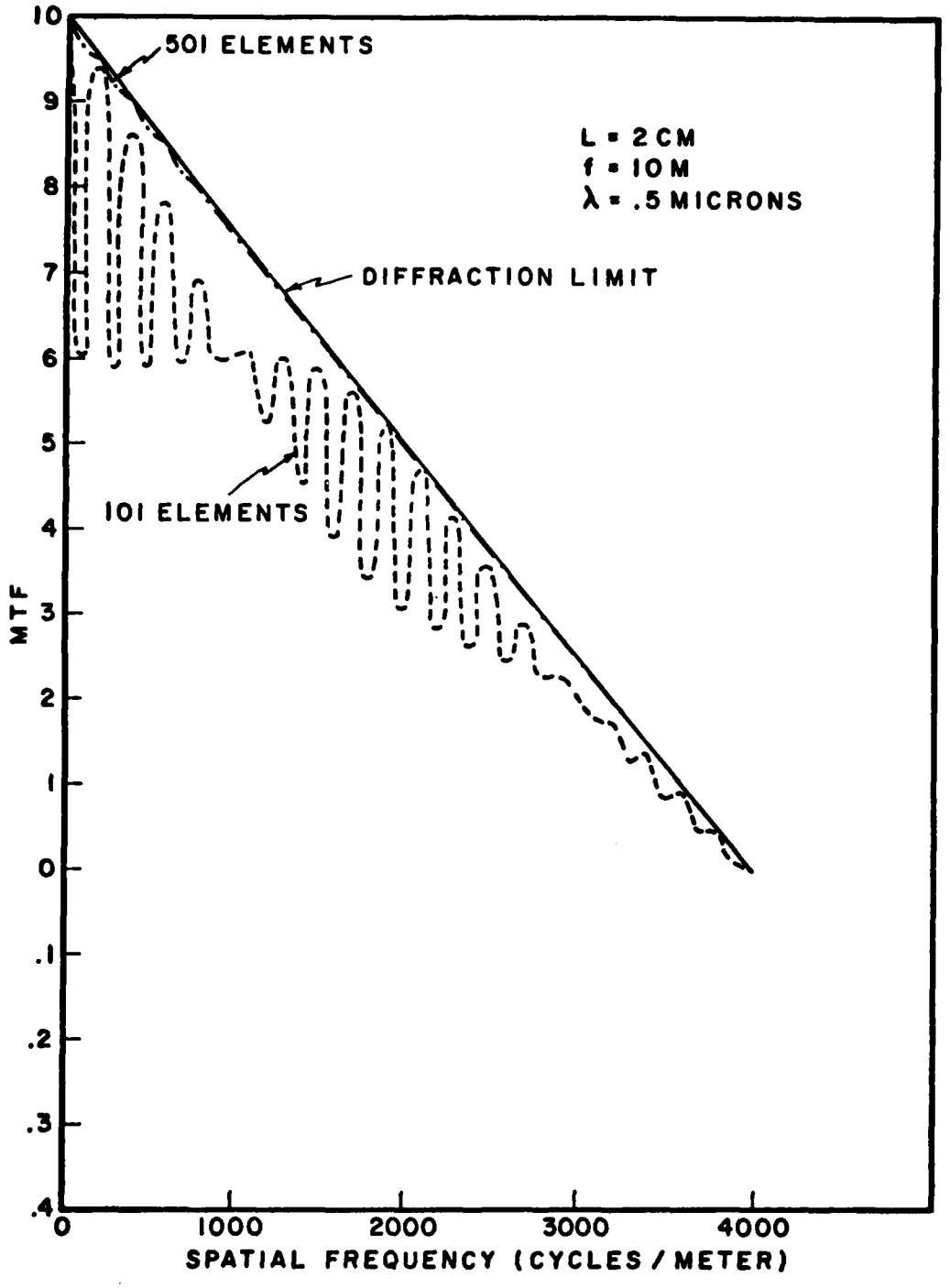

Figure 4.4-7 Comparison of the Modulation Transfer Function of Two Liquid Crystal Lenses.

References

1. Bridges, W. B.; Pearson, J. E.; Hausen, S.; Pedinoff, M. E.; and Nussmeier, T. A.; "Coherent Optical Adaptive Techniques: Design and Performance of an 18-Element Visible Multidither Coat System", Applied Optics, Vol. 15, No. 3.

2. Pearson, James E., "Atmospheric Turbulence Compensation Using Coherent Optical Adaptive Techniques", Applied Optics, Vol. 15, No. 3.

3. Patent No. 3,167,718, DeLuca, W.V., "Fluid Lens of Variable Power", Dec. 15, 1964.

4. Patent No. 3,424,513, Lotspeich, J.F., "Electrooptic Variable Focal Length Lens," June 20, 1966.

5. British Patent No. 1,563,113, Thompson-Brandt, "Variable Focus Liquid Crystal Lens" Sept. 3, 1976.

6. Penz, P. Andrew, "Voltage-Induced Vorticity and Optical Focusing In Liquid Crystals", Physical Review Letters, Vol. 24, No. 25, June 1970.

7. Nye, Physical Properties of Crystals, Oxford Press.

8. Freedericksz, V.; and Zolina, V.; Trans. Faraday Soc., 29, 919, 1933.

9. Goodman, Joseph W., Introduction to Fourier Optics, McGraw Hill, New York 1968.

10. Priestley, E. B. et al, Introduction to Liquid Crystals, Plenum Press, New York 1974.

11. Sprokel, Gerald J., The Physics and Chemistry of Liquid Crystal Devices, Plenum Press, New York 1980.

12. Leui, Leo, Applied Optics: A Guide to Optical System Design/ Volume I, John Wiley and Sons, New York 1968.

13. Southhall, James P. C., Mirrors,Prisms, and Lenses, Dover Publications, 1964.

14. DeGennes, P. G., The Physics of Liquid Crystals, Clarendon Press, Oxford 1974.

15. Schiekel, M. F. and Fahrenschon, K., "Deformation of Nematic Liquid Crystals with Vertical Orientation in Electrical Fields", Applied Physics Letters, Vol. 19, No, 10, Nov. 1971.

16. Schadt, M. and Helfrich, W., "Voltage-Dependent Optical Activity of a Twisted Nematic Liquid Crystal", Applied Physics Letters, Vol. 18, No. 4, Feb. 1971.

17. Kahn, Frederic J., "Electric-Field-Induced Orientational Deformation of Nematic Liquid Crystals: Tunable Birefringence", Applied Physics Letters, Vol. 20, No. 5, March 1972.

18. Creagh, Linda T., "Nematic Liquid Crystal Materials for Displays", Proceedings of the IEEE, Vol. 61, No. 7, July 1973.

19. Kahn, Frederic J., Taylor, Gary N,, and Schonhorn, Harold, "Surface-produced Alignment of Liquid Crystals", Proceedings of the IEEE, Vol. 61, No. 7, July 1973.

Chapter 5: Summary

Our basic goal has been to evaluate the suitability of polymer systems for use in adaptive optics. Structures such as the electrostatically controlled mirrors and lenses described in this report require the mating of materials relatively new to electronics applications with microfabrication technology. Microprocessor technology will be essential in electronically "calibrating" structures with little inherent optical quality.

In the case of deformable mirrors, analysis indicates that elastomer microstructures should be capable of larger deformations than conventional adaptive optical components. Microfabrication creates structures with large area-to-volume ratios. Thus electrostatic forces can overcome inertial forces.

We have verified that such materials can be spread in thin sheets and formed into islands smaller than 20μm on a side. The techniques developed depend on using elastomers which can serve as "resist". Exposed to ultraviolet light through a mask, they are chemically altered and the unwanted portions can then be washed away.

We have also demonstrated that conductive and reflective metal electrodes can be deposited using low temperature conditions. The thin films created should not stiffen the polymer appreciably. Indium is the best material for use in these structures.

Studies of the elastomers revealed basic physical and chemical properties which may prove useful.

The infrared spectra of the polymer systems were correlated to the structural bonds of the silicone polymers. Using this correlation, the kinetics of crosslinking were then followed by comparing the absorbance of the reactive C-C bond to the non reactive C-H bond. Only for polymer system (A) do kinetics as found by IR agreed with those found by swelling measurements.

For the thicker films, the absorbance curves indicates nonideality, possibly due to aggregation of molecules.

In addition to mirror structures, we have studied the concept of a liquid crystal matrix lens. Appropriate voltages will produce a two-dimensional variation of index of refraction, creating a spherical phase front for a plane wave input. Focal lengths of several meters appear possible. A system of four tandem nematic lenses has been shown to provide focussing action for a beam of light with arbitrary transverse polarization. With a dense set of small electrodes, performance approaching diffraction-limited is expected.

Display applications cannot tolerate fringing effects making high resolution difficult to achieve. For the lens application; however, the fringing effect in a high density array should create a graduation in index of refraction greatly improving phase performance.

During the next year, we hope to make continued progress on all aspects of this effort. Experiments are planned to expand our microfabrication capabilities. The newly developed

pattern generator will be used to write directly on the elastomer films with a focussed beam of ultraviolet light from an argon ion laser. Near U.V. wavelengths will be obtained by special mirrors, while the far U.V. will be introduced by doubling visible light in non-linear crystal. This technique will free us from the need to subject these delicate films to contact "printing" in the mask aligner.

At higher power levels, we will attempt to pyrolyze elastomers which do not crosslink in U.V. light. Thus, new materials may become available for microstructure fabrication.

Most of our deflection experiments used one-dimensional arrays, rather than islands. We will try to develop techniques for producing bending structures to produce greater deflection.

We expect to fabricate a lens based on straight nematic liquid crystals rather than the commercially available twisted nematics. Experimental work should reveal the ultimate limitations to be overcome in order to produce a true image forming lens.

APPENDIX 1A

Static Deflection of Microplates

Let us estimate the requires elastic constant of the elastomer and the magnitude of the applied voltage.

The torque required for bending the elastomer is supplied by the forces acting between the charges on the aluminum films. The maximum torque, fortunately, occurs at the foot of the elastomer "L". That is, it occurs where the elastomer is joined to the substrate as shown in Fig. 1.1-2.

The radius of curvature ρ at the foot of the elastomer "L" is inversely proportional to the applied bending moment M and proportional to the longitudinal stiffness constant c of the elastomer and to the moment of inertia I of the elastomer cross-section.

$$\rho = \frac{Ic}{M}. \tag{1A.1}$$

The deflection angle θ in radians of the elastomer "L" is approximately equal to

$$\theta \approx \frac{2b}{\rho} \tag{1A.2}$$

The moment of inertia I of a rectangular cross-section with dimensions b and w about an axis perpendicular to the projection of the structure shown in Fig. 1.1-2, and located at y = 0, is

$$I = \frac{wb^3}{12} \tag{1A.3}$$

where w is the dimension perpendicular to the projection of the structure shown in Fig. 1.1-2. Combining equations 1A.1, 1A.2, and 1A.3 we obtain for the deflection angle θ

$$\theta = \frac{24M}{wb^2C} \tag{1A.4}$$

Let us next estimate the bending moment M due to the force between charges on the aluminum films, assuming the two aluminum films form a parallel plate capacitor. Granted, this is a fairly crude assumption. The stored energy U in this capacitor at constant potential V is

$$U = \frac{1}{2} CV^2. \tag{1A.5}$$

The capacitance C between the plates is

$$C = \varepsilon_0 \varepsilon \frac{aw}{b} \frac{1}{1 + \frac{g}{b}\varepsilon} \tag{1A.6}$$

where g is the width of the air gap and ε is the relative dielectric constant of the elastomer. Here ε_0 is the dielectric constant of vacuum. The dimensions a and b are shown in Fig. 1.1-2. The effective force F on the upper film is equal to the change of the stored energy U with the air gap g at constant potential V

$$F = -\frac{dU}{dg}. \tag{1A.7}$$

Combining equations 1A.5, 1A.6, and 1A.7 we obtain for the force

$$F = \varepsilon_0 \frac{\varepsilon^2}{[1 + \frac{g}{b}\varepsilon]^2} \frac{aw}{2b^2} V^2 \qquad (1A.8)$$

assuming that the air gap g is equal to the dimension b as shown in Fig. 1.1-2. Defining the effective relative dielectric constant K of this system

$$K = \frac{\varepsilon^2}{[1 + \varepsilon]^2}, \qquad (1A.9)$$

the force dF on an incremental length dx of the capacitor is

$$dF = \varepsilon_0 K \frac{wV^2}{2b^2} dx. \qquad (1A.10)$$

The applied bending moment M due to these electrostatic forces is

$$M = \int_{b/2}^{b/2+a} x \, dF. \qquad (1A.11)$$

Upon substituting equation 1A.10 into 1A.11 we obtain for the bending moment

$$M = \frac{1}{4} \varepsilon_0 K w V^2 \frac{a}{b} [1 + \frac{a}{b}]. \qquad (1A.12)$$

Substituting equation 1A.12 into equation 1A.4 we obtain for the deflection angle

$$\theta = \frac{6\varepsilon_0 K}{c} \frac{V^2}{b^2} \frac{a}{b} [1 + \frac{a}{b}] \qquad (1A.13)$$

Assuming a deflection angle of 20^o (and an addition deflection of 10^o at the knee of the "L") for a total deflection of about 30^o, with a value of 5.10^6 volts per meter for V/b, a length to thickness ratio a/b = 2 for the elastomer arm, and a relative dielectric

constant ε of the elastomer of about 4, we require an elastic stiffness constant of the elastomer of about $1.5 \cdot 10^4$ N/m^2, so that for a value of b equal to 5 μm we obtain 25 volts for the applied voltage. This is quite reasonable.

There will also be some deflection due to the force of gravity. The gravitational bending moment is

$$M_g = \sigma g b^2 w [2b + \frac{3}{2} a] \qquad (1A.14)$$

where σ is the density of the elastomer and g is the acceleration of gravity.

Calculation yields for the ratio of the gravitational deflection angle θ_g to the electrostatic deflection angle θ

$$\frac{\theta_g}{\theta} = \frac{4}{\varepsilon_0 K} \frac{g}{V^2} b^2 \frac{[2 + \frac{3a}{2b}]}{\frac{a}{b}[1 + \frac{a}{b}]} \qquad (1A.15)$$

This ratio is proportional to the linear dimension of the structure. Thus, the gravitation deflection angle would be about 4^o:35' for a device with b = 1mn. And, of course, the required voltage is also proportional to the linear dimension. For a device with b = 1 mn the required voltage would have to be 5000V. And, of course, a large device is thus more succeptable to acceleration forces.

One further note, even though not proven here, is that the selfresonant frequency is inversely proportional to the linear dimension. Also the response time is linearly proportional to the linear dimension. Thus a 5 μm system responds about 200 times faster than a 1mn system.

APPENDIX 2A

Experimental Swelling Procedure For Crosslinked Gel

2A.1 Materials:

Spectral grade hexane

Petri dish with glass plate cover

Planchette

Balance

Vacuum oven

2A.2 Crosslink Density

A sample of the network should be weighed dry and placed in a sufficient amount of spectral grade hexane such that it is completely immersed. The dish is covered and the gel is swollen for two days; it is then removed from the hexane and blotted twice to remove excess hexane. The gel is then placed in another dish and cover (preweighed) to determine absorbed hexane. The temperature should remain constant at $25\pm1^{\circ}C$.

2A.3 Sol Content (Uncrosslinked Material)

To determine the amount of uncrosslinked material decant the supernatant hexane into a weighed planchette. Wash the gel and swelling flask or dish with hexane again and pour into planchette.

Place the planchette and its contents into a vacuum oven at $35^{\circ}C$ until the contents are evaporated dry. Reweigh the planchette and determine the sol fraction.

APPENDIX 2B

Formulations of Silicone Gels

The materials were formulated in the following ratios :

System A

X_2-7077	97 pts. by weight
X_2-7078	3 pts. by weight

System B

X_2-7079	75 pts. by weight
X_2-7080	25 pts. by weight

Dielectric Gel

Q_3-6527 A	50 pts. by weight
Q_3-6527 B	50 pts. by weight

APPENDIX 2C

Rheology of Spin-coating Process

The rheology of the spin-coating process has been studied by Washo (1) based on the assumptions that:

(i) the spinning fluid is Newtonian;

(ii) no evaporation loss of the solvent occurs;

(iii) no body or surface forces affect the process.

Washo found that the spinning process could be described by the relation:

$$t = KC^a F^b \qquad (2C\text{-}1)$$

where t is the film thickness, F is the rotational speed of the disk, C is the volume fraction of polymer in the spinning process, and a, b, and K are constants. A similar investigation of spin-coating of electronic resists has been done by Lai (2).

The log of the thickness of microcomponents (Table (2C-I) versus the log of the rotating speed F is plotted in Figure(2C-1) for both ultraviolet curable Systems A and B. The average value of b in Equation (2C-1) obtained from these samples was different from the theoretical value (-0.67). This difference may be due to the fact that no solvent was used in this study, the substrate geometry, and the viscoelastic behavior of the polymers.

Table 2C-I

Film Thickness VS. Spinning Speed

Speed (rpm)								
Thickness(μm)	800	1200	1600	2000	2400	2800	3200	3600
System A	45	32.5	30	25	20	17.5	15	12.5
System B	40	30	20	16.2	13.7	11.2	10	7.5

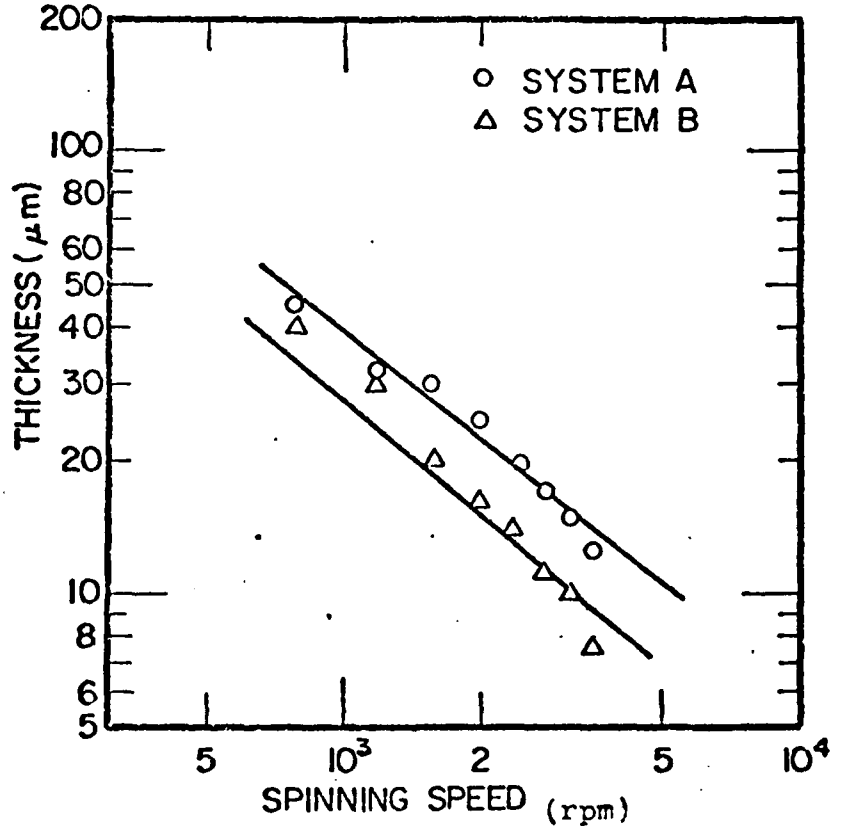

Figure 2C-1 Film thickness vs. spinning speed

References

1. B. D. Washo, IBM, J. Res. Dev., 21, 190 (1977).

2. J. H. Lai, Polym. Eng. Sci., 19, 1117 (1979).

APPENDIX 3A

Viscoelastic Wave Equations

3A.1

In the derivation that follows, we assume the constituitive relations for a viscous loss; however, except for the boundary conditions on some of the displacements, the form of the dispersion relations can readily be adopted to a hysteretic loss, due to the symmetry of the constituitive constants.

We now consider the generalization of the equations of motion to allow for a dissipative term. The equations of motion of a particle are given by the extremum principle

$$\delta \int_1^2 (T + W)dt = 0 \qquad (3A\text{-}1)$$

where T is the kinetic energy and W is the work.

The generalized work, W, can be separated into two terms

$$W = \Sigma_j T_j \delta q_j + \Sigma_j Q_j \delta q_j \qquad (3A\text{-}2)$$

where q_j is a generalized coordinate, T_j is a generalized force that is derivable from a potential and Q_j is a force that is non-conservative and therefore not derivable from a potential. This force is the source of the loss term that is incorporated into Mindlin's theory. After performing the variations with respect to generalized modes we find the analogous equations of motion for a continuum to be

$$\int_V \int_{t_1}^{t_2} (\rho \ddot{u}_j - T_{ij,i})\delta u_j dVdt = \int_V \int_{t_1}^{t_2} Q_{ij,i} \delta u_j dVdt \qquad (3A\text{-}3)$$

where ρ is the density, u_j is the modal displacement, T_{ij} and Q_{ij} are stresses corresponding to conservative and nonconservative potentials respectively. These equations are reduced to planar equations by assuming the three-dimensional displacements to be written in a power series in the thickness coordinate as

$$u_j = \Sigma_n x_2^n \, u_j^{(n)} \, (x_1, x_3, t) \qquad (3A\text{-}4)$$

The superscript on the displacement refers to an index for u_j. By judiciously choosing $u_j^{(n)}$, the equations of motion of the three lowest frequency modes may be approximated in the long wavelength, low frequency limit. These modes are, in increasing order of frequency, the flexural, the straight-crested thickness shear, and thickness extensional modes as shown in Fig. 3.1-1. It is fairly obvious that a combination of a few displacement fields are necessary to generate these solutions. The choice of these displacements are listed by order index and are illustrated in Fig. 3A-1.

The zeroth order are rigid displacements along x_j; the first order displacements contain a nodal plane and are antisymmetric with respect to this plane. The second order displacements are symmetric with respect to the nodal plane.

3A.2 Stress Equations of Motion

Upon substituting the power series into the variational equation (3A-3), and integrating over the thickness the remaining integrations are over the cross sectional area and time. Since the variations are arbitrary the integral yields the equation of motion

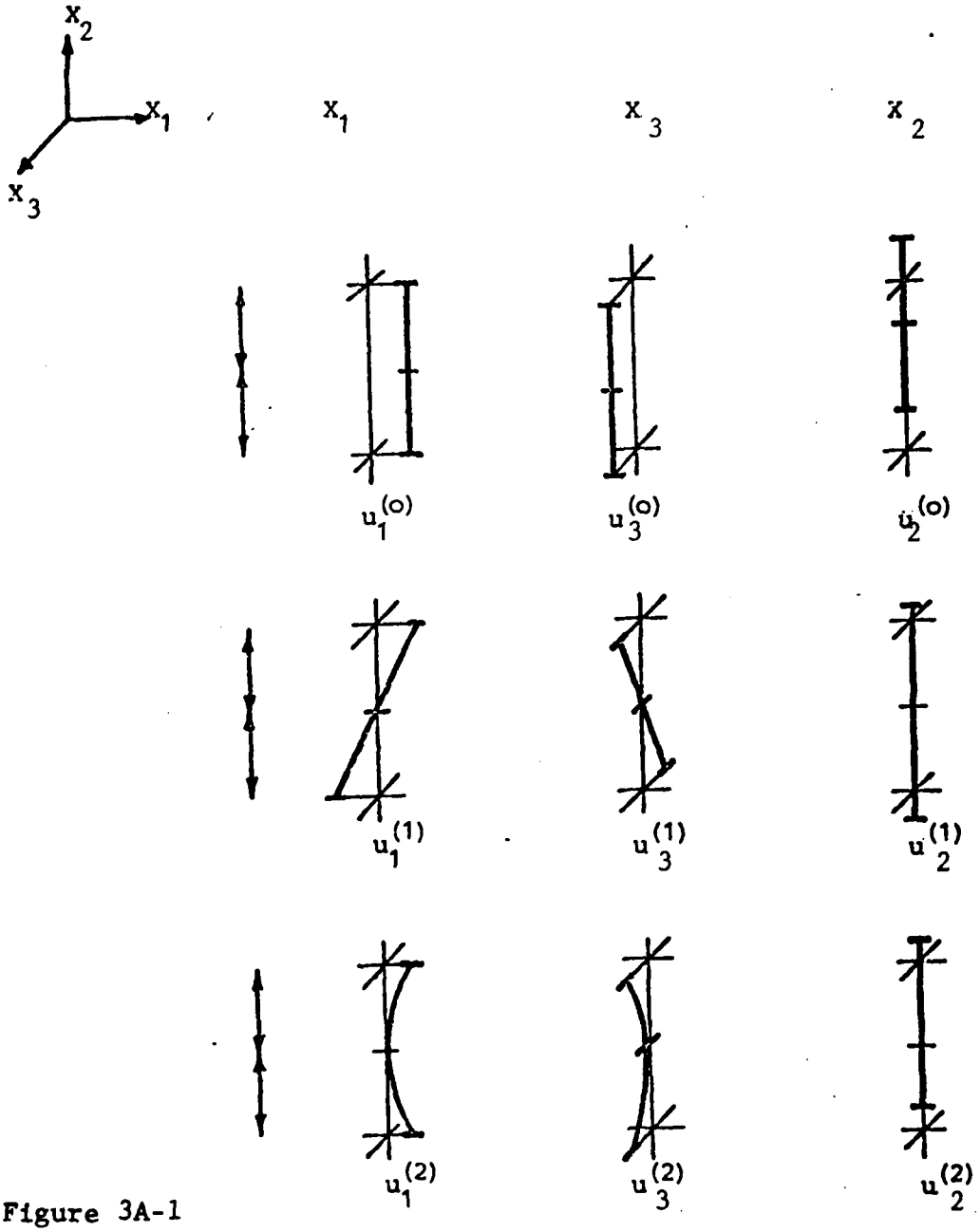

Figure 3A-1

The zeroth, first and second orders of the planar displacements. (after Mindlin, ref. 1, Sec. 3.0).

AD-A105 707 SYRACUSE UNIV NY DEPT OF ELECTRICAL AND COMPUTER EN--ETC F/G 11/9
POLYMERIC MICROELECTRONICS.(U)
JUN 81 S T KOWEL, E BALIZER, T T SU, I H LOH N0AAK70-80-C-0053
UNCLASSIFIED TR-81-6 NL

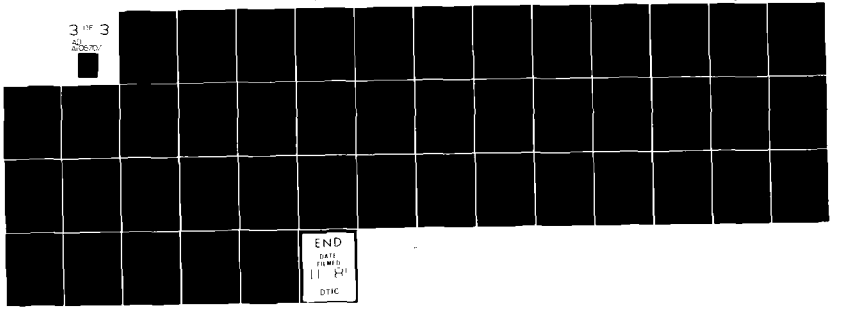

$$T^{(n)}_{ij,i} - nT_{3j} + F^{(n)}_j - \rho B_{mn} u_j^{(m)} = -(Q^{(n)}_{ij,i} - nQ^{(n-1)}_{2j} + O^{(n)}_j) \tag{3A-5}$$

where for = 1,3

$$T^{(n)}_{ij} = \int_{-b}^{b} x_2^n \, T_{ij} dx_2$$

$$Q^{(n)}_{ij} = \int_{-b}^{b} x_2^n \, Q_{ij} dx_2 \tag{3A-6}$$

for i = 2 integration by parts yields

$$T^{(n)}_{2j,2} = F^{(n)}_j - nT^{(n-1)}_{2j}$$

$$Q_{2j,2} = Q^{(n)}_j - nQ^{(n-1)}_{2j} \tag{3A-7}$$

where $Q^{(n)}_j$ and $F^{(n)}_j$, are the nth order surface traction contributions

where $F^{(n)}_j = \int_{-b}^{b} x_2^n \, T_{2j} dx_2$

and $Q^{(n)}_j = \int_{-b}^{b} x_2^n \, Q_{2j} dx_2$

and where

$$B_{mn} = \frac{2b^{m+n+1}}{(m+n+1)} \qquad \text{for } m + n \text{ even}$$

$$= 0 \qquad \text{for } m + n \text{ odd} \tag{3A-8}$$

Strain

3A.3

The substitution of the power series of the displacements into the strain tensor

$$S_{ij} = \tfrac{1}{2}(u_{i,j} + u_{j,i})$$

yields

$$= \tfrac{1}{2} \Sigma S_{ij}^{(n)} X_2^n \qquad (3A\text{-}9)$$

where

$$S_{ij}^{(n)} = u_{i,j}^{(n)} + u_{j,i}^{(n)} + (n + 1)(\delta_{2j} u_1^{(n+1)} + \delta_{2i} u_j^{(n+1)}$$

Constituitive Relations

3A.4

The conservative stresses are given by Hooke's law as

$$T_{ij} = C_{ijkl} S_{kl} \qquad (3A\text{-}10)$$

The nonconservative stresses that occur in the variational principle are derived in the case of linear viscoelasticly from the Rayleigh dissipation function:

$$\Psi = \tfrac{1}{2} \eta_{ijkl} \dot{S}_{ij} \dot{S}_{kl}$$

$$Q_{ij} = \frac{\partial \Psi}{\partial \dot{S}_{kl}}$$

$$= \eta_{ijkl} \dot{S}_{kl} \qquad (3A\text{-}11)$$

The constituitive equation that is developed by combining both stress contributions is

$$t_{ij} = C_{ijkl}S_{kl} + \eta_{ijkl}\dot{S}_{kl} \qquad (3A\text{-}12)$$

In terms of the planar tensors we find

$$t_{ij} = C_{ijkl}S^{(n)}_{kl} + \eta_{ijkl}\dot{S}^{(n)}_{kl}$$

3A.5 Truncation and Reduction to the Low Frequency of Thin Plates

. The previous formalism can be used to the first order (n = 1) and boundary conditions can be imposed to reduce the set of differential equation to an uncoupled flexural and two extensional modes.

The equations of motion for the first six lowest modes are obtained from the zeroth and first order approximation; they are

$$T^{(o)}_{11,1} + Q^{(o)}_{11,1} + T^{(o)}_{31,3} + Q^{(o)}_{31,3} = 2b\,\rho\ddot{u}^{(o)}_1$$

$$T^{(o)}_{12,1} + Q^{(o)}_{12,1} + T^{(o)}_{32,3} + Q^{(o)}_{32,3} = 2b\,\rho\ddot{u}^{(o)}_2$$

$$T^{(o)}_{13,1} + Q^{(o)}_{13,1} + T^{(o)}_{33,3} + Q^{(o)}_{33,3} = 2b\,\rho\ddot{u}^{(o)}_3$$

$$T^{(1)}_{11,1} + Q^{(1)}_{11,1} + T^{(1)}_{31,3} + Q^{(1)}_{31,3} - T^{o}_{21} - Q^{o}_{21} = \frac{2b^3}{3}\rho\ddot{u}^{(1)}_1$$

$$T^{(1)}_{12,1} + Q^{(1)}_{12,1} + T^{(1)}_{32,3} + Q^{(1)}_{32,3} - Q^{o}_{22} - T^{o}_{22} = \frac{2b^3}{3}\rho\ddot{u}^{(1)}_2$$

$$T^{(1)}_{13,1} + Q^{(1)}_{13,1} + T^{(1)}_{33,3} + Q^{(1)}_{33,3} - Q^{o}_{23} - T^{o}_{23} = \frac{2b^3}{3}\rho\ddot{u}^{(1)}_3 \qquad (3A\text{-}13)$$

The displacements $u_{ij}^{(o)}$ are governed by the stress resultants $T_{ij}^{(o)}$ and $Q_{ij}^{(o)}$ whereas the rotation $u_{ij}^{(1)}$ contain contributions from both the moments $T_{ij}^{(1)}$, $Q_{ij}^{(1)}$ and the stress resultants.

The Stress Strain Relations

The conditions on the truncation of the displacements and boundary conditions for the first order equations of motion are

$$u_i^{(n)} = 0 \qquad n > 1 \quad i = 1,3$$
$$u_2^{(n)} = 0 \qquad n > 2 \tag{3A-14}$$

The tractions $\ddot{u}_2^{(1)} = 0 = \dot{u}_2^{(1)} = \dot{u}_2^{(2)}$ vanish at the surface as well as the following stresses:

$$t_{22}^{(1)} = t_{21}^{(1)} = t_{23}^{(1)} = 0$$

At the first order the kinetic and potential energies contain the displacements $u_2^{(2)}$ and $u_2^{(1)}$. The equations of motion may be reduced to the classical extensional equations if these displacements are not coupled into them. The above assignments of vanishing stresses do not allow these displacements to appear in the energy term or in the equations of motion. Those boundary conditions result in equations valid at low frequencies since $u_2^{(1)}$ and $u_2^{(2)}$ become appreciable for thickness modes whose frequencies are greater than those of the extensional modes.

The zeroth order equations become upon eliminating $S_{22}^{(o)}$ from the constraint on $t_{22}^{(o)}$:

$$t_{11}^{(o)} = 2b\,[c'_{11}u_{1,1}^{(o)} + c'_{13}u_{3,3}^{(o)} + c'_{14}\,(u_{2,3}^{(o)} + u_3^{(1)}$$

$$+ c'_{15}\,(u_{3,1}^{(o)} + u_{1,3}^{(o)}) + c'_{16}\,(u_{2,1}^{(o)} + u_1^{(1)})$$

$$+ \eta'_{11}u_{1,1}^{(o)} + \eta'_{13}u_{3,3}^{(o)} + \eta'_{14}\,(\dot{u}_{2,3}^{(o)} + \dot{u}_3^{(1)})$$

$$+ \eta'_{15}\,(\dot{u}_{3,1}^{(o)} + \dot{u}_{1,3}^{(o)}) + \eta'_{16}\,(\dot{u}_{2,1}^{(o)} + \dot{u}_1^{(1)})]$$

$$t_{33}^{(o)} = 2b\,[c'_{31}u_{1,1}^{(o)} + c'_{33}u_{3,3}^{(o)} + c'_{34}\,(u_{2,3}^{(o)} + u_3^{(1)})$$

$$+ c'_{35}\,(u_{3,1}^{(o)} + u_{1,3}^{(o)}) + c'_{36}\,(u_{2,1}^{(o)} + u_1^{(1)})$$

$$+ \eta'_{31}u_{1,1}^{(o)} + \eta'_{33}\dot{u}_{3,3}^{(o)} + \eta'_{34}\,(\dot{u}_{2,3}^{(o)} + \dot{u}_3^{(1)})$$

$$+ \eta'_{35}\,(\dot{u}_{3,1}^{(o)} + \dot{u}_{1,3}^{(o)}) + \eta'_{36}\,(\dot{u}_{2,1}^{(o)} + u_1^{(1)})]$$

$$t_{23}^{(o)} = 2b\,[c'_{41}u_{1,1}^{(o)} + c'_{43}u_{3,3}^{(o)} + c'_{44}\,(u_{2,3}^{(o)} + u_3^{(1)})$$

$$+ c'_{45}\,(u_{3,1}^{(o)} + u_{1,3}^{(o)}) + c'_{46}\,(u_{2,1}^{(o)} + u_1^{(1)})$$

$$+ \eta'_{41}\,\dot{u}_{1,1}^{(o)} + \eta'_{43}\dot{u}_{3,3}^{(o)} + \eta'_{44}\,(\dot{u}_{2,3}^{(o)} + \dot{u}_3^{(1)})$$

$$+ \eta'_{45}\,(\dot{u}_{3,1}^{(o)} + \dot{u}_{1,3}^{(o)}) + \eta'_{46}\,(\dot{u}_{2,1}^{(o)} + \dot{u}_1^{(1)})]$$

$$t_{13}^{(o)} = 2b\,[c'_{51}u_{1,1}^{(o)} + c'_{53}u_{3,3} + c'_{54}\,(u_{2,3}^{(o)} + u_3^{(1)})$$

$$+ c'_{55}\,(u_{3,1}^{(o)} + u_{1,3}^{(o)}) + c'_{56}\,(u_{2,1}^{(o)} + u_1^{(1)})$$

$$+ \eta'_{51}\dot{u}_{1,1}^{(o)} + \eta'_{53}\dot{u}_{3,3}^{(o)} + \eta'_{54}\,(\dot{u}_{2,3}^{(o)} + \dot{u}_3^{(1)})$$

$$+ \eta'_{55}\,(\dot{u}_{3,1}^{(o)} + \dot{u}_{1,3}^{(o)}) + \eta'_{56}\,(\dot{u}_{2,1}^{(o)} + \dot{u}_1^{(1)})]$$

$$t_{12}^{(o)} = 2b\,[c'_{61}u_{1,1}^{(o)} + c'_{63}u_{3,3}^{(o)} + c'_{64}\,(u_{2,3}^{(o)} + u_3^{(1)})$$

$$+ c'_{65}\,(u_{3,1}^{(o)} + u_{1,3}^{(o)}) + c'_{66}\,(u_{2,1}^{(o)} + u_1^{(1)})$$

$$+ \eta'_{61}\dot{u}_{1,1}^{(o)} + \eta'_{63}\dot{u}_{3,3}^{(o)} + \eta'_{64}\,(\dot{u}_{2,3}^{(o)} + \dot{u}_3^{(1)})$$

$$+ \eta'_{65}\,(\dot{u}_{3,1}^{(o)} + \dot{u}_{1,3}^{(o)}) + \eta'_{66}\,(\dot{u}_{2,1}^{(o)} + \dot{u}_1^{(1)})]$$

where for p,q = 1, 2, 3

$$c'_{pq} = c_{pq} - \frac{c_{p2}c_{2q}}{c_{22}}$$

$$\eta'_{pq} = \eta_{pq} - \frac{c_{p2}\eta_{2q}}{c_{22}}$$

The first order equations are obtained by eliminating the three strains $S_{22}^{(1)}$, $S_{21}^{(1)}$, and $S_{23}^{(1)}$ from the constraints on the stresses. Upon this elimination the first order stress displacement equations are

$$t_{11}^{(1)} = \frac{2b^3}{3}\left[c_{11}'''u_1^{(1)} + c_{13}'''u_3^{(1)} + c_{15}'''\left(u_{3,1}^{(1)} + u_{1,3}^{(1)}\right)\right.$$

$$\left. + \eta_{11}''''\dot{u}_1^{(1)} + \eta_{13}''''\dot{u}_3^{(1)} + \eta_{15}'''\left(\dot{u}_{3,1}^{(1)} + \dot{u}_{1,3}^{(1)}\right)\right]$$

$$t_{33}^{(1)} = \frac{2b^3}{3}\left[c_{31}'''u_1^{(1)} + c_{33}'''u_3^{(1)} + c_{35}'''\left(u_{3,1}^{(1)} + u_{1,3}^{(1)}\right)\right.$$

$$\left. + \eta_{31}''''\dot{u}_1^{(1)} + \eta_{33}''''\dot{u}_3^{(1)} + \eta_{35}'''\left(\dot{u}_{3,1}^{(1)} + \dot{u}_{1,3}^{(1)}\right)\right]$$

$$t_{13}^{(1)} = \frac{2b^3}{3}\left[c_{51}'''u_1^{(1)} + c_{53}'''u_3^{(1)} + c_{55}'''\left(u_{3,1}^{(1)} + u_{1,3}^{(1)}\right)\right.$$

$$\left. + \eta_{51}''''\dot{u}_1^{(1)} + \eta_{53}''''\dot{u}_3^{(1)} + \eta_{55}'''\left(\dot{u}_{3,1}^{(1)} + \dot{u}_{1,3}^{(1)}\right)\right] \qquad \text{(3A-16)}$$

Where the consecutive eliminations of the strains yield the constants:

$$c_{pq}'' = c_{pq}' - \frac{c_{p4}'c_{4q}'}{c_{44}'}$$

$$c_{pq}''' = c_{pq}'' - \frac{c_{p6}''c_{6q}''}{c_{66}''}$$

and viscous constants

$$\eta_{pq}''' = \eta_{pq}' - \frac{c_{p4}'\eta_{4q}'}{c_{44}'}$$

$$\eta_{pq}''' = \eta_{pq}'' - \frac{c_{p6}''\eta_{6q}''}{c_{66}''} \qquad \text{(3A-17)}$$

The setting of $t_{22}^{(1)}$ to zero is sufficient for $u_2^{(2)}$ to be decoupled from the first order elastic equations, however, it is observed that the vanishing of the viscous terms coupled to $\dot{u}_2^{(2)}$ is accomplished by setting it to zero. The zeroth order stresses, $t_{23}^{(o)}$ and $t_{21}^{(o)}$, are coupled into the first order equations of motion. These stresses may then be determined in terms of the first order stresses and inertia terms $u_3^{(1)}$ and $u_1^{(1)}$. Another coupling of zeroth and first order displacements arises from the condition that the waves of propagation be straight-crested along the thickness. This imposes the restriction that $S_4^{(o)}$ and $S_6^{(o)}$ are due to displacement components of a rotation and vanish through constraints of

$$s_{23}^{(o)} = 0$$

$$s_{21}^{(o)} = 0$$

Yield

$$u_1^{(1)} = -u_{2,3}^{(o)}$$

$$u_3^{(1)} = -u_{2,1}^{(o)} \qquad \text{(3A-18)}$$

When the above restrictions are substituted into the first order equations of motion, $t_{21}^{(o)}$ and $t_{23}^{(o)}$ become

$$t_{21}^{(o)} = -\frac{2b^3}{3}\left[c_{11}^{'''} u_{2,111}^{(o)} + 3c_{51}^{'''} u_{2,311}^{(o)} + 2c_{55}^{'''} u_{2,331}^{(o)}\right.$$

$$\left. + \left(\eta_{51}^{'''} + 2\eta_{15}^{''}\right) \dot{u}_{2,311}^{(o)} + \eta_{53}^{''''} \dot{u}_{2,333}^{(o)}\right.$$

$$+ 2\eta'''_{55}\dot{u}^{(o)}_{2,331} + \eta'''_{13}\dot{u}^{(o)}_{2,331} + \eta'''_{11}\dot{u}^{(o)}_{2,111}]$$

$$t^{(o)}_{23} = -\frac{2b^3}{3}[c'''_{51}u^{(o)}_{2,111} + 3c'''_{53}u^{(o)}_{2,133} + (c'''_{31} + 2c'''_{55})u^{(o)}_{2,113}$$

$$+ c'''_{33}u^{(o)}_{2,333} + \eta'''_{51}\dot{u}^{(o)}_{2,111} + (\eta'''_{31} + 2\eta'''_{55})\dot{u}^{(o)}_{2,113}$$

$$+ (\eta'''_{53} + 2\eta'''_{35})\dot{u}^{(o)}_{2,133}] \qquad (3A\text{-}19)$$

The rotary inertia terms $\rho\ddot{u}^{(1)}_1$ and $\rho\ddot{u}^{(1)}_3$ are assumed small at low frequencies and not included in the above expressions. These two equations can be introduced into the zeroth order stress-strain equations by solving consecutively for $S^{(o)}_{23}$ and $S^{(o)}_{21}$ from the zeroth order equations in terms of $t^{(o)}_{23}$ and $t^{(o)}_{24}$ and substituting into the remaining equations. The zeroth order stress displacement equations are now

$$t^{(o)}_{11} = 2b[c'''_{11}u^{(o)}_{1,1} + c'''_{13}u^{(o)}_{3,3} + c'''_{15}(u^{(o)}_{3,1} + u^{(o)}_{1,3})$$

$$+ \eta'''_{11}\dot{u}^{(o)}_{1,1} + \eta'''_{13}\dot{u}^{(o)}_{3,3} + \eta'''_{15}(\dot{u}^{(o)}_{3,1} + \dot{u}^{(o)}_{1,3})]$$

$$+ \frac{c'_{14}}{c_{44}}\,\frac{[1 - c''_{16}]}{c''_{66}}\,t^{(o)}_4 + \frac{c''_{16}}{c''_{66}}\,t^{(o)}_6$$

$$t^{(o)}_{33} = 2b[c'''_{31}u^{(o)}_{1,1} + c'''_{33}u^{(o)}_{3,3} + c'''_{35}(u^{(o)}_{3,1} + u^{(o)}_{1,3})$$

$$+ \eta_{31}^{''''\cdot} u_{1,1}^{(o)} + \eta_{33}^{''''\cdot} u_{3,3}^{(o)} + \eta_{35}^{'''} (\dot{u}_{3,1}^{(o)} + \dot{u}_{1,3}^{(o)})]$$

$$+ \frac{c_{34}^{'}}{c_{44}} \frac{[1 - c_{36}^{''}]}{c_{66}^{''}} t_4^{(o)} + \frac{c_{36}^{''}}{c_{66}^{''}} t_6^{(o)}$$

$$t_{31}^{(o)} = 2b\,[c_{51}^{'''} u_{1,1}^{(o)} + c_{53}^{'''} u_{3,3}^{(o)} + c_{55}^{'''} (u_{3,1}^{(o)} + u_{1,3}^{(o)})$$

$$+ \eta_{51}^{'''} u_{1,1}^{(o)} + \eta_{53}^{'''} u_{3,3}^{(o)} + \eta_{55}^{'''} (\dot{u}_{3,1}^{(o)} + \dot{u}_{1,3}^{(o)})]$$

$$+ \frac{c_{54}^{'}}{c_{44}} \frac{[1 - c_{56}^{''}]}{c_{66}^{''}} t_4^{(o)} + \frac{c_{56}^{''}}{c_{66}^{''}} t_6^{(o)} \qquad \text{(3A-20)}$$

The above three stresses are those remaining after the reduction to low frequency modes. The substitution of these stresses into the zeroth order equations of motion yields the development of the displacements due to general triclinic symmetry. The resulting displacement equations can be simplified by assuming an infinite dimensional plate in the x_3 direction. The displacement equations of motion for this case are

$$2b\rho u_j^{(o)} = t_{1j,1}^{(o)} \qquad \text{(3A-21)}$$

Which when written in terms of the displacements become

Which when written in terms of the displacements become

$$\rho\ddot{u}_1^{(o)} = c_{11}^{'''} u_{1,11}^{(o)} + c_{15}^{'''} u_{3,11}^{(o)} + \eta_{11}^{''''} \dot{u}_{1,11}^{(o)} + \eta_{15}^{''''} \dot{u}_{3,11}^{(o)}$$

$$- \frac{b^2}{3} \frac{c_{14}^{'}}{c_{44}^{'}} \left[1 - \frac{c_{16}^{''}}{c_{66}^{''}}\right] \left(c_{51}^{'''} u_{2,1111}^{(o)} + \eta_{51}^{''''} \dot{u}_{2,111}^{(o)}\right)$$

$$- \frac{b^2}{3} \frac{c_{11}^{''}}{c_{66}^{''}} \left(c_{11}^{'''} u_{2,1111}^{(o)} + \eta_{11}^{''''} \dot{u}_{2,1111}^{(o)}\right)$$

$$\rho\ddot{u}_3^{(o)} = c_{51}^{'''} u_{1,11}^{(o)} + c_{55}^{'''} u_{3,11}^{(o)} + \eta_{51}^{''''} \dot{u}_{1,11}^{(o)} + \eta_{55}^{''''} \dot{u}_{3,11}^{(o)}$$

$$- \frac{b^2}{3} \frac{c_{54}^{'}}{c_{44}^{'}} \left[1 - \frac{c_{56}^{''}}{c_{66}^{''}}\right] \left[c_{51}^{'''} u_{2,1111}^{(o)} + \eta_{51}^{''''} \dot{u}_{2,111}^{(o)}\right]$$

$$- \frac{b^2}{3} \frac{c_{56}^{''}}{c_{66}^{''}} \left[c_{11}^{'''} u_{2,1111}^{(o)} + \eta_{11}^{''''} \dot{u}_{2,1111}^{(o)}\right]$$

$$\rho\ddot{u}_2^{(o)} = - \frac{b^2}{3} \left[c_{11}^{'''} u_{2,1111}^{(o)} + \eta_{11}^{''''} \dot{u}_{2,1111}^{(o)}\right] \qquad (3A\text{-}22)$$

The first two equations are extensional and the third is a flexural equation. The viscoelastic constants couple the displacements for the extensional modes. The effect of the first order terms are observed as the coefficients of b^2. It is noted that the flexure mode is composed entirely of first order terms and that it is uncoupled from the extensional displacements.

3A.6 Biaxial Symmetry Dispersion Relation

A biaxially oriented film of PVF_2 is of symmetry 2 mm which has elastic constants of the form

$$[c_{ij}] = \begin{matrix} c_{11} & c_{12} & c_{13} & 0 & 0 & 0 \\ c_{21} & c_{22} & c_{23} & 0 & 0 & 0 \\ c_{31} & c_{32} & c_{33} & 0 & 0 & 0 \\ 0 & 0 & 0 & c_{44} & 0 & 0 \\ 0 & 0 & 0 & 0 & c_{55} & 0 \\ 0 & 0 & 0 & 0 & 0 & c_{66} \end{matrix} \qquad \text{(3A-23)}$$

The propagation equations reduce for this symmetry to

$$\rho u_1^{(o)} = c_{11}' \, u_{1,11}^{(o)} + \eta_{11}' \, \dot{u}_{1,11}^{(o)}$$

$$\rho u_3^{(o)} = c_{55} \, u_{3,11}^{(o)} + \eta_{55} \, \dot{u}_{3,11}^{(o)}$$

$$\rho u_2^{(o)} = -\frac{b^2}{3} \, (c_{11}' \, u_{2,1111}^{(o)} + \eta_{11}' \, \dot{u}_{2,1111}^{(o)})$$

(3A-24)

When the function for a decaying wave along the x_1 direction is substituted into the equation of motion $u_1^{(o)}$, the real and imaginary components of the wave vector are given as

$$k^2 = \rho\omega^2 \, [1 + (1 + \omega^2 \eta_{11}^2 / c_{11}'^2)^{\frac{1}{2}}]/2c_{11}' \, (1 + \omega^2 \eta_{11}^2 / c_{11}'^2)$$

$$\alpha^2 = \rho\omega^2 \, [1 + (1 + \omega^2 \eta_{11}^2 / c_{11}'^2)^{\frac{1}{2}}]/2c_{11}' \, (1 + \omega^2 \eta_{11}^2 / c_{11}'^2)$$

which reduces for small η_{11}'/c_{11}' to

$$\alpha^2 = \rho/4 \; \frac{\eta'^2_{11}}{c'^2_{11}} \; \omega^4 \qquad \text{(3A-25)}$$

The same dispersion relations occurs for the shear displacement $u_3^{(o)}$ and are found by substituting the constants C_{55} and η_{55} into the above equations.

The flexure mode yields a quartic equation in α and k when a decaying wave is substituted in the equation of motion for $u_2^{(o)}$. The solutions for the real and imaginary parts of the wave vector are

$$k^2 = \frac{\omega}{2}(3\rho/c'_{11}b^2)^{\frac{1}{2}} \left[1 + ((1 - 4\omega^2\eta'^2_{11}/c'^2_{11})^{\frac{1}{2}})/2\right]^{\frac{1}{2}}$$

$$\alpha^2 = \frac{\omega}{2}(3\rho/c'_{11}b^2)^{\frac{1}{2}} \left[1 - ((1 + (1 - 4\omega^2\eta'^2_{11}/c'^2_{11})^{\frac{1}{2}}/2)^{\frac{1}{2}}\right]$$

which for small η'_{11}/c'_{11} yields

$$\alpha^2 = \omega^3 (3\rho/c'_{11}b^2)^{\frac{1}{2}} \eta'^2_{11}/c'^2_{11}$$

(3A-26)

3A.7 Hysteretic Dispersion Relations

For a semicrystalline polymer, the crystallites act as cross-links and prevent the mechanical motion needed for a viscous loss. The attentuation has been evaluated to depend linearly upon the frequency which is indicative of a hysteretic loss. The constituitive equation for the hysteretic loss is of the form

$$T_p = c_{pq}s_q + jh_{pq}s_q \tag{3A-27}$$

where h_{pq} is the loss tensor component and j is $\sqrt{-1}$. It is noted that there is a direct similarity between the imaginary component and that of the time harmonic viscous loss. An analysis following the previous derivation leads to equations of motion of the same form as the viscous equation; however, the coupling of constants due to the free boundary conditions are both complex and are

$$c_{11}^{',*} = c_{11} - c_{12}^2/c_{22} + jh_{22}$$

$$h_{11}^{',*} = h_{11} - c_{13}h_{31}/c_{22} + jh_{22} \tag{3A-28}$$

The extensional equations of motion for $u_1^{(o)}$ becomes

$$[c_{11} - (c_{12}^2c_{22} + h_{21}h_{22}c_{12})/(c_{22}^2 + h_{22}^2)]\, u_{1,11}^{(o)}$$

$$+ j\,[h_{11} + (c_{12}^2h_{22} - c_{12}c_{22}h_{21})/(c_{22}^2 + h_{22}^2)\, u_{1,11}^{(o)}$$

$$= \rho\ddot{u}_{1,11}^{(o)} \tag{3A-29}$$

The dispersion relations are found to be

$$k^2 = \frac{\rho\omega^2}{a(1 + b^2/a^2)} \left[1 + (1 + b^2/a^2)^{\frac{1}{2}}\right]/2$$

and

$$\alpha^2 = \frac{\rho\omega^2}{a(1 + b^2/a^2)} \left[-1 + (1 + b^2/a^2)^{\frac{1}{2}}\right]/2 \qquad \text{(3A-30)}$$

where

$$a = \frac{c_{11} - c_{12}^2 c_{22} - h_{21}h_{22}c_{12}}{c_{22}^2 + h_{22}^2}$$

and

$$b = \frac{h_{11} + c_{12}^2 h_{22} - c_{12}c_{22}h_{21}}{c_{22}^2 + h_{22}^2} \qquad \text{(3A-31)}$$

which up to second order in h_{22}/c_{22} become

$$a = c_{11} - \frac{c_{12}^2}{c_{22}} - \frac{c_{12}h_{21}h_{22}}{c_{22}^2}$$

$$b = h_{11} + \frac{c_{12}^2 h_{22}}{c_{22}^2} - \frac{c_{12}h_{21}}{c_{22}} \qquad \text{(3A-32)}$$

Thus the dispersion relations for the hysteresis loss to second order terms in h_{11}/c_{11} are

$$k^2 = \frac{\rho\omega^2}{c_{11}} \left(1 - 3/8\ h_{11}'^2/c_{11}'^2\right)$$

$$\alpha^2 = \frac{\rho\omega^2}{2c_{11}} \left[\frac{1}{2} \frac{h_{11}'^2}{c_{11}^2}\right] \qquad \text{(3A-33)}$$

Similarly the dispersion relations for the remaining modes can be found by substituting into the viscoelastic relations for the elastic constant and for the viscous constant $\omega\eta_{11}$. For the viscous case, the k vector decreases due to second order terms in the viscosity. Since the frequency is constant, this yields an increase in the phase velocity. A similar expansion for the hysteresis loss indicates a similar trend although there is also a second order decrease in the elastic constant which tends to decrease the velocity. This decrease is a second order effect and does not appear in the viscoelastic treatment since the initial condition on the velocity of the thickness displacement $u_2^{(1)}$ was set to zero for the viscoelastic case.

3A.8 Summary

The displacement equations of motion of the three lowest frequency modes of propagation in anisotropic lossy plates have been derived by Mindlin's formulation. The boundary conditions of vanishing stresses across the plate couple the loss constants to the elastic constants in the equations for the remaining stress equations. The dispersion relations derived using these stresses yielded the attenuation dependence for the extensional waves to first and second powers of the frequency for the respective hysteretic and viscous losses. However, the flexural attenuation for a viscous loss was to the three-halves power of the frequency.

The coupling of the equations are symmetry dependent and, for a biaxial film of 2 mm symmetry such as PVF_2, the extensional

shear wave viscoelastic constants are uncoupled and can be evaluated directly from experiment. The elastic and hysteretic plate mode constants along each principle axis were evaluated including the values of the uncoupled shear constants.

APPENDIX 4A

Creation of a Thin Lens By Index of Refraction Variation

Consider the geometry shown in Figure 4A-1 where a material of width Δ and variable index of refraction, $n(x,y)$, is centered on the z-axis and lies in the x-y plane. A wave at coordinates (x,y) will suffer a phase delay in passing through the material given by

$$\phi(x,y) = k\Delta n(x,y) \tag{4A-1}$$

Where

$k = \frac{2\pi}{\lambda}$ = Wave Number

λ = Wavelength ,

In attempting to vary the index of refraction to match the spherical curvature of a thin lens, assume

$$n(x,y) = n_o \left(1 - \frac{R_1 - \sqrt{R_1^2 - x^2 - y^2}}{\Delta}\right) + \frac{R_1 - \sqrt{R_1^2 - x^2 - y^2}}{\Delta} \tag{4A-2}$$

Where Figure 4A-2applies for definitions. The phase delay then becomes

$$\phi(x,y) = k\Delta\, n_o \left(1 - \frac{R_1 - \sqrt{R_1^2 - x^2 - y^2}}{\Delta}\right) + \frac{R_1 - \sqrt{R_1^2 - x^2 - y^2}}{\Delta} \tag{4A-3}$$

Equivalently,

$$\phi(x,y) = k\Delta n_o - k(n_o-1)R_1 \left[1 - \sqrt{1 - \frac{x^2 + y^2}{R_1^2}}\right] \tag{4A-4}$$

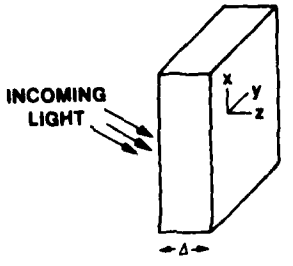

Figure 4A-1 Basic Configuration

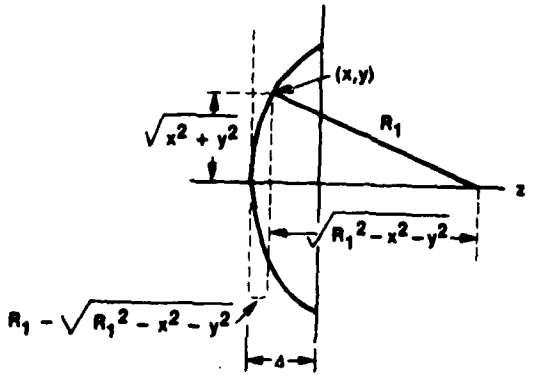

Figure 4A-2 Geometry of Variation

Using the Paraxial Approximation

$$\sqrt{1 - \frac{x^2 + y^2}{R_1^2}} \cong 1 - \frac{x^2 + y^2}{2R_1^2} \tag{4A-5}$$

Equation (4A-4) becomes

$$\phi(x,y) = k\Delta n_o - k(n_o - 1)R_1 \left[1 - \left(1 - \frac{x^2 + y^2}{2R_1^2}\right)\right] \tag{4A-6}$$

or finally,

$$\phi(x,y) = k\Delta n_o - k(n_o - 1)\frac{x^2 + y^2}{2R_1} \tag{4A-7}$$

The Corresponding Transmission Function is

$$t(x,y) = \exp j\phi(x,y) = \exp\left[jk\Delta n_o\right] \exp\left[-jk(n_o-1)\frac{x^2 + y^2}{2R_1}\right] \tag{4A-8}$$

But using the definition of focal length for a plano-convex lens

$$\frac{1}{f} \triangleq \frac{n_o - 1}{R_1} \tag{4A-9}$$

Equation (4A-8) becomes

$$t(x,y) = \exp\left[jk\Delta n_o\right] \exp\left[\frac{-jk}{2f}(x^2 + y^2)\right] \tag{4A-10}$$

Equation(4A-10) is the transmission function of a thin lens Note that n(x,y) could have been considered to increase rapidly and if appropriately chosen would have resulted in a plano-concave equivalent lens.

The form of the index of refraction given in equation (4A-2) can be simplified. Letting $r = x^2 + y^2$, it becomes

$$n(r) = n_o - \frac{(n_o - 1)}{\Delta}\left[R_1 - \sqrt{R_1^2 - r^2}\right] \tag{4A-11}$$

Equivalently,

$$n(r) = n_o - \frac{(n_o - 1)}{\Delta} R_1 \left[1 - \sqrt{1 - \frac{r^2}{R_1^2}} \right] \qquad (4A\text{-}12)$$

Again using the paraxial approximation

$$n(r) = n_o - \frac{(n_o - 1)R_1}{\Delta} \left[1 - 1 + \frac{r^2}{2R_1^2} \right]$$

$$n(r) = n_o - \frac{(n_o - 1)r^2}{2\Delta R_1} \qquad (4A\text{-}13)$$

Finally, using the definition of focal length given in Equation (4A-9) the required variation of the index of refraction becomes

$$n(r) = n_o - \frac{r^2}{2\Delta f} \qquad (4A\text{-}14)$$

APPENDIX 4B

Birefringence

Crystals generally are electrically and thus optically anisotropic. An electric field produces a polarization in a crystal which is not always a scalar times the field. Instead the magnitude and direction of the polarization depend on the direction of the applied field in relation to the crystal lattice. As will be shown, one important consequence of this phenomenon is that the velocity of light propagation within the crystal is a function of the direction of propagation and the polarization of the light.

A monochormatic ray of light propagating through an anisotropic crystal is split into two rays. These orthogonally polarized rays generally travel at different speeds and in different directions. This phenomenon is known as birefringence or double refraction. Natural double refraction is exhibited by 20 of the 32 solid crystal classes and all liquid crystals.

In an anisotropic material, the relation between the displacement, $\overline{D}$, and the electric field intensity, $\overline{E}$, can be written

$$D_i = \sum_j \epsilon_o \epsilon_{ij} E_j \qquad i = 1,2,3 \qquad (4B\text{-}1)$$

where ϵ_o = Free space permittivity

ϵ_{ij} = Components of the dielectric constant tensor

Equivalently,

$$D_i \epsilon_o^{-1} = E_{ij} E_j \qquad (4B\text{-}2)$$

Where Einstein notation - summation is to be performed over that index which appears more than once on any term (in this case $j = 1,3,2$)- is used. Equation 4B-2 written out in matrix form is

$$\frac{1}{\varepsilon_o}\begin{bmatrix} D_1 \\ D_2 \\ D_3 \end{bmatrix} = \begin{bmatrix} \varepsilon_{11} & \varepsilon_{12} & \varepsilon_{13} \\ \varepsilon_{21} & \varepsilon_{22} & \varepsilon_{23} \\ \varepsilon_{31} & \varepsilon_{32} & \varepsilon_{33} \end{bmatrix}\begin{bmatrix} E_1 \\ E_2 \\ E_3 \end{bmatrix} \qquad (4B\text{-}3)$$

The single quantity ε in the isotropic case is replaced by an array of nine components which relate the three components of $\overline{D}$ to the three components of $\overline{E}$. $\overline{D}$ is no longer necessarily in the same direction as $\overline{E}$.

The Maxwell equations are still

$$\overline{\nabla} \times \overline{E} = \frac{-\partial \overline{B}}{\partial t} \qquad (4B\text{-}4)$$

and

$$\nabla \times \overline{H} = \overline{J} + \frac{\partial \overline{D}}{\partial t} \qquad (4B\text{-}5)$$

Transparent crystals have low conductivities and are not ferromagnetic. Thus

$$\overline{J} = 0 \qquad (4B\text{-}6)$$

and

$$\overline{B} = \mu_o \overline{H} \qquad (4B\text{-}7)$$

Using these equations (4B-4) and (4B-5) become

$$\nabla \times \overline{E} = -\mu_o \frac{\partial \overline{H}}{\partial t} \qquad (4B\text{-}8)$$

and

$$\nabla \times \overline{H} = \frac{\partial \overline{D}}{\partial t} \qquad (4B\text{-}9)$$

However, now in the propagation equation obtained by eliminating $\bar{H}$ from these two equations

$$\mu_o \frac{\partial^2 \bar{D}}{\partial t^2} = \nabla^2 \bar{E} - \nabla(\bar{\nabla}.\bar{E}) \qquad (4B\text{-}10)$$

The term containing $\nabla.\bar{E}$ does not vanish as it would in the isotropic case.

For the case of plane waves

$$\bar{E} = \bar{E}_o \, e^{j\omega(t - \frac{\bar{r}.\bar{\ell}}{v})} \qquad (4B\text{-}11)$$

where

$\bar{E}_o$ = Constant vector

ω = Wave frequency

v = Wave propagation velocity

$\bar{\ell}$ = Unit vector in direction of wave propagation (wave normal)

$\bar{r}$ = Position vector

Equation (4B-10) becomes

$$\mu_o v^2 \bar{D} - \bar{E} = \bar{\ell}(\bar{\ell}.\bar{E}) = 0 \qquad (4B\text{-}12)$$

If ϵ_1, ϵ_2, and ϵ_3 are the diagonal terms in the dielectric constant tensor referred to the principal axes, and ℓ_1, ℓ_2, and ℓ_3 are the three components of $\bar{\ell}$ along the principal axes, then (4B-12) simplifies to

$$\frac{\ell_1^2}{\mu_o v^2 - \frac{1}{\epsilon_o \epsilon_1}} \quad \frac{\ell_2^2}{\mu_o v^2 - \frac{1}{\epsilon_o \epsilon_2}} + \mu_o v^2 - \frac{\ell_3^2}{\frac{1}{\epsilon_o \epsilon_3}} = 0 \qquad (4B\text{-}13)$$

This is a quadratic equation in v^2. If the negative values of v are discarded, there are in general two values of v associated with each wave normal $\bar{\ell}$. The $\bar{E}$ and $\bar{D}$ fields associated with each value of v are found to be linearly polarized. Further, $\bar{D}$ vectors with different velocities are orthogonal to each other.

The relative vector configuration is shown in Figure 4B-1. In an isotropic material or free space, $\bar{D}$ is collinear with $\bar{E}$ and the Poynting vector, $\bar{S} = \bar{E} \times \bar{H}$, is collinear with $\bar{\ell}$. In an anisotropic material $\bar{D}$ is related to E through a tensor relationship and is, therefore, not necessarily parallel to $\bar{E}$. It follows that $\bar{S}$ is not necessarily parallel to $\bar{\ell}$. This means that the direction of energy propagation is not the direction of phase advance.

The value of c/v for each of the two possible waves is defined as the refraction index, n for that wave. The refractive indices of the two waves, as functions of the direction of their common wave normal, can be obtained by drawing the indicatrix, the ellipsoid shown in Figure 4B-2.

If x_1, x_2, and x_3 are the principal axes of the permittivity tensor, the indicatrix is defined by the equation.

$$\frac{x_1^2}{n_1^2} + \frac{x_2^2}{n_2^2} + \frac{x_3^2}{n_3^2} = 1 \qquad (4B\text{-}14)$$

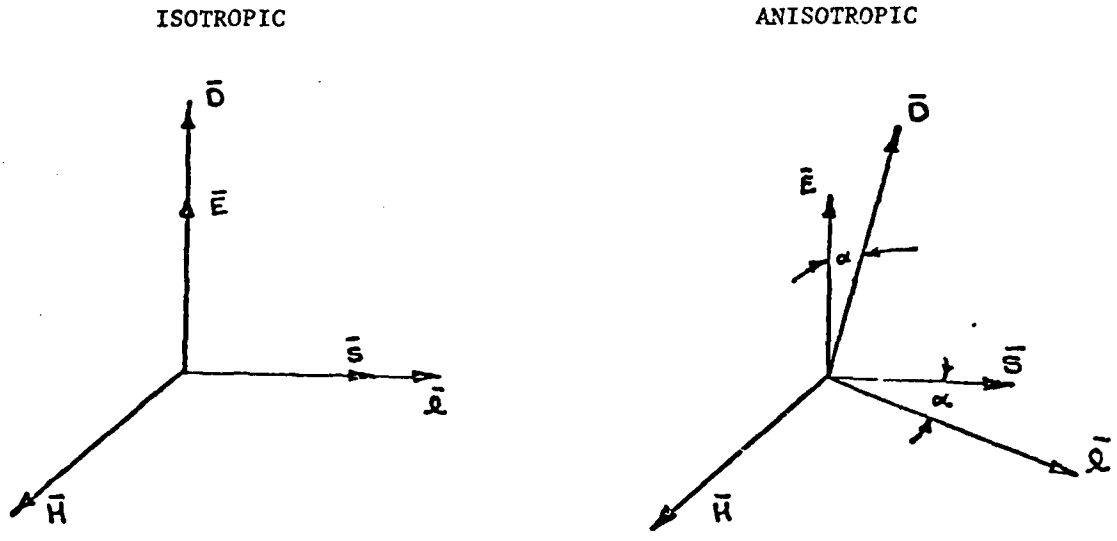

Figure 4B-1
VECTOR COMPARISON OF
ISOTROPIC AND ANISOTROPIC
MATERIALS

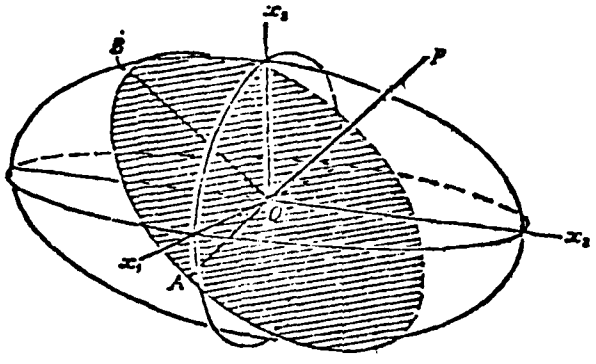

Figure 4B-2
THE INDICATRIX

where n_1, n_2, and n_3 are the principal refractive indices. The indicatrix has the following important property. Draw through the origin a straight line OP in an arbitrary direction. Draw the central section of the indicatrix perpendicular to it. This will be an ellipse. Then the two wavefronts normal to OP that may be propagated through the crystal have refractive indices equal to the semi-axes, OA and OB, of this ellipse. The displacement vector $\bar{D}$ in the plane polarized wave with refractive index equal to OA vibrates parallel to OA. Similarly, the displacement vector in the wave with refractive index equal to OB vibrates parallel to OB. From this it follows that the two possible waves with wave normal x_1 have refractive indices n_2 and n_3 and $\bar{D}$ is parallel to x_2 and x_3 respectively. Similarly, the wave normal x_2 corresponds to two waves of refractive indices n_3 and n_1, with $\bar{D}$ parallel to x_3 and x_1. A similar statement applies to x_3. For this reason, n_1, n_2, and n_3 are called the principal refractive indices.

Note that the refractive index itself is not a tensor, although its variation with direction is determined by the dielectric constant which is a tensor.

Using the indicatrix, crystals can be classified into three categories according to the relationship among the three principal indices of refraction.

1. $n_1 = n_2 = n_3$

   The ellipsoid becomes a sphere. For any wave-normal direction, the central section is a circle. Thus, there is no natural birefringence for any wave normal direction. This is the case in cubic crystals and isotropic materials.

2. $n_1 = n_2 \neq n_3$

Here only one section is circular. So, for only wave-normal direction is there no birefringence. The axis is the direction of the unique index of refraction is called the optic or principal axis. This type of crystal is known as uniaxial. Hexagonal, trigonal, and tetragonal crystals belong to this group as do nematic liquid crystals.

3. $n_1 \neq n_2 \neq n_3$

Now, there are two different optic axes. The crystal is called biaxial. The three remaining crystal systems; orthorhombic, monoclinic, and triclinic belong to this class.

APPENDIX 4C

Nematic Director Orientation To Match Index of Refraction Variation

Liquid crystals are characterized by an orientational order of their constituent rod-like molecules [11]. In nematic liquid cyrstals this orientational order has uniaxial symmetry, the axis of uniaxial symmetry being parallel to a unit vector, $\hat{n}$, called the director. The indicatrix formulation given in Appendix 4B applies but since the orientation of the liquid crystal molecules can be altered under application of an external field the orientation of the indicatrix can be changed. This is analogous to reorienting a solid so that light passing through it "sees" a different index of refraction. Figure 4.2-2 illustrates this phenomenon. In this example, a liquid crystal possessing positive dielectric anisotropy is shown at the top of the figure in the homogeneous state. Correspondingly, the indicatrix is aligned so that a wave polarized in the x-direction is influenced by an index of refraction n_e. At the bottom of the figure, the orientation has been altered to the homeotropic state. In which case, the same polarized light encounters an index of refraction n_o. At an intermediate point, the index of refraction is dependent on θ.

4C.1 The Value of the Director

In Appendix 4A, the required index of refraction modulation to match an ideal thin lens was derived. To create that modulation, it is necessary to alter the orientation of the liquid

crystal molecules.

Consider the slice of the indicatrix shown in Figure 4C- 1 If light was propagating in the negative y_n direction and polarized in the x_n direction, it would "see" an index of refraction n_e. If the indicatrix was rotated through an angle θ_n. That same ray would "see" an index of refraction, r_n.

The slice of the indicatrix shown can be expressed as

$$\frac{x_n^2}{n_e^2} + \frac{y_n^2}{n_o^2} = 1 \qquad (4C\text{-}1)$$

But

$$r_n^2 = x_n^2 + y_n^2 \qquad (4C\text{-}2)$$

So equation(4C-1) can be written

$$\frac{r_n^2 - y_n^2}{n_e^2} + \frac{y_n^2}{n_o^2} = 1 \qquad (4C\text{-}3)$$

Equivalently,

$$y_n^2 = \frac{1 - r_n^2/n_e^2}{\left[\frac{1}{n_o^2} - \frac{1}{n_e^2}\right]} \qquad (4C\text{-}4)$$

$$y_n = \sqrt{\frac{1 - r_n^2/n_e^2}{\left[\frac{1}{n_o^2} - \frac{1}{n_e^2}\right]}} \qquad (4C\text{-}5)$$

From the geometry of Figure 4C-1

$$\sin\theta = \frac{y_n}{r_n} = \frac{1}{r_n}\sqrt{\frac{1 - r_n^2/n_e^2}{\left[\frac{1}{n_o^2} - \frac{1}{n_e^2}\right]}} \qquad (4C\text{-}6)$$

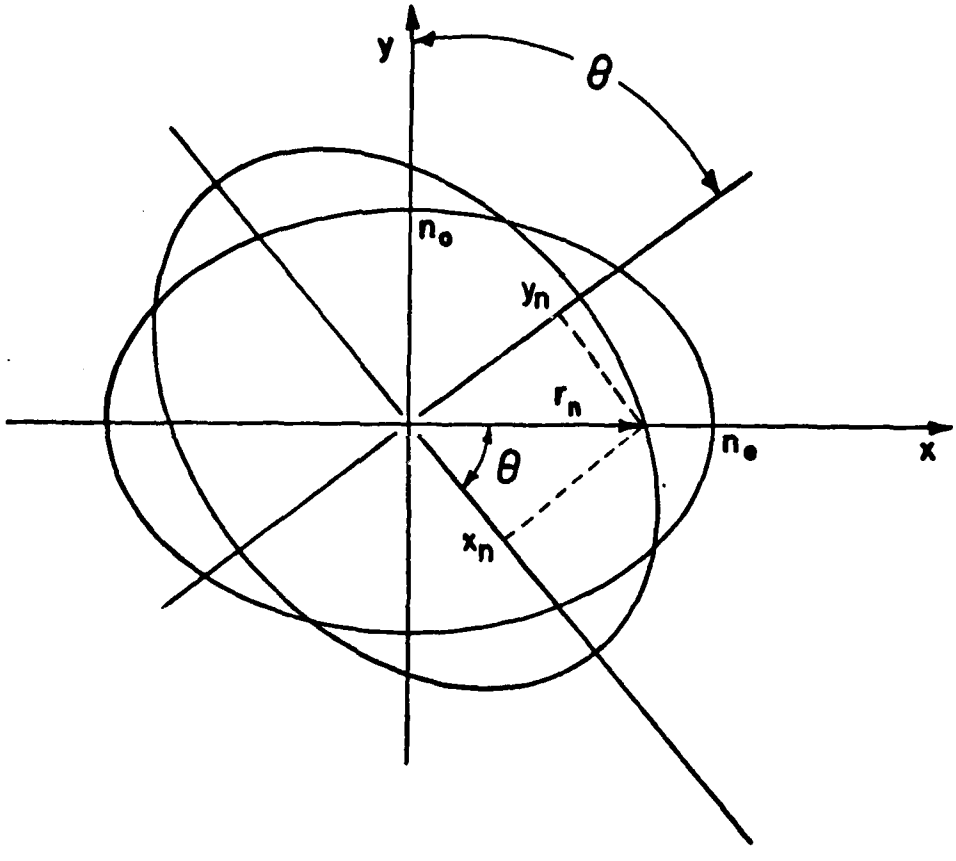

Figure 4C-2 The Indicatrix for a Uniaxial Crystal

Or finally,

$$\theta = \sin^{-1}\left[\sqrt{\frac{\frac{1}{r_n^2} - \frac{1}{n_e^2}}{\frac{1}{n_o^2} - \frac{1}{n_e^2}}}\right] \qquad (4C\text{-}7)$$

For any desired index of refraction between n_o and n_e, Equation 4C-7 gives the required θ or orientation of the nematic crystal director. Note that indeed when $r_n = n_e$, $\theta = 0^o$ and when $r_n = n_o$, $\theta = 90^o$.

Now the results of Appendix 4A can be factored into the required orientation. From Appendix 4A,

$$r_n = n_e - \frac{r^2}{2\Delta f} \qquad (4C\text{-}8)$$

Where terms have been altered to match their meaning here.

The required form for the index of refraction can now be substituted into equation (4C-7) yielding the required angle variation for the liquid crystal director as a function of the radial distance from the center of the liquid crystal lens.

As an example, let,

$n_e = 1.634$

$n_o = 1.492$

$\Delta = 14 \times 10^{-6}$ meters

$f = 10$ meters

Figure 4C-2, shows the required director variation.

Now that the required orientation of the director has been found, the next step is to identify what field is required to produce this variation.

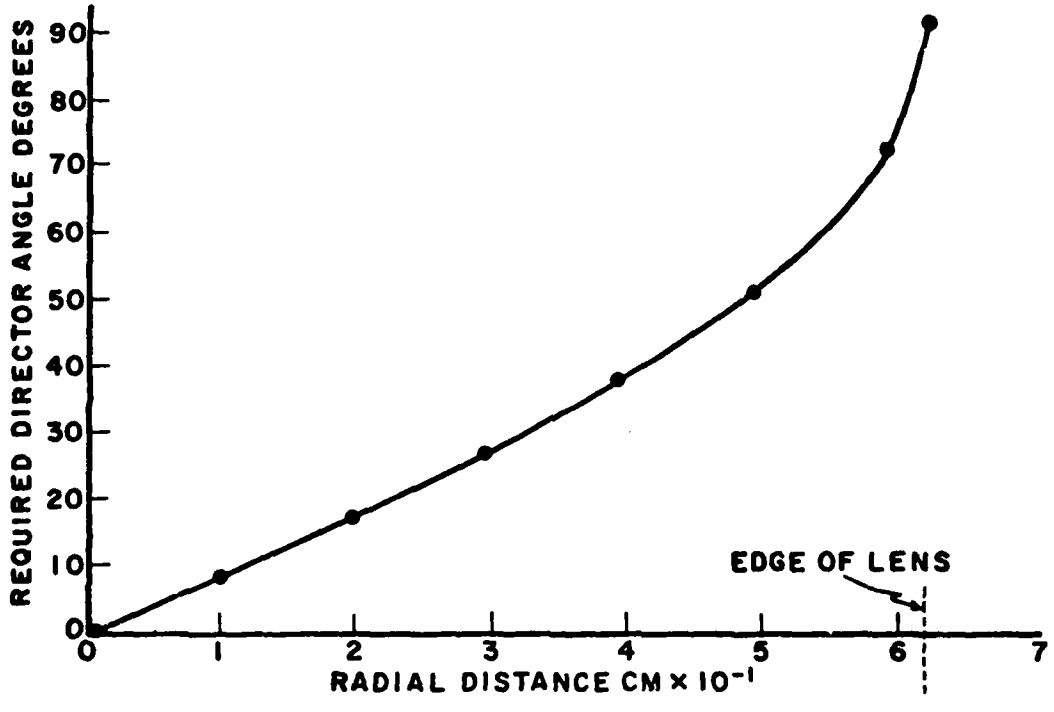

Figure 4C-2 Radial Distance cm x 10^{-1}

APPENDIX 4D

Orientation of the Liquid Crystal Director to an Applied Electric Field

For most display applications, liquid crystals are used as two state devices. That is, the crystal is either in its equilibrium state or is driven by application of a field to a highly altered state. To accomplish this result, devices are normally operated at two to five times the threshold voltages. Thus insuring the desired effect.

In attempting to create a lens with a liquid crystal, the transition state or partial reaction of the crystal to an applied field is critical. This appendix described the orientation of local directors to an applied field.

The intial formulation follows Sheng (Chapter 8, Ref.11). Consider a very small spatial region inside a macroscopic sample of nematic liquid crystal that contains a sufficiently large numbers of molecules of the same orientation so that a local director can be used to describe this orientation. Imagine the division of a macroscopic sample into such small spatial regions. In each region, define an orientational director, $\hat{n}$, so that a director field $\hat{n}(\vec{r})$ results.

Now the total free-energy density of the system under external fields can be written

$$F = F_d + F_m + F_e \qquad (4D\text{-}1)$$

Where

F_d = Free-energy density associated with distortion from equilibrium

F_m = Magnetic field contribution

F_e = Electric field contribution

The total free energy of the smaple is given by

$$\underline{F} = \int F \, d^3r \qquad (4D\text{-}2)$$

volume of

the sample

Sheng expands equations (4D-1) giving

$$F = \frac{1}{2}\{ K_{11}[\nabla\cdot\hat{n}(\vec{r})]^2 + K_{22}[|\hat{n}(\vec{r}) \cdot \nabla\times\hat{n}(\vec{r})| - \frac{\pi}{\lambda_o}]^2$$

$$+ K_{33}[|\hat{n}(\vec{r}) \times \nabla\times\hat{n}(\vec{r})|]^2 - \Delta\chi\,[\vec{H}\cdot\hat{n}(\vec{r})]^2 - \frac{1}{4\pi}\Delta\varepsilon[\vec{E}\cdot\hat{n}(\vec{r})]^2\} \qquad (4D\text{-}3)$$

Where

K_{11} = Spray elastic constant

K_{22} = Twist elastic constant

K_{33} = Bend elastic constant

$\Delta\chi \equiv \chi_{11} - \chi_{\perp}$

χ_{11} = Susceptibility per unit volume parallel to $\hat{n}(\vec{r})$

$\chi_{\perp}$ = Susceptibility per unit volume perpendicular to $\hat{n}(\vec{r})$

$\Delta\varepsilon = [\varepsilon_{11} - \varepsilon_{\perp}]\varepsilon_o$

ε_{11} = Dielectric constant parallel to $\hat{n}(\vec{r})$

$\varepsilon_{\perp}$ = Dielectric constant perpendicular to $\hat{n}(\vec{r})$

ε_o = Permittivity of free space

$\vec{H}$ = Externally applied magnetic field

$\vec{E}$ = Externally applied electric field

Figure 4D-1 gives an illustration to the meaning of the first three terms on the right hand side of Equations (4D-3).

By knowing that the liquid crystal molecules will orient to minimize the free energy (Equation 4D-2), it is now possible to use Equation (4D-3) and find the orientation of the liquid crystal director as a function of applied field strength and position within the sample.

Significant mathematical simplification results if the three constants, K_{11}, K_{22}, and K_{33}, collectively called the Frank constants are set equal to K. Similarly if the π/λ_o term is omitted which does not add to the minimization problem, Equation (4D-3) can be simplified to

$$F = \frac{K}{2} \{[\nabla . \hat{n}(\vec{r})]^2 + [|\nabla \times \hat{n}(\vec{r})|]^2 - \frac{\Delta\chi}{K}[\vec{H} . \hat{n}(\vec{r})]^2 - \frac{1}{4\pi}\frac{\Delta\varepsilon}{K}[\vec{E} . \hat{n}(\vec{r})]\} \quad (4D\text{-}4)$$

Consider the geometry in Figure (4D-2). A positive dielectric liquid crystal fills a space of width d centered at x = 0. Molecules are constrained at the surface to be parallel to the enclosure walls. With the application of an external electric field in the $\hat{x}$ direction, molecules away from the walls re-orient and attempt to line up with the field. From Figure (4D-2) the components of the local director, $\hat{n}(\vec{r})$, can be written as,

$$n_x = \cos\theta(x)$$

$$n_y = 0$$

$$n_z = \sin\theta(x) \quad (4D\text{-}5)$$

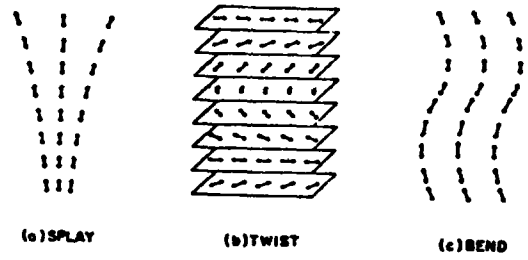

Figure 4D-1 Three types of distortion in a director field: (a) gives $\nabla.\hat{n}(\vec{r}) \neq 0$, (b) gives $\hat{n}(\vec{r}).\nabla x\hat{n}(\vec{r}) \neq 0$, and (c) gives $\hat{n}(\vec{r}) \times \nabla x\hat{n}(\vec{r}) \neq 0$. Each director is shown with double arrows in order to indicate that the "head" and the "tail" directions represent exactly the same physical state in a nematic sample.

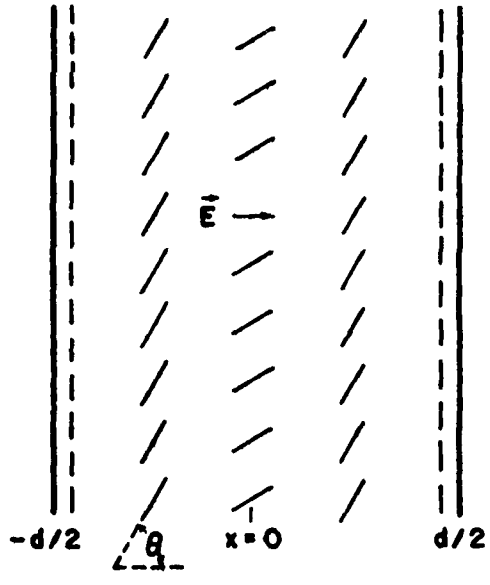

Figure 4D-2 Molecule Orientation With Applied Field

From which

$$[\nabla.\hat{n}(\vec{r})]^2 = \sin^2\theta \left[\frac{d\theta(x)}{dx}\right]^2 \tag{4D-6}$$

$$[|\nabla x\hat{n}(\vec{r})|]^2 = \cos^2\theta \left[\frac{d\theta(x)}{dx}\right]^2 \tag{4D-7}$$

And

$$-\frac{1}{4\pi}\Delta\epsilon[\vec{E}.\hat{n}(\vec{r})]^2 = -\frac{E^2\Delta\epsilon}{4\pi}\cos^2\theta \tag{4D-8}$$

And

$$\frac{-\Delta\chi}{K}[\vec{H}.\hat{n}(\vec{r})]^2 = 0 \tag{4D-9}$$

Substitution of these into equation (4D-4) gives the free energy density of the system as

$$F = \frac{K}{2}\{\left[\frac{d\theta}{dx}\right]^2 - \frac{E^2\Delta\epsilon}{4\pi K}\cos^2\theta\} \tag{4D-10}$$

Correspondingly, the total free energy is given by

$$F = \int \frac{K}{2}\{\left[\frac{d\theta}{dx}\right]^2 - \frac{E^2\Delta\epsilon}{4\pi K}\cos^2\theta\}dr^3 \tag{4D-11}$$

It is this function that the molecules move to minimize. To minimize an integral of the form

$$I = \int_a^b G(y(x), \frac{dy(x)}{dx}, x)dx \tag{4D-12}$$

By varying y(x), the optimal function y(x) must satisfy the equation

$$\frac{\partial G}{\partial y} - \frac{d}{dx}\left[\frac{\partial G}{\partial(\frac{dy}{dx})}\right] = 0 \tag{4D-13}$$

Which is called the Euler-Lagrange Equation. Comparing Equations (4D-11) and (4D-12) and noting that the only variations in the volume is in the x-direction gives

$$G = \left[\frac{d\theta}{dx}\right]^2 - \frac{E^2\Delta\varepsilon}{4\pi K}\cos^2\theta \qquad (4D\text{-}14)$$

And

$$y = \theta$$

Therefore, the Euler-Lagrange Equation becomes

$$\frac{2E^2\Delta\varepsilon}{4\pi K}\cos\theta\sin\theta - \frac{d}{dx}\left[2\,\frac{d\theta}{dx}\right] = 0 \qquad (4D\text{-}15)$$

Equivalently,

$$\frac{E^2\Delta\varepsilon}{4\pi K}\cos\theta\sin\theta - \frac{d^2\theta}{dx^2} = 0 \qquad (4D\text{-}16)$$

For simplicity, let

$$\xi_E = \frac{1}{E}\sqrt{\frac{4\pi K}{\Delta\varepsilon}} \qquad (4D\text{-}17)$$

So

$$\frac{1}{\xi_E^2}\cos\theta\sin\theta = \frac{d^2\theta}{dx^2} \qquad (4D\text{-}18)$$

Rewriting

$$\frac{\sin\theta\cos\theta}{\xi_E^2}\ \frac{d\theta}{dx} = \frac{d^2\theta}{dx}\cdot\frac{d\theta}{dx} = \frac{1}{2}\frac{d}{dx}\left(\frac{d\theta}{dx}\right)^2 \tag{4D-19}$$

$$\frac{\sin\theta}{\xi_E^2}\ \frac{d\sin\theta}{dx} = \frac{1}{2}\frac{d}{dx}\left(\frac{d\theta}{dx}\right)^2 \tag{4D-20}$$

Or

$$\frac{1}{2}\frac{1}{\xi_E^2}\frac{d\sin^2\theta}{dx} = \frac{1}{2}\frac{d}{dx}\left(\frac{d\theta}{dx}\right)^2 \tag{4D-21}$$

Integration Yields

$$\left(\frac{d\theta}{dx}\right)^2 = \left(\frac{\sin\theta}{\xi_E}\right)^2 + C \tag{4D-22}$$

The constant of integration can be evaluated by noting that because of symmetry $\left.\frac{d\theta}{dx}\right|_{x=0} = 0$. Calling the corresponding $\theta(x=0)=\theta_m$, the minimum value of θ

$$C = -\left(\frac{\sin\theta_m}{\xi_E}\right)^2 \tag{4D-23}$$

So equation (4D-22) becomes

$$\left(\frac{d\theta}{dx}\right)^2 = \left(\frac{\sin\theta}{\xi_E}\right)^2 - \left(\frac{\sin\theta_m}{\xi_E}\right)^2 \tag{4D-24}$$

Equivalently,

$$\frac{d\theta}{dx} = \pm\frac{1}{\xi_E}\sqrt{\sin^2\theta - \sin^2\theta_m} \tag{4D-25}$$

Where the negative sign applies for $-d/2 \leq x \leq 0$ and the positive sign applies for $0 \leq x \leq d/2$. Because of symmetry only one section needs to be considered. So, for $-d/2 \leq x \leq 0$,

$$\frac{1}{\xi_E} \int_{d/2}^{x} dx = - \int_{\pi/2}^{\theta} \frac{d\theta'}{\sin^2\theta' - \sin^2\theta_m} \qquad (4D\text{-}26)$$

Equivalently,

$$\frac{1}{\xi_E} \left[x + \frac{d}{2}\right] = - \int_{\pi/2}^{\theta} \frac{d\theta'}{\sin^2\theta' - \sin^2\theta_m} \qquad (4D\text{-}27)$$

Unfortunately, there is no closed form solution to the right side. Insight can be gained, however, by assuming that sufficient field strength has been applied to drive θ_m to zero. In that case, Equation (4D-27) becomes

$$\frac{1}{\xi_E} \left[x + \frac{d}{2}\right] = - \int_{\pi/2}^{\theta} \frac{d\theta'}{\sin^2\theta'} = - \int_{\pi/2}^{\theta} \frac{d\theta'}{\sin\theta'} \qquad (4D\text{-}28)$$

Or

$$\frac{-1}{\xi_E} \left[x + \frac{d}{2}\right] = \log \tan \frac{\theta}{2} \qquad (4D\text{-}29)$$

Finally

$$\theta = 2 \operatorname{Tan}^{-1} \exp \left[\frac{-1}{\xi_E} (x + \frac{d}{2})\right]$$

$$-d/2 < x < 0 \qquad (4D\text{-}30)$$

As an example let

$$d = 14 \times 10^{-6} \text{ meters}$$

$$K = 10^{-6} \text{ dynes} = 10^{-11} \text{ newtons}$$

$$\Delta\varepsilon = .7 \times \varepsilon_o = 6.195 \times 10^{-12} \frac{\text{farads}}{\text{m}}$$

Figure4D-3 shows the results for two different voltages across the cell. One very interesting fact comes out of this example. The average orientation of the directors are

$$\bar{\theta}_{50} = 22.5^o$$

And

$$\bar{\theta}_{100} = 14.9^o$$

If $n_e = 1.64$ and $n_o = 1.492$, then the average indices of refraction are

$$\bar{n}_{50} = 1.61$$

and

$$\bar{n}_{100} = 1.62$$

This is a small change in index of refraction for a significant change in orientation and a very significant change in applied voltage.

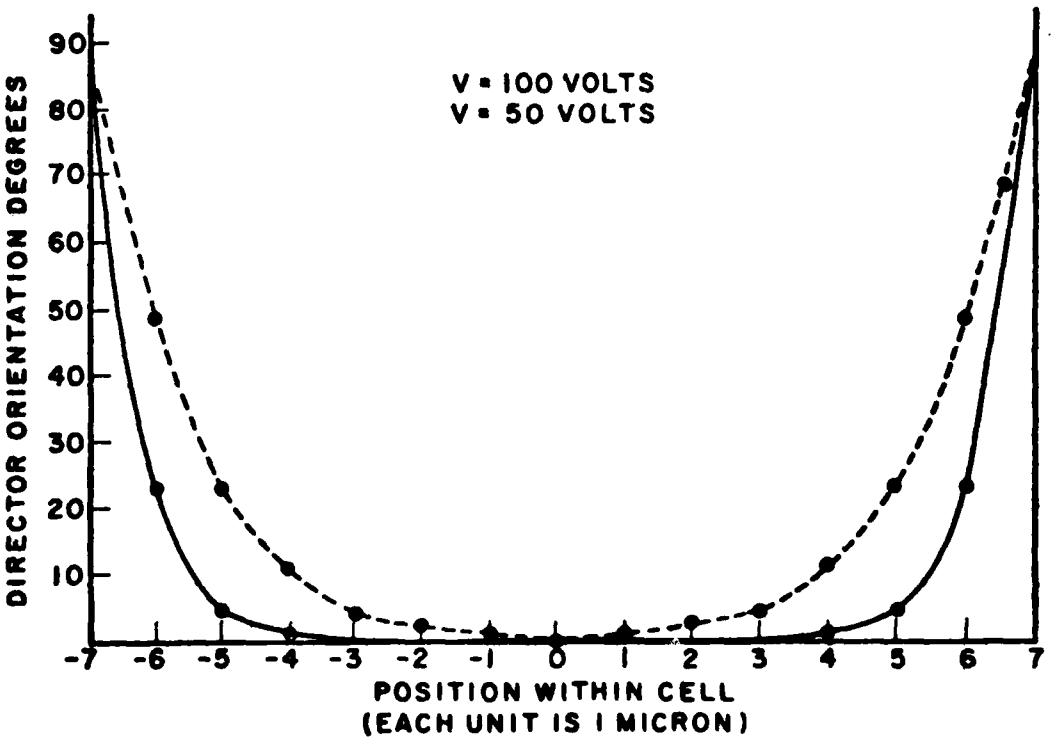

Figure 4D-3 Director Orientation Across Liquid Crystal

END

DATE
FILMED
11-81

DTIC